NTNU
Norwegian University of
Science and Technology

Using SURF imaging for efficient detection of micro-calcifications

Bastien Emmanuel Denarie

Master of Science in Engineering Cybernetics
Submission date: June 2010
Supervisor: Bjørn Atle J. Angelsen, ITK

Norwegian University of Science and Technology
Department of Engineering Cybernetics

Problem Description

Clustered micro-calcifications is an important indicator of early stage breast cancers, and an efficient real-time ultrasound imaging support is needed for conducting needle biopsies.
SURF is a dual-frequency band ultrasound imaging technique capable of imaging nonlinear scattering using the superposition of a low-frequency pulse to manipulate the tissue characteristics and an imaging pulse to extract the information. This new technique has already demonstrated its superiority in imaging high intensity nonlinear scatterers like ultrasound contrast agents compared to the classical methods.
However, imaging lower intensity nonlinear scatterers like micro-calcifications requires the use of higher manipulation pressures, causing the apparition of complex distortions of the imaging pulse neglected hitherto. In order to achieve a sufficient level of tissue suppression and detect the micro-calcifications using SURF imaging, these nonlinear forward propagation effects must be characterized, limited and/or compensated for.

(Problem description extracted from the thesis abstract)

Assignment given: 11. January 2010
Supervisor: Bjørn Atle J. Angelsen, ITK

Using SURF imaging for efficient detection of micro-calcifications

Bastien Emmanuel DENARIE, bastien.denarie@centraliens-nantes.net
Trondheim, June 6, 2010

NTNU
Faculty of Information Technology,
Mathematics and Electrical Engineering
Department of Engineering Cybernetics

Abstract

The presence of clustered micro-calcifications is an important indicator of early stage breast cancers, and an efficient real-time ultrasound imaging support is needed for conducting needle biopsies. SURF is a dual-frequency band ultrasound technique capable of imaging nonlinear scattering using the superposition of a low-frequency pulse to manipulate the tissue characteristics and an imaging pulse to extract the informations. This new technique has already demonstrated its superiority in imaging high intensity nonlinear scatterers like ultrasound contrast agents compared to the classical methods. However, imaging lower intensity nonlinear scatterers like micro-calcifications requires the use of higher manipulation pressures, causing the apparition of complex distortions of the imaging pulse neglected hitherto. In order to achieve a sufficient level of tissue suppression and detect the micro-calcifications using SURF imaging, these nonlinear forward propagation effects must be characterized and corrected for.

In this thesis, simulations have been conducted based on the geometry of the first manufactured prototypes of SURF probes, named Viglen and Okla.
The nonlinear propagation effects were described as the regroupment of a nonlinear propagation delay due the average level of LF manipulation pressure experienced by the HF pulse, a mix of compressions/expansions of the imaging pulse resulting from the fluctuations of the LF manipulation pressure over the HF pulse, and a phenomenon of SURF aberration due to the difference in the focusing and diffraction pattern of the HF and LF beams. The build-up of these nonlinear propagation effects were shown to be fully characterized by the combination of the profiles of the LF beam and the phase-relation between the two pulses.
The different beamforming strategies, with the superposition of a focused HF beam on a plane or co-focused LF beam, were also discussed: a net trade-off appears between the minimization of delays and SURF aberrations ensured by the co-focal configurations, and the minimization of compressions/expansions effects by using plane LF beams. A strategy to limit the nonlinear propagation effects would be the use of an especially designed transducer providing an excellent HF focusing in the study range and a sufficiently large LF aperture.

A filter was then designed and tested to ensure a correction of the pulse-form distortions in the received signals. The filter improved the level of suppression of the linear scattering from tissue by 15 dB in the numerical simulations, allowing a theoretical detection of the micro-calcifications and raising the resolution of the imaging system up to 1 dB close to the noise floor. The same filter demonstrated a smaller suppression of only 7 dB with the experiments conducted on phantoms, 2 dB below the limit required for detecting the smallest micro-calcifications.
Further work studying the pulse-form correction filter should be conducted to understand this difference in performances, along with a real-time implementation on the scanner, before achieving a correct detection of micro-calcification using SURF imaging.

Preface

This report is a result of my Master Thesis at the Department of Engineering Cybernetics (ITK) of the Faculty of Information Technology, Mathematics and Electrical Engineering (IME) of the Norwegian University of Science and Technology (NTNU). It was supervised by Professor Bjørn A.J. Angelsen and was carried out at the Department of Circulation and Medical Imaging (ISB) of the Faculty of Medicine (DMF). The report describes theoretical considerations, computer simulations and laboratory work carried out from January to June 2010.

Acknowledgments

I would like to thank Prof. Bjørn A. J. Angelsen for introducing me to medical ultrasounds and taking me under his supervision. Special thanks go to Post Doc Svein Erik Måsøy and PhD student Thor Andreas Tangen for being my daily advisors at ISB. They have always been available for help and guidance, taking time to answer questions, and full of motivation when it came to orienting my work. I also need to thank Jochen Deibele, Øyvind Standal and Tonni F. Johansen for all their help and suggestions during my laboratory work. The Master Thesis is the last piece of my *sivil ingeniør* studies at NTNU, and also the early start of my working life. I am very grateful to the persons who believed in me for the future, by offering me a place for an internship at the Ultrasound R&D department at GE Vingmed Oslo, and by welcoming me as a PhD student at the ISB department within the MILab structure: Geir Haugen and Arve Stavø from GE Vingmed, Olav Haraldseth from MILab, and my future supervisors Prof. Hans Torp and Post Doc Tore Bjåstad. Thank to everyone at the ISB department, the SURF group, and the MILab for all kinds of contributions. Last, I would like to thank my fellow students at ISB and the MR-center for making the hospital a warmer place.

Contents

List of Figures

List of Tables

List of Abbreviations

CTR	Contrast to Tissue Ratio, page 12
DMF	Faculty of Medicine, page iii
HF	High-Frequency imaging pulse, page 10
IME	Faculty of Information Technology, Mathematics and Electrical Engineering, page iii
ISB	Department of Circulation and Medical Imaging, page iii
ITK	Department of Engineering Cybernetics, page iii
LF	Low-Frequency manipulation pulse, page 10
MI	Mechanical Index, page 30
MLA	Multiple Line Acquisition, page 66
NC	Normalized Correlation, page 35
NTNU	Norwegian University of Science and Technology, page iii
RAD	Relative Amplitude Difference, page 42
RMS	Root Mean Square, page 42
RTS	Relative Tissue Suppression, page 42
SNR	Signal-to-Noise Ratio, page 24
SURF	Second-order UltRasound Field imaging, page 10
SURF TCI	Tissue Characteristcs Imaging, page 82
WLS estimator	Weighted Least Square estimator, page 20

Chapter 1

Introduction

1.1 Background and motivation

In modern countries, mammography has become a common procedure for breast cancer screening followed by every women above age 40. Early detection of the development of tumors is achievable by the research of micro-calcifications easily recognizable on x-ray pictures [1, 2], and allows a simpler and safer treatment via needle biopsy. But this biopsy operation is still needing for the assistance of an efficient, real-time, non-ionizing, flexible and cost-less imaging technique.

Since their early introduction for medical diagnostic purposes in the 1940's, it is precisely on the above cited advantages that ultrasounds have built their reputation, nowadays being the second most popular method for medical imaging. Ultrasounds, however, are also known to produce noisy images, with poor resolution and many artifacts... not ideal when it comes to detect micro-calcifications [3, 4].

But some recent improvements could reverse the deal. Nonlinear propagation of the ultrasound pulses has been exploited in harmonic imaging for improving both the accuracy and the resolution of the images [5]. The detection of ultrasonic contrast agents has motivated the study of nonlinear scattering, bringing in the images what could not be seen before [6]. With these discoveries, the complex theory of biomedical nonlinear acoustics had to be investigated formally and revolutionized the old models used by the ultrasound scanner manufacturers for B-mode imaging since the 1960's.

Dual-frequency band techniques [7, 8] come as a step even further, allowing the imaging of contrast agents to a higher frequency, by decoupling the ultrasound pulse into a low-frequency manipulation pressure and a high-frequency imaging pressure. Second order UltRasound Field (SURF) imaging is the concretization of such a dual-frequency method [9]. It has already shown its superiority to classical methods when it comes to imaging contrast agents [10], and its theoretical capabilities predict the possible detection and characterization of nonlinear scattering in tissues, including the imaging of micro-calcifications.

1.2 Purpose of this study

If the technological challenges of creating a dual-frequency band transducer have been accomplished [11], the possibilities offered by the SURF probes still have to be fully understood to be used adequately. Imaging schemes based on the Pulse Inversion technique [12] have been established, each of them exploiting a different possibility offered by the SURF method to improve the image [10], reduce artifacts such as aberrations [13], estimate strains [14], detect nonlinear scattering [15], or characterize the tissues [16]. But all these methods face a common problem. In order to be optimal, they need to have some information about the eventual degradations of the high-frequency imaging pulse [7].

The nonlinear propagation of a SURF pulse is the result of the complex interaction of two ultrasound fields, where distortions of the high-frequency imaging pulse will happen in a non-negligible way. It was first thought that the propagation of a SURF pulse could be summarized in the creation of a delay due to the manipulation pressure dependance of the speed of sound [17]. This model worked well for low levels of manipulation pressure, as the ones required for the detection of contrast agents, and an estimation and correction algorithm for this delays was designed and applied with success. However, for high levels of manipulation pressure such as the ones required for detection of micro-calcifications, a distortion characterized as a complex mix of compressions and expansions of the imaging pulse could not be neglected anymore [18].

The subject of this study is to characterize these complex distortions of the high-frequency imaging pulses: how are they generated, what are their impact on the reconstructed image when using the currently existing experimental SURF probes, and how can we minimize them? A second and major goal of this thesis is to develop and test a filter capable of compensating for this distortions, and allow a proper imaging of the nonlinear scattering from stiff particles such as micro-calcifications.

1.3 Structure of this paper

This report is the direct continuation of my Master Project [18], and tries to propose some solutions to the challenges raised in this previous paper. Even though this thesis has been built to be read independently, several references are done on the work conducted previously and the curious reader may be advised to briefly look at this production.

Chapter 2 introduces this paper on a theoretic level with a presentation of breast cancers and micro-calcifications, followed by a formal treatment of nonlinear ultrasounds propagation. The SURF technique and its abilities to image nonlinear scatterers are also presented.

Chapter 3 digs further into the mechanisms related to the SURF pulse complexes in order to get a better understanding of the phenomenons investigated in this report, and presents the theoretical aspects of the correction filters used in this study.

In Chapter 4, simulations of the nonlinear forward propagation of SURF pulse complexes were conducted based on the geometry and characteristics of the existing dual frequency band transducers Viglen and Okla. Such simulations allow a better understanding the phenomenons involved when using the SURF imaging techniques with high levels of manipulation pressures.

The signal distortions characterized in these last simulations have been corrected for in Chapter 5

using a filter specially designed to this purpose. The correction process is shown to play a major role in the imaging of micro-calcifications, while presenting some obvious limitations.

Due to the different problems they tackle, Chapters 4 and 5 may be considered as two papers based on the same theoretical introduction, but containing each their own presentation of methods, their results, as well as a thorough discussion. A common conclusion to this thesis and propositions for further work may be found in Chapters 6 and 7 respectively.

In the Appendixes, the attentive reader may found a presentation of additional results related to Chapter 4, as well as a water-tank study of the Okla probe, and some of the Matlab scripts created and used throughout this work.

Chapter 2

Motivations

2.1 Breast cancer

In modern countries, medical statistics have estimated that one women on eight will contract a breast cancer. Malign tumors are more likely to appear in breast tissues of women above age 40, and they represent 35% of the abnormalities detected in women breasts. Breast cancer is currently responsible for more than 30% of death by cancer in women, which is about 1% of all deaths worldwide. Men are also concerned by breast cancers since it represents 1.5% of all cancer death in men [1, 19, 20].

Though no formal causes have yet been assigned to the development of malignant tumor in breast tissues, numbers of treatments have been dedicated to cure breast cancer patients. Without possible prevention, current cancer treatments rest on early detections for reducing the mortality rate and the impact on the cured patients health. Early detection of breast cancer is especially important because the treatment of an undeveloped and non-metastasized tumor will not require massive surgical interventions.

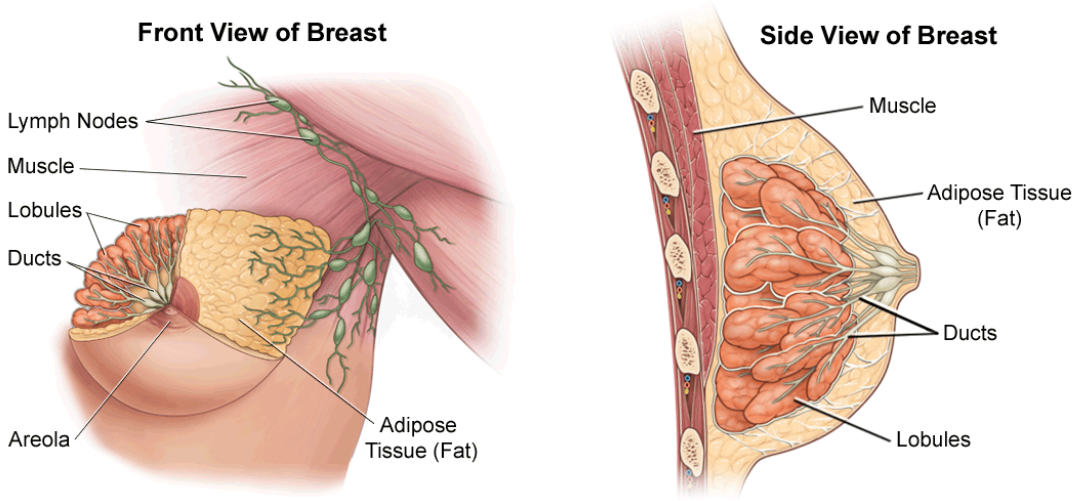

(a) (b)

Figure 2.1: Anatomy of the human breast

Breast cancer is characterized by malignant cell growth in the glandular tissue. The most com-

mon types of malignant breast tumors originate from either the epithelial cells of the milk ducts (ductal carcinoma, which represents 90% of all breast cancer) or lobules (lobular carcinoma) [21]. See Figure (2.1).

In an early stage called *in situ carcinomas*, the cancerous cells lose their normal regulation of differentiation and proliferation, but stay confined within the basement membrane of the duct or lobule. Most of the breast tumors in this situation corresponds to benign tumors [21]. However, approximately 35% of the malignant breast tumors will stay in this state of non-invasive cancers, and take the form of clusters of abnormal cells increasing the tissue stiffness [22]. In most of the malignant cases, though, the abnormal cells start to invade the surrounding breast tissue and eventually metastasize to distant organs, forming an invasive cancer.

When the cancerous cells start to divide at an abnormal rate, the numerous divisions will cause a residue in the form of specks of calcium, known as micro-calcifications [22]. These micro-calcifications may be observed on a mammogram as tiny white spots, thin linear branching or shell-like (See Figure (2.2)). Both benign and malicious breast cancers produce micro-calcifications, but in case of malignant tumors they are smaller, usually $\leq 0.5mm$ [23].

Clustered micro-calcifications is an important indicator of early stage breast cancers since it is a common feature of tumors found in the breast. This makes detection of micro-calcifications crucial for early breast cancer diagnosis, where lesions are still non-palpable by medical practitioners.

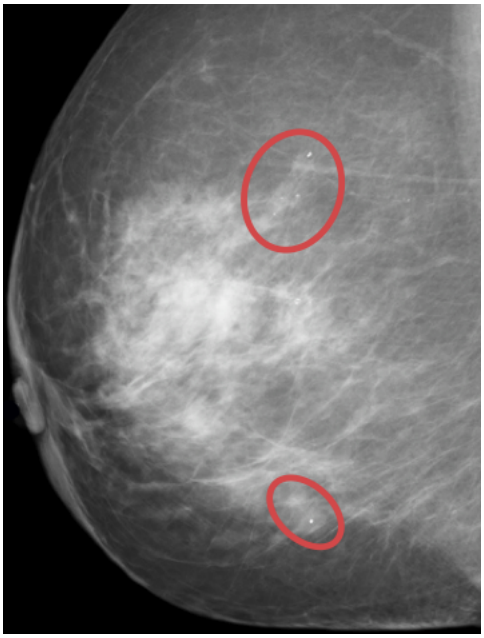

Figure 2.2: Breast mammography presenting six microcalcifications in the mammary ducts (in the areas circled in red).

Nowadays, mammography is the only standard tool used in breast cancer screening and is able to detect up to 90% of the cancers even before the tumor shows some symptoms [21]. Although mammography is a highly sensitive technique, it can not differentiate between benign and malignant breast micro-calcifications. Needle biopsy is therefore needed for extracting the micro-calcifications and characterizing the cancers. In cases of an early detection, the same kind of biopsy may be used to simply remove the cancerous clusters.

X-Ray mammography is a technique which provides an excellent image resolution, but with the drawbacks of being non-real-time, of being irradiating the breast tissues, and being uncomfortable for the patients. Needle biopsies currently lack for a safe, efficient, real-time imaging support for visualizing the micro-calcifications during the operation. Therefore, the recent progress in the field of ultrasound imaging, and especially in the study of the nonlinearities of the sound wave propagation, let the searchers hope for developing a method for imaging the smallest micro-calcifications in real-time.

2.2 Ultrasounds basic theory

Ultrasounds (US) waves is the name given to sound waves whith frequency over the humanly ear-able frequency band. For medical purposes, ultrasounds have been used for the past half-century for imaging the body and estimate organ and blood characteristics by using waves with frequency usually in the range 1MHz-50MHz. Today, ultrasonic imaging has become a standard medical procedure for patient diagnosis, and the recent developments in modern electronics offer medical ultrasounds an ever growing field of applications (pre-natal imaging, cardiac imaging, blood flow characterizations, ...).

The purpose of this report is not to describe the entire advancements in the field of ultrasound imaging, and we will therefore restrict ourselves to a condensed modeling of the nonlinear propagation and scattering of ultrasonic waves. The notations follow Angelsen [3]. A more thoroughfull background on the ultrasound imaging theory and the current technological methods used clinically may be found in [3], [4] or [24].

Defining

$$\underline{\psi}\left(\underline{r},t\right)\ ,\ \underline{u}\left(\underline{r},t\right)=\frac{\partial\underline{\psi}\left(\underline{r},t\right)}{\partial\underline{r}}\ ,\ p\left(\underline{r},t\right), \tag{2.1}$$

where $\underline{\psi}\left(\underline{r},t\right)$ is the particle displacement vector from an equilibrium position $\underline{r}$, $\underline{u}\left(\underline{r},t\right)$ the particle velocity, and $p\left(\underline{r},t\right)$ the acoustic pressure in a Lagrangian coordinate system.

The Newton acceleration law may be written for an ultrasonic plane wave:

$$\rho\frac{\partial\underline{u}}{\partial t}=-\nabla p, \tag{2.2}$$

where ρ is the mass density, and spatial and time coordinates are omitted for notational convenience. This equation is generally valid for beams with a smooth phase around the main propagation direction [4].

Lets now establish the constitutive material equation for an isotropic material with nonlinear elasticity. By doing a Taylor series expansion of the equation of state $P=P(\rho,s)$ along an isentrope $s=s_0$, where P is the pressure, tissue nonlinearities can be taken into account. Discarding terms of order higher than the second in the Taylor series expansion, the acoustic pressure is

$$p=A\frac{\rho_1}{\rho_0}+\frac{B}{2}\frac{\rho_1^2}{\rho_0^2}. \tag{2.3}$$

Here, ρ_0 is the density in the unstrained material while $\rho_1=\rho-\rho_0$. The acoustic pressure is defined as $p=P-P_0$ where P_0 is the ambient pressure, and the parameters A and B are defined as

$$A=\rho_0\frac{\partial P}{\partial\rho}\bigg|_{0,s}\ ,\ B=\rho_0^2\frac{\partial^2 P}{\partial\rho^2}\bigg|_{0,s} \tag{2.4}$$

where the subscripts in the partial derivatives indicate that they are evaluated at the unstrained state for an isentropic process. The following tissue elasticity equation may then be derived:

$$p\left(\underline{r},t\right)=-A\nabla\cdot\underline{\psi}\left(\underline{r},t\right)+A\beta_n\left(\nabla\cdot\underline{\psi}\left(\underline{r},t\right)\right)^2 \tag{2.5}$$

where β_n is a nonlinearity parameter defined as

$$\beta_n=1+\frac{B}{2A} \tag{2.6}$$

Lets now introduce the linear bulk compressibility $\kappa=1/A$, and notice that the relative compression in an ultrasound wave is $\frac{\delta V}{\Delta V}=-\nabla\underline{\psi}\left(\underline{r},t\right)$, we may rewrite (2.5) as the constitutive equation for the nonlinear tissue elasticity

$$-\frac{\delta V}{\Delta V}=\nabla\cdot\underline{\psi}\left(\underline{r},t\right)=-K\left(p\left(\underline{r},t\right)\right)-h_p\underset{t}{\otimes}\kappa p\left(\underline{r},t\right). \tag{2.7}$$

where $K\left(p\right)$ is a nonlinear elastic compressibility function for isentropic (very rapid) compression of the material and h_p represents the absorption. This equation describes the relation between the relative volume compression of a small volume of tissue with an applied acoustic pressure p. The elasticity function is conveniently splitted into a linear component dominant for small pressure amplitudes and a nonlinear component as

$$K\left(p\right)=\kappa p-K_n\left(p\right) \tag{2.8}$$

For fluid and soft tissue (which have elasticity close to water) we have seen that we could discard terms of order higher than the second in the Taylor expansion. It leads to the expression for $K\left(p\right)$ and $K_n\left(p\right)$ according to (2.5):

$$K\left(p\right)=\left(1-\beta_n\kappa p\right)\kappa p \tag{2.9}$$

$$K_n\left(p\right)=\beta_n\kappa^2p^2 \tag{2.10}$$

Defining the momentum potential ϕ as

$$\rho\underline{u}\left(\underline{r},t\right)=-\nabla\phi\left(\underline{r},t\right) \tag{2.11}$$

yields from (2.2)

$$p\left(\underline{r},t\right)=\frac{\partial\phi\left(\underline{r},t\right)}{\partial t}. \tag{2.12}$$

Combining equations (2.7)-(2.12), the wave equation for a homogeneous nonlinear tissue becomes the wave equation:

$$\nabla\left(\frac{1}{\rho}\nabla\phi\left(\underline{r},t\right)\right)-K'\left(p\left(\underline{r},t\right)\right)\frac{\partial^2\phi\left(\underline{r},t\right)}{\partial t^2}-h_p\underset{t}{\otimes}\kappa\frac{\partial^2\phi\left(\underline{r},t\right)}{\partial t^2}=0 \tag{2.13}$$

This expression of the wave equation is quite unintelligible and in order to go further, we need to characterize the tissue. We introduce spatial heterogeneity because soft tissues are composed of different material types (fat, muscle, connective tissue, ...) which gives spatial variations of the mass density and elasticity. We will model this heterogeneous material by separating the material parameters into a slowly varying (scale $\sim\lambda$) component (denoted with the subscript a

for average) and a rapidly varying component (denoted with the subscript f for fluctuations), i.e.

$$\rho(\underline{r}) = \rho_a(\underline{r}) + \rho_f(\underline{r}) \tag{2.14}$$
$$\beta_n(\underline{r}) = \beta_{na}(\underline{r}) + \beta_{nf}(\underline{r}) \tag{2.15}$$
$$K(\underline{r};p) = K_a(\underline{r};p) + K_f(\underline{r};p) \tag{2.16}$$
$$K_a(\underline{r};p) = \kappa_a(\underline{r})\,p - K_{na}(\underline{r};p) \tag{2.17}$$
$$K_f(\underline{r};p) = \kappa_f(\underline{r})\,p - K_{nf}(\underline{r};p) \tag{2.18}$$

By introducing $\gamma = \frac{\rho_f}{\rho}$ we see that

$$\frac{1}{\rho} = \frac{\rho_a}{\rho\cdot\rho_a} = \frac{\rho-\rho_f}{\rho\cdot\rho_a} = \frac{1}{\rho_a} - \frac{\gamma}{\rho_a}, \tag{2.19}$$

and inserting this into (2.13) and approximating $\nabla\rho_a \approx 0$, we get

$$\underbrace{\nabla^2\phi(\underline{r},t) - \frac{1}{c^2(\underline{r};p)}\frac{\partial^2\phi(\underline{r},t)}{\partial t^2}}_{\text{Nonlinear propagation}} - \underbrace{h_p \underset{t}{\otimes} \frac{1}{c_0^2}\frac{\partial^2\phi(\underline{r},t)}{\partial t^2}}_{\text{absorption}} \tag{2.20}$$
$$= \underbrace{\frac{\sigma_l(\underline{r})}{c_0^2}\frac{\partial^2\phi(\underline{r},t)}{\partial t^2} + \nabla\left(\gamma(\underline{r})\nabla\phi(\underline{r},t)\right)}_{\text{Linear scattering source terms}} - \underbrace{\frac{\sigma_n(p;\underline{r})}{c_0^2}\frac{\partial^2\phi(\underline{r},t)}{\partial t^2}}_{\substack{\text{Nonlinear scattering}\\ \text{source term}}}$$

where c_0 and c represent respectively the linear and nonlinear propagation velocities:

$$c_0(\underline{r}) = \frac{1}{\sqrt{\rho_a(\underline{r})\,\kappa_a(\underline{r})}} \tag{2.21}$$

$$\begin{aligned} c(\underline{r};p) &= \frac{1}{\sqrt{\rho_a(\underline{r})\,K_a'(\underline{r};p)}} \\ &= \frac{1}{\sqrt{\rho_a\kappa_a\left(1-2\beta_n\kappa_a p\right)}} \\ &\approx c_0\left(1+\beta_n\kappa_a p\right) \end{aligned} \tag{2.22}$$

and γ, σ_l and σ_n represent respectively the fluctuations in mass density, the linear and nonlinear fluctuations in compressibility:

$$\gamma(\underline{r}) = \frac{\rho_f(\underline{r})}{\rho(\underline{r})} \qquad\qquad \sigma_l(\underline{r}) = \frac{\kappa_f(\underline{r})}{\kappa_a(\underline{r})} \tag{2.23}$$

$$\begin{aligned} \sigma_n(\underline{r};p) &= \frac{K_{nf}'(\underline{r};p)}{\kappa_a(\underline{r})} \\ &= \left\{2\beta_{na}(2+\sigma_l)\,\sigma_l + \beta_{nf}(1+\sigma_l)^2\right\}\kappa_a p \\ &\approx 4\beta_{na}\sigma_l\kappa_a p \end{aligned} \tag{2.24}$$

The terms on the left hand side of (2.20) represent the propagation of the wave, while rapid spatial fluctuations of the coefficients of the right hand side are the sources for scattering. The

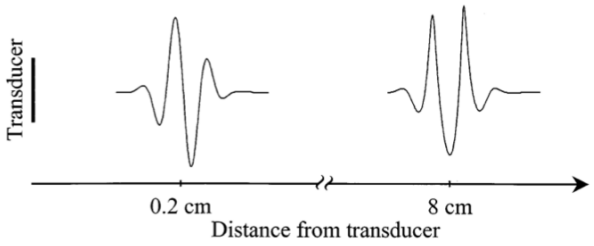

(a)

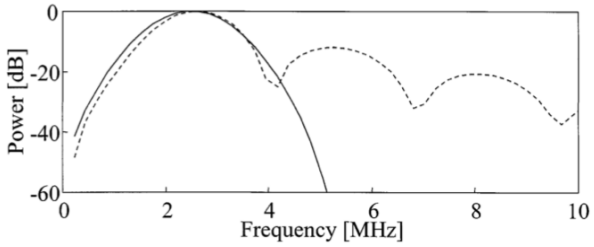

(b)

Figure 2.3: Distortion of an ultrasound pulse due to nonlinear propagation measured by a hydrophone in a water tank measurement: (a) change of shape of the ultrasound pulse as it propagates through water, (b) corresponding normalized spectra at 0.2 cm (solid line) and 8 cm (dashed line, with formation of higher harmonic) from the transducer. The transducer diameter was 28 mm, the frequency was 2.5 MHz, the focus was 75 mm and the peak negative pressure was 100 kPa. Figure is taken from [6].

wave velocity $c\left(\underline{r};p\right)$ is pressure dependent, this implies that the high pressure in the oscillation propagates with a higher velocity than the low pressure. This produces a nonlinear propagation distortion of the wave oscillations which accumulate with propagation distance and introduce higher harmonic frequency components in the propagation pulse. Figure 2.3 illustrates this distortion phenomenon of a pulse.

The finite size of the transducer introduces phase variations between the fundamental frequency and its harmonics, resulting in an asymmetry of the distorted wave (the peak compression exceeds the magnitude of the peak rarefaction) [5].

From (2.20) we can split the scattering source terms into linear scattering $-s_l$ (terms in first order of ϕ) and nonlinear scattering $-s_n$ (second order of ϕ),

$$-s_l\left(\underline{r},t\right)=\frac{\sigma_l\left(\underline{r}\right)}{c_0^2}\frac{\partial^2\phi\left(\underline{r},t\right)}{\partial t^2}+\nabla\left(\gamma\left(\underline{r}\right)\nabla\phi\left(\underline{r},t\right)\right) \tag{2.25}$$

$$-s_n\left(\underline{r},t\right)=-\frac{\sigma_n\left(p;\underline{r}\right)}{c_0^2}\frac{\partial^2\phi\left(\underline{r},t\right)}{\partial t^2}. \tag{2.26}$$

Linear scattering is the combination of a monopole scattering component due to the variations in volume compressibility $\sigma_l=\kappa_f/\kappa_a$ and a dipole scattering component due to the variations in mass density $\gamma=\rho_f/\rho$. From (2.24), we may observe that the nonlinear scattering σ_n is proportional to the linear scattering term σ_l with $4\beta_{na}\kappa_a p=4\beta_{na}\kappa_a\frac{\partial\phi}{\partial t}$ as a proportional constant.

The nonlinear heterogeneous wave propagation equation (2.20) is complex and must be solved by numerical simulations, as we will see later when using ABERSIM. Typical values for the different parameters presented above in soft tissue are given in Table 2.1.

Table 2.1: Typical acoustic parameters values for soft tissues

c_0 m/s	ρ_a kg/m^3	ρ_f kg/m^3	κ_a $10^{-12}\text{Pascal}^{-1}$	κ_f $10^{-12}\text{Pascal}^{-1}$	β_{na}	β_{nf}	σ_l
1440 - 1560	1010	$\pm$ 60	450	$\pm$ 55	4.9	1.5	$\pm$ 0.12

2.3 SURF Imaging principles

Second-order UltRasound Field imaging, abbreviated SURF imaging, is a technique developed at the Department of Circulation and Medical Imaging (ISB), NTNU. It is based on the transmission of dual-frequency band pulses from the same acoustic source using a low-frequency (LF) manipulation pulse and a high-frequency (HF) imaging pulse, typically having a frequency separation in the order of 1:8-10. The two pulses are wide-band, usually with a length less than 4 periods. The purpose of the LF pulse is to manipulate the scattering and propagation of the HF imaging pulse, and is only transmitted and not received. The HF imaging pulse is then used to image tissue or nonlinear scatterers under the influence of the manipulation pulse.

Dealing with a dual frequency ultrasound signal has been explored by some scientific teams during the last decades without a net and clinically applicable success, mainly due to the complexity of achieving the transmission of such a signal. However, dual-frequency techniques offers new possibilities in reducing ultrasonic aberrations, improving image quality via synthetic beamforming, characterizing tissues, or estimating the nonlinear scattering from sources such as contrast agent (micro-bubbles) or micro-calcifications. In our study, we will restrict ourselves to the imaging of nonlinear scatterers such as micro-calcifications with the SURF imaging technique.

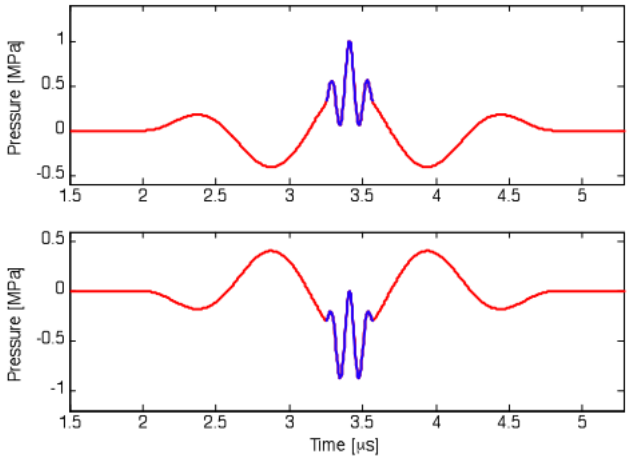

Figure 2.4: Illustration of two different SURF-pulse complexes.

SURF imaging is based on the transmission of two overlapping wide-band pulses (see Figure 2.4). In the upper panel, the imaging pulse is placed in a compression phase of the manipulation pulse, while in the lower panel the imaging pulse is placed in a rarefaction phase of the manipulation pulse. The combination of these two pulse schemes, where the HF pulse travels on the peak or on the trough of the LF pulse is very important in SURF imaging and they will therefore be called respectively positive and negative SURF-pulse complexes.

Imaging of nonlinear scatterers with SURF technique is done with a scheme inspired by the Pulse Inversion technique done in ultrasound contrast agent imaging [12]:

1. Transmit successively two successive pulse complexes where the high frequency imaging pulse travels respectively on the peak and on the trough of the manipulation pulse.
2. Receive the scattered signal for each pulse complex as in classical B-mode imaging.
3. Apply a bandpass filter to keep only the high frequency signal components.
4. Subtract the two HF-filtered signals, this produces a signal which represents only the nonlinear components of the scattered signals.

In order to understand this scheme, we must refer to (2.24) and (2.26) for expressing the nonlinear scattering,

$$-s_n\left(\underline{r},t\right) \approx -\frac{1}{c_0^2}\left[4\beta_{na}\left(\underline{r}\right)\sigma_l\left(\underline{r}\right)\kappa_a\left(\underline{r}\right)\right]p\left(\underline{r},t\right)\frac{\partial^2\phi\left(\underline{r},t\right)}{\partial t^2}. \tag{2.27}$$

We remark that the nonlinear scattering s_n is proportional to the second order product $p\cdot\frac{\partial^2\phi}{\partial t^2}$. For a better understanding of SURF imaging, we separate the pressure into two components, $p = p_m + p_i$, where p_m represents the low-frequency manipulation pulse pressure and p_i the high-frequency imaging pulse pressure. The momentum potential ϕ is directly linked to the pressure via (2.11) and may also be separated in $\phi = \phi_m + \phi_i$. The nonlinear scattering for a SURF pulse complex is therefore proportional to the product

$$\left(p_m + p_i\right)\cdot\left(\frac{\partial^2\phi_m}{\partial t^2} + \frac{\partial^2\phi_i}{\partial t^2}\right) \tag{2.28}$$

Due to the SURF frequency ratio of 1:8-10 and the HF bandpass filtering on receive, we may neglect in our product the terms in $\frac{\partial^2\phi_m}{\partial t^2} = \frac{\partial p_m}{\partial t}$ compared to the terms in $\frac{\partial^2\phi_i}{\partial t^2}$. Placing the imaging pulse successively on the peak and on the trough of the manipulation pulse, i.e. inverting the LF-pulse polarity, we will obtain two scattered signals proportional to the products

$$\left(p_m + p_i\right)\cdot\frac{\partial^2\phi_i}{\partial t^2} \qquad \text{and} \qquad \left(-p_m + p_i\right)\cdot\frac{\partial^2\phi_i}{\partial t^2} \tag{2.29}$$

The scattering after subtraction of the two received signals will therefore be proportional to

$$2\cdot p_m\cdot\frac{\partial^2\phi_i}{\partial t^2}. \tag{2.30}$$

The nonlinear scattering properties of the tissue are extracted by the imaging pulse ($\frac{\partial^2\phi_i}{\partial t^2}$) with the magnitude allowed by the manipulation pulse (p_m).

2.4 Theoretical requirements for detection of micro-calcifications

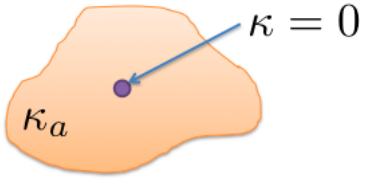

Figure 2.5: Illustration of an incompressible micro-calcification in homogeneous soft tissue of linear bulk compressibility κ_a.

Micro-calcifications are incompressible clusters of calcium particles surrounded by compressible tissue (see Figure 2.5). Our notation of of the linear bulk compressibility in the form $\kappa(\underline{r}) = \kappa_a(\underline{r}) + \kappa_f(\underline{r})$ will therefore be:

$$\kappa(\underline{r}) = 0 \qquad \Rightarrow \qquad \kappa_f(\underline{r}) = -\kappa_a(\underline{r}) \tag{2.31}$$

Using (2.31) and the usual values of the parameters for soft tissues listed in Table 2.1 we can easily compute the scattering coefficients for a manipulation pulse of amplitude 1 MPa:

$$\sigma_l = \frac{\kappa_f}{\kappa_a} = -1 \qquad \text{and} \qquad \sigma_n^{\text{calcif}} \approx 4\beta_{na}\sigma_l\kappa_a p \approx -8.82 \cdot 10^{-3} \tag{2.32}$$

The monopole and dipole sources of linear scattering of (2.25) can be merged in the study of back-scattering according to [4, eq. (7.229) and (7.288)] in a single component:

$$\upsilon_b(\underline{r}) = \sigma_l(\underline{r}) - \gamma(\underline{r}) = (1 - \gamma_{\sigma_l})\,\sigma_l(\underline{r}) \approx 1.3 \cdot \sigma_l(\underline{r}) \tag{2.33}$$

For soft tissue, we know that $\sigma_l \approx 0.12$ and therefore $\upsilon_b^{\text{tissue}} \approx 0.156$. We can also compute the average nonlinear scattering component for soft tissue, $\sigma_n^{\text{tissue}} \approx 1.76 \cdot 10^{-3}$.

Up to now, we have computed the intensity of the different scattering types (linear and quadratic) for soft tissue and micro-calcification. In order to draw some conclusions from these values, a comparison is needed. As human perception, the perception of a signal compared to an other follows a logarithmic rule, and we will therefore compare the previous values as logarithmic ratios of the received intensities:

$$\frac{\text{nonlinear scattering of tissue}}{\text{linear scattering of tissue}} = 20\log\left(\frac{\sigma_n^{\text{tissue}}}{\upsilon_b^{\text{tissue}}}\right) = -38.9 \text{ dB} \tag{2.34}$$

$$\frac{\text{nonlinear scattering of micro-calcification}}{\text{linear scattering of tissue}} = 20\log\left(\frac{\sigma_n^{\text{calcif}}}{\upsilon_b^{\text{tissue}}}\right) = -24.9 \text{ dB} \tag{2.35}$$

$$\tag{2.36}$$

The above ratios show that in order to extract all the nonlinear scattering components of the received signal, we have to manage in suppressing the signal due to linear scattering of tissue by at least 39 dB. For appropriate detection of micro-calcifications, however, the required linear tissue suppression is reduced to 25 dB. If we manage to get this perfect suppression, the best Contrast to Tissue Ratio (CTR) achievable will be $39 - 25 = 14$ dB for micro-calcifications as contrast agent.

Note also that in order to obtain a sufficient level of nonlinear scattering from the micro-calcifications, a manipulation pressure of magnitude 1 MPa has been used. This level of low-frequency amplitude is high compared to the 0.1MPa used for the detection of contrast agent, and the consequences on the high-frequency pulse propagation are, as we shall see, not negligible.

These observations are quite drastic because the suppression of linear tissue in the SURF imaging technique is based on the subtraction of the two HF bandpass-filtered signals as seen in the previous section, and if the signals are not perfectly aligned (same p_i in the left and the right parts of (2.29)), the limit of 25 dB of suppression will never be reached. And unfortunately for us, we will see in the next chapter that the nonlinear propagation of the SURF pulse complexes makes it really hard to achieve a perfect alignment of the HF-filtered pulses.

Chapter 3

Challenges of the current SURF imaging method

3.1 Nonlinear propagation effects

In Chapter 2, we have seen that imaging nonlinearities using SURF is based on the subtraction of two high-frequency bandpass filtered pulses of opposite manipulation polarity. In the absence of nonlinear scatterers, these two HF-filtered received signals should be equal and perfectly aligned. However, we will see that the nonlinear propagation of the imaging pulse on the peak or on the trough of the manipulation pulse will induce delays, compression/expansion and focusing aberration of the imaging pulse.

3.1.1 Nonlinear propagation delays

Using a dual-frequency band pulse, it is convenient to analyze the propagation velocity $c(p)$ by separating the pressure into two components, $p = p_m + p_i$, where p_m represents the low-frequency manipulation pulse pressure and p_i the high-frequency imaging pulse pressure. Inserting this components into the nonlinear propagation velocity (2.22), and discarding the spatial dependency on $\underline{r}$ for readability, gives

$$c\left(p_m, p_i\right) \approx c_0 \left(1 + \beta_{na}\kappa_a p_m + \beta_{na}\kappa_a p_i\right) \tag{3.1}$$

The two last terms in (3.1) generate nonlinear distortion of the manipulation and imaging pulses. In addition to it's own harmonic distortion, the imaging pulse will experience a local change in the speed of sound proportional to the manipulation pulse pressure p_m. By introducing the imaging pulse intrinsic velocity as the velocity of an imaging pulse propagating without manipulation pulse,

$$c_i\left(p_i\right) = c_0 \left(1 + \beta_{na}\kappa_a p_i\right), \tag{3.2}$$

the nonlinear sound propagation velocity (3.1) may be reduced (by omitting second order terms) to

$$c_i\left(p_m, p_i\right) \approx c_i\left(p_i\right)\left(1 + \beta_{na}\kappa_a p_m\right). \tag{3.3}$$

The pressure dependance of the propagation velocity has a direct impact on the propagation of the SURF pulse complexes. An imaging pulse placed on a peak of the manipulation pulse will

travel faster than the same imaging pulse placed on a trough of the manipulation pulse. The two imaging pulses will thus be delayed from each other. See Figure 3.1.1.

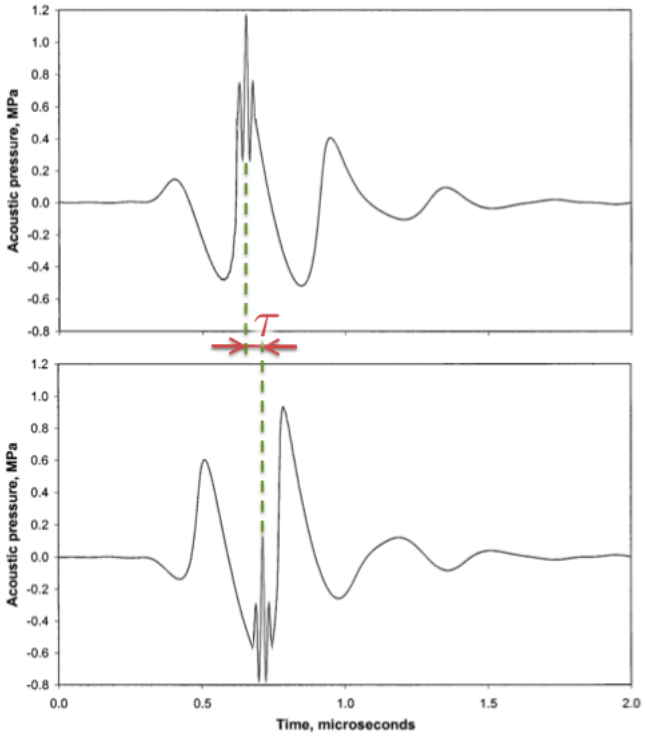

Figure 3.1: Illustration of the nonlinear propagation delay τ (exaggerated here) between the imaging pulse propagating on a peak and a trough of the manipulation pressure

This delay τ may be expressed mathematically, using the time/depth relationship of the HF-imaging pulse

$$t(z) = \int_{\Gamma(z)} \frac{ds}{c_i\left(p_m(s), p_i(s)\right)} = t_0(z) + \tau(z) \tag{3.4}$$

where $\Gamma(z)$ is the propagation path of the imaging pulse to and from a scatterer at depth z, t_0 is the propagation lag without LF manipulation, i.e., for conventional imaging, and τ is the added nonlinear propagation delay due to the presence of an LF manipulation pressure p_m. For conventional back-scatter imaging, the unmodified propagation lag is given by the total propagation length of $2z$ so that

$$t_0(z) = 2\int_0^z \frac{ds}{c_i\left(p_i(s)\right)} \tag{3.5}$$

For the added nonlinear propagation lag, however, the LF manipulation pressure drops so much in the back-scattered direction that nonlinear propagation effects are negligible, and we thus only get contribution as long as the HF-imaging pulse follows the high-amplitude forward-propagating manipulation pulse:

$$\tau(z) = -\int_0^z \frac{ds}{c_i\left(p_i(s)\right)} \beta_{na}(s)\kappa_a(s)p_m(s) \tag{3.6}$$

3.1.2 Compression / expansion of the imaging pulse

With a frequency ratio of 1:8-10 between the manipulation and imaging pulses, the low-frequency pressure experienced by the high-frequency pulse will vary across the imaging pulse length. The effect of the manipulation pulse on the imaging pulse will therefore not be uniform in all parts of the pulse: this difference in the manipulation pressure p_m will drive some parts of the imaging pulse faster than others, and cause a relative compression/expansion of the pulse.

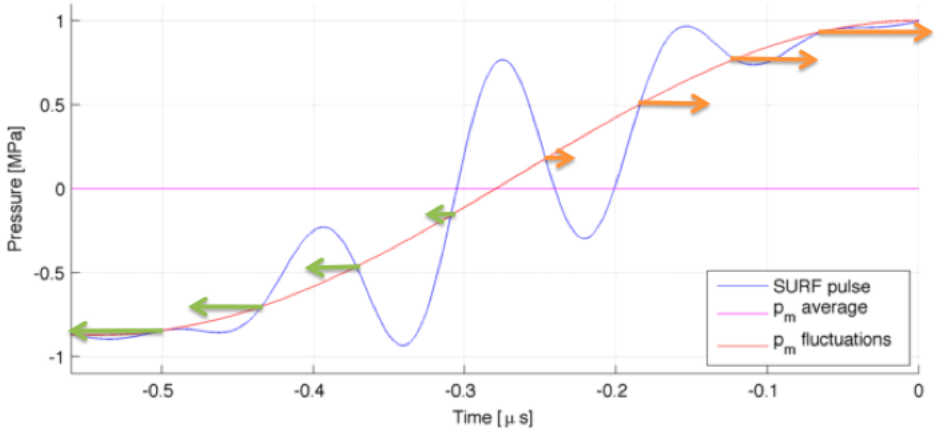

Figure 3.2: Illustration of the compression / expansion due to the propagation of the imaging pulse on a varying manipulation pressure. The arrows represent the local increases in velocity due to manipulation pressure. In this situation, the imaging pulse is located on a flank of the manipulation pulse, and the positive gradient induced by the manipulation slope will here induce an expansion of the pulse.

The compression / expansion effects occurring during the nonlinear propagation of a dual-frequency band pulse has first been analyzed by H. Fukukita in [8], where it has been used for an estimation of the nonlinearity parameter. In essence, the compression / expansion phenomenon may be visualized as a displacement of the crossings (called nodes) of the filtered low-frequency manipulation pressure by the the superposed high-frequency imaging pulse. This description is illustrated in Figure 3.2, and allows a simple understanding of this complex phenomenon.

The imaging pulse is relatively short compared to the LF wavelength, we can therefore split the manipulation pressure into two components, $p_m = p_{ma} + p_{mf}$. The average pressue p_{ma} will contribute to an accumulated delay while the varying part will give compression expansion of the pulse compared to a pulse propagating without any manipulation pressure. The delays and compression/expansion can be denoted *nonlinear propagation effects* and are of special interest for our study.

3.1.3 Aberration within the HF pulse

The term *aberration* is used in ultrasound imaging to describe the degradation of the beam ideal focusing due to spatial variations in the ultrasound propagation velocity. This phase-front aberration leads to a wrong focusing of the beam along with increased sidelobes, leading to the reduction of both spatial and contrast resolution in the image.

Transmitting a composite band pulse, the difference between the focusing and diffraction pattern from the LF and HF beams will introduce a similar phenomenon, called *SURF aberration*.

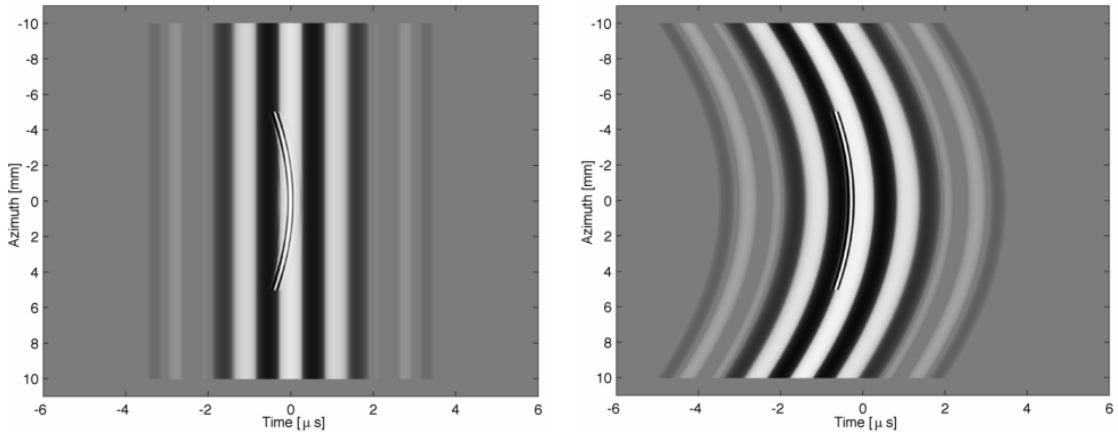

(a) (b)

Figure 3.3: Illustration of the SURF aberration phenomenon. Abersim simulated positively manipulated SURF pulses on an annular array transducer surface (depth z = 0), for a HF beam focused at 20 mm and a (a) plane wave LF beam (b) a co-focused LF beam. White parts correspond to positive pressures (compression) while darker parts correspond to negative pressures (rarefaction). Figures are taken from [18].

In order to understand this phenomenon, consider the simulated SURF pulse in Figure 3.3(a), where a setting using a focused high-frequency beam superposed on a plane low-frequency beam is illustrated. The HF pulse is smaller and located on the middle of the LF pulse, mainly on a compression phase. However, one can notice that along the azimuth direction, the high-frequency pulse is not equally located on the LF peak: for azimuth $x > 2mm$, the HF pulse lies on the LF pulse flank, and is even located on a trough of the LF pulse for $x = \pm 5mm$. This difference in phase relation between the two pulses along the azimuth direction is due to the different focusing pattern of the pulses. Such different experienced manipulation pressures by the HF pulse along the azimuth direction will result in different nonlinear propagation delays: the central part (in azimuth) of the HF pulse will travel faster than the sides of the pulse. The difference in the focusing pattern of the two pulses introduce a difference in the propagation speed inside the HF pulse, and thus result in an aberration phenomenon.

Consider now Figure 3.3(b), where a co-focused SURF pulse is presented. The HF pulse is now located on the flank of the LF manipulation pulse, with a constant phase relation between the two pulses along the azimuth direction: the two pulses have the same focusing pattern. However, these pulses have a significant difference in center frequency, and thus a significant difference in diffraction pattern. In order to put this remark on more formal terms, we can look at the expression of the Fresnel parameter for an annular array given in [3, chap. 5].

$$S = \frac{4f_{\#}}{D/\lambda}, \tag{3.7}$$

where $f_{\#} = F/D$ is the f-number, D is the diameter (aperture) of the array, and λ is the ultrasound wavelength. The Fresnel parameter describes the diffraction and focusing characteristics of an array. A low Fresnel parameter, practically in the order of 0.1 to 0.3, provides efficient focusing of the array. In our example, the Fresnel parameters for the LF and HF arrays are respectively $\{0.34, 0.15\}$ (see [18, chap. 5.2]). Therefore, the HF beam is efficiently focused while the LF beam has a poor focusing. The LF beam will thus result in an effective focus position closer to the transducer than the geometric focus of the beam (depth $z = 20mm$). In this situation, the high-frequency pulse has a constant phase relation along the azimuth direction with

the low-frequency pulse at the transducer surface (depth $z = 0mm$) ; but due to the difference in the diffraction pattern of the two pulses, the perfect geometrical alignment of the pulses will no longer exist for depths $> 0mm$, and the difference in phase-relation introduced across the HF pulse will result once again in an aberration phenomenon.

These examples illustrated the formation of SURF aberrations when the LF and HF beams present a difference in their focusing or diffraction patterns. The intensity of such aberrations will be function of the manipulation pressure amplitude (introducing different propagation speeds) as well as the difference in the type and quality of focusing between the two pulses.

3.1.4 Nonlinear propagation effects build-up and correction

We have described three nonlinear propagation effects in SURF pulses: propagation delays, compressions/expansions and SURF aberrations. The magnitude of this effects have all been shown to be dependent on the low-frequency manipulation pressure. As previously mentioned for the propagation delays, the LF manipulation pressure drops so much in the back-scattered direction that nonlinear propagation effects are negligible on the way back to the probe. The study of nonlinear propagation effects can therefore be limited to the study of the *forward* propagation of the SURF pulse.

In order to image nonlinearities in soft tissues, the ideal SURF imaging procedure has to be adapted, otherwise it will mix up the nonlinear propagations effects and the nonlinear scattering, producing an incorrect result. A compensation for the nonlinear propagation effects is introduced before subtracting the signals from positive and negative pulse complexes in the SURF imaging procedure presented in Chapter 2.3.

To illustrate this compensation mathematically, one may consider the following signal model for a received echo from a HF pulse with no manipulation pressure:

$$s\left(t\right) = x_l\left(t\right) + n\left(t\right) \tag{3.8}$$

where n is uncorrelated noise. By applying a manipulation pressure and combining the nonlinear wave equation (2.20) and (3.8), the received HF-filtered echo from a SURF complex can be modeled as

$$s_k(t) = h_k\left(t\right) \otimes x_l\left(t + \alpha_k \tau_n\left(t\right)\right) + \alpha_k h_k\left(t\right) \otimes x_n\left(t + \alpha_k \tau_n\left(t\right)\right) + n_k\left(t\right) \tag{3.9}$$

where α_k is the polarity of the manipulation pressure for pulse k ($\alpha_1 = 1$ and $\alpha_2 = -1$ respectively denoting the positively and negatively manipulated HF imaging pulses), τ_n is the nonlinear propagation delay, h_k is a filter which incorporates the compression/expansion of the pulse and x_l and x_n is the linear and nonlinear scattered signal respectively.

If we want extract the nonlinear scattering as presented in the SURF imaging procedure, one must compensate for the effects of both τ_n and h_k before subtracting the signals s_1 and s_2. As for a vast majority of cases in signal processing, this correction is more easily presented in the Fourier domain. Taking the Fourier transform of the signals over an interval T_i around time t_i where the delay and pulse distortion are assumed to be approximately constant ($\forall t \in T_i$, $\tau_n\left(t\right) = \tau_{n,i}$ and $h_k\left(t\right) = h_{k,i}\left(t\right)$), the signal in (3.9) becomes

$$S_{k,i}\left(\omega\right) = H_{k,i}\left(\omega\right) X_{l,i}\left(\omega\right) e^{j\alpha_k \omega \tau_{n,i}} + \alpha_k H_{k,i}\left(\omega\right) X_{n,i}\left(\omega\right) e^{j\alpha_k \omega \tau_{n,i}} + N_{k,i}\left(\omega\right) \tag{3.10}$$

Applying the SURF imaging two pulse scheme, one may see that correction may be applied to the received signals before subtraction, such as the linear scattering can be suppressed and the nonlinear scattering detected:

$$\hat{X}_{n,i}(\omega) = \frac{1}{2}\left[\hat{H}_{1,i}^{-1}(\omega) S_{1,i}(\omega) e^{-j\alpha_1 \omega \hat{\tau}_{n,i}} - \hat{H}_{2,i}^{-1}(\omega) S_{2,i}(\omega) e^{-j\alpha_2 \omega \hat{\tau}_{n,i}}\right] \tag{3.11}$$

In order to achieve such a correction, one must first estimate for each time/depth interval T_i the nonlinear propagation delay $\hat{\tau}_{n,i}$ as well as the pulse-form distortion characteristics $\hat{H}_{k,i}(\omega)$ for $k = 1, 2$.

3.2 Phase relation: a key factor in understanding the nonlinear propagation effects build-up

We already mentioned that the LF manipulation pressure contributed by it's average p_{ma} value to the formation of an accumulated delay, while the fluctuations p_{mf} induced a complex distortion of the imaging pulse shape as a mix of compressions and expansions. We shall call the fluctuations p_{mf} the *gradient* induced on the imaging pulse by the manipulation pulse. In order to fully understand the build-up of the nonlinear propagation phenomenons, we need to be in measure of estimating variations of the manipulation pressure along with the propagation depth z: $p_m(z) = p_{ma}(z) + p_{mf}(z)$.

SURF pulse complexes do not propagate from the transducer to the focus in their ideal shape presented in Figure 2.4 (ideal in the sense that the imaging pulse is located perfectly on a peak or trough of the manipulation pulse). In any focused system, the propagation will induce a phase shift of the signal from the transducer to the signal. In the case of dual-frequency band pulses, this will cause the imaging pulse to slide on the manipulation pulse, e.g. starting from the flank to reach the peak or trough in focus.

In order to illustrate this phase-shift and the importance of following the alignment, i.e. the phase relation, of the imaging and manipulation pulses, a good idea is to look at the linearized and idealized expression of the pressure of a focused transducer. By dropping the nonlinear terms and absorption in (2.20), the linear wave equation takes the form

$$\nabla^2 \phi - \frac{1}{c_0^2}\frac{\partial^2 \phi}{\partial t^2} = 0 \tag{3.12}$$

Working through Helmholtz-Kirchoff's formula, the Rayleigh integral for a plane vibrating surface in a rigid baffle can be written in the frequency domain as [3, chap. 4-5]

$$\hat{\phi}(\underline{r}, \omega) = \hat{h}(\underline{r}, \omega)\, \hat{f}(\omega) \tag{3.13}$$

where

$$\hat{h}(\underline{r}, \omega) = \rho U_n \int_A dr_0^2 \frac{e^{-ik|\underline{r} - \underline{r_0}|}}{2\pi |\underline{r} - \underline{r_0}|} \tag{3.14}$$

Here, $\hat{h}(\underline{r}, \omega)$ is the spatial frequency response, $\underline{r}$ the field coordinate, $\underline{r_0}$ a point on the vibrating surface, $\hat{f}(\omega)$ the Fourier transform of the time excitation, $k = \omega/c$ the wave number, ρ the homogeneous medium mass density, A the vibrating surface area, and U_n the normal velocity amplitude of the vibrating surface, assuming a constant velocity distribution (no apodization).

At the focal point of the vibrating surface, $|\underline{r} - \underline{r_0}| \equiv F$ the focal distance, and the saptial impulse frequency response becomes

$$\hat{h}(F,\omega) = \rho U_n \frac{e^{-ikF}}{2\pi F} \int_A dr_0^2 = \rho U_n \frac{e^{-ikF}}{2\pi F} A. \tag{3.15}$$

Using the relation between the momentum potential and pressure (2.12)

$$p(\underline{r},t) = \frac{\partial \phi(\underline{r},t)}{\partial t} \qquad \longleftrightarrow \qquad \hat{p}(\underline{r},\omega) = i\omega \hat{\phi}(\underline{r},\omega), \tag{3.16}$$

gives the expression of the pressure in the focal point of the vibrating surface as

$$p(F,t) = \frac{\partial}{\partial t}\left\{ f\left(t - \frac{F}{c}\right)\right\} \frac{\rho U_n A}{2\pi F} \qquad \longleftrightarrow \qquad \hat{p}(\underline{r},\omega) = i\omega \hat{f}(\omega)\, \rho U_n \frac{e^{-ikF}}{2\pi F} A. \tag{3.17}$$

Equation (3.17) shows that the time excitation at the focal point of a vibrating surface is the derivative of the transmit excitation (or $\pi/2$ phase-shifted in the frequency domain).

This ideal linear situation presented above reflects the presence of a phase-shift in any focused configuration. If we assume that the manipulation and imaging arrays are coaxial and have the same focal point, (3.17) shows that in order to position the imaging pulse on a peak or a trough of the manipulation pulse at the focal point of the array, the imaging pulse must be transmitted on the flank of the manipulation pulse (in the idealized linear case, it should be in the position of zero manipulation pressure). The imaging pulse will travel on a changing manipulation pressure and experience the equivalent of a $T_m/4$ slide, where T_m is the period of the manipulation pulse, from the array surface to the focal point. This initial placement of the imaging pulse on a flank of the manipulation pressure is illustrated on Figure 3.4

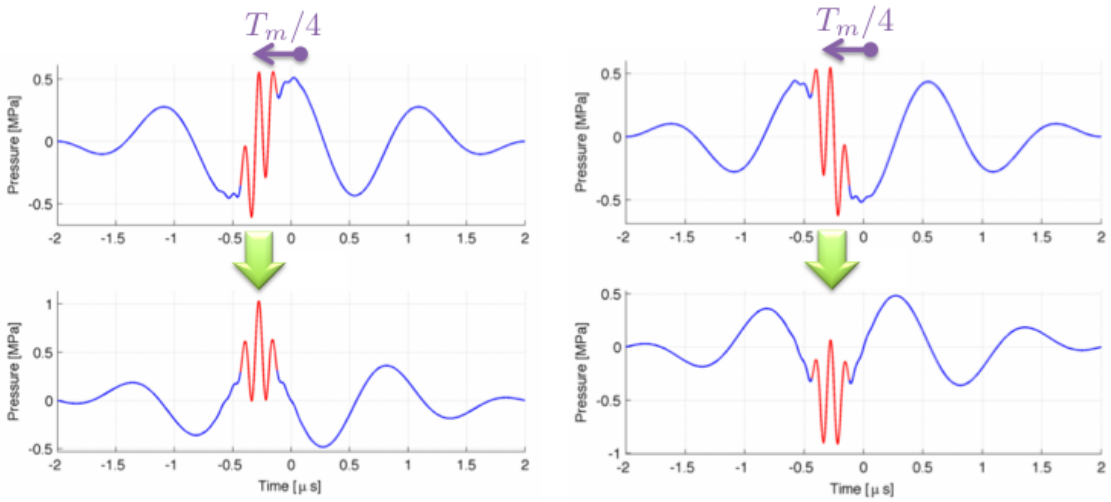

(a) (b)

Figure 3.4: Illustration of the placement of the imaging pulse relative to the manipulation pulse in an idealized situation, on the transducer (top) and in focus (bottom). The concept is presented for an imaging pulse placed on (a) a positive gradient and (b) a negative gradient. The pressure scale is not respected since the pulse pressures are normalized.

For the sequel, we shall call *phase relation* the distance between the maximum of the envelope of the HF-imaging pulse and the nearest peak/trough of the LF-manipulation pulse. As we just

showed, we should expect this phase relation to be in the range $[0, T_m/4]$ between the transducer surface and the focal distance F, for a situation where the LF array is focused.

The nonlinear propagation of a SURF pulse is quite complex. As we have already explored in [18, chap. 5], the phase relation between the imaging and manipulation pulses depends on the configuration setup used to transmit the pulse. In real cases, is not restricted to the ideal $[0, T_m/4]$ range, and may oscillate before reaching the goal presented in Figure 2.4. This will cause the imaging pulse to slide back and forth relatively to the closest manipulation pressure peak/trough, and will impose different experienced pressures and experienced gradients building up the complex distortion that we call usually call the delay and compression/expansion phenomenons.

Along with the beam characteristics, the depth variation of the phase relation between the HF and LF pulse contains all the information about the build-up of the nonlinear propagation effects. However, the depth profile of the phase relation can only be established by simulation or laboratory experiments such as water-tank recordings. If the phase relation is useful for us to characterize the nonlinear propagation delays and the compression/expansion phenomenon, it may not be estimated from conventional RF-data recorded by an ultrasound scanner. Since the nonlinear propagation effects have a non negligible negative impact on the imaging resolution of the system, they must be either minimized by looking for the best beam-configuration setup, either estimated and corrected for using a "close to real-time" algorithm.

3.3 Estimation and correction of the propagation delays

We have seen that the nonlinear propagation of the manipulation pulse will induce a delay between the imaging pulses located in a compression phase (peak) and a rarefaction phase (trough) of the manipulation pressure. We do only treat the high frequency band corresponding to scattering created by the imaging pulse. Therefore, the two received signals in the SURF imaging scheme will be delayed to each other with a delay varying with depth, i.e. with time.

In order to compensate for these nonlinear delays, a real-time algorithm has been established ([17] and [25]). The algorithm first estimates the nonlinear propagation delay at each time step using a Weighted Least-Square (WLS) estimator described below and corrects the two signals of this delay using a standard linear interpolation scheme.

We will now present the process used to estimate the nonlinear propagation delays.

3.3.1 Delayed received signals model

We represent our received signal as a complex band-limited 1D signal with real positive amplitude, a, center frequency, ω_c, modulating phase, φ, and time-varying subsample delay, $\tau(t)$,

$$s(t) = a(t) \exp\left[i(\varphi(t) + \omega_c t)\right] \tag{3.18}$$

The instantaneous frequency $\theta(t)$ of the signal $s(t)$ is defined as the time derivative of the argument, i.e. $\theta(t) = \frac{d}{dt}\left[\arg s(t)\right]$. Thus, considering the definition (3.18) of our signal, we have:

$$\theta(t) = \frac{d}{dt}\left[\varphi(t) + \omega_c t\right] = \dot{\varphi}(t) + \omega_c \tag{3.19}$$

Without loss of generality, assume symmetric delay, and discretely sampled signals:

$$x(k) = s\left(k + \frac{1}{2}\tau(k)\right) = a\left(k + \frac{1}{2}\tau(k)\right) \exp\left[i\left(\varphi\left(k + \frac{1}{2}\tau(k)\right) + \omega_c k + \frac{1}{2}\omega_c \tau(k)\right)\right] \quad (3.20)$$

$$y(k) = s\left(k - \frac{1}{2}\tau(k)\right) = a\left(k - \frac{1}{2}\tau(k)\right) \exp\left[i\left(\varphi\left(k - \frac{1}{2}\tau(k)\right) + \omega_c k - \frac{1}{2}\omega_c \tau(k)\right)\right] \quad (3.21)$$

The signals x and y represent respectively the signals located on a trough and on a peak of the manipulation pressure.

3.3.2 Estimation of the phase difference ψ

Cross-multiplication of the signals yields the phase difference:

$$\psi(k) = \arg\left(x(k) \cdot \bar{y}(k)\right) \quad (3.22)$$

$$= \varphi\left(k + \frac{1}{2}\tau(k)\right) - \varphi\left(k - \frac{1}{2}\tau(k)\right) + \omega_c \tau(k) \quad (3.23)$$

The definition of the derivative as

$$\lim_{\Delta x \to 0} \frac{f(x + \frac{\Delta x}{2}) - f(x - \frac{\Delta x}{2})}{\Delta x} = f'(x) \quad (3.24)$$

yields the following result for a sufficiently small delay τ:

$$\psi(k) \approx \underbrace{\left[\dot{\varphi}(k) + \omega_c\right]}_{\theta(k)} \tau(k) \quad (3.25)$$

The approximation of small delays is generally true with SURF imaging where delays are under 20 ns.

3.3.3 Estimation of the instantaneous frequency θ

Consider the general complex form of a signal $s(t) = a(t) \exp\left[i\phi(t)\right]$. Using the same definition of the derivative as in (3.24), and considering a sufficiently short time sampling, we can approximate the instantaneous frequency by:

$$\phi(k+1) - \phi(k-1) \approx 2\dot{\phi}(k) = 2\theta(k) \quad (3.26)$$

Therefore,

$$\theta(k) \approx \frac{1}{2}\left[\phi(k+1) - \phi(k-1)\right] \quad (3.27)$$

$$= \arg\left[s(k+1) \cdot \bar{s}(k-1)\right] \quad (3.28)$$

Using (3.27), we get:

$$\theta\left(k + \frac{1}{2}\tau(k)\right) \approx \frac{1}{2}\arg\left[x(k+1) \cdot \bar{x}(k-1)\right] \quad (3.29)$$

$$\theta\left(k - \frac{1}{2}\tau(k)\right) \approx \frac{1}{2}\arg\left[y(k+1) \cdot \bar{y}(k-1)\right] \quad (3.30)$$

Finally, we can approximate the instantaneous frequency by a local linear regression:

$$\theta(k) \approx \frac{1}{2}\left[\theta\left(k+\frac{1}{2}\tau(k)\right)+\theta\left(k-\frac{1}{2}\tau(k)\right)\right] \tag{3.31}$$

$$\approx \frac{1}{4}\Big[\arg\left[x(k+1)\cdot\bar{x}(k-1)\right]+\arg\left[y(k+1)\cdot\bar{y}(k-1)\right]\Big] \tag{3.32}$$

3.3.4 Weighted Least-Square estimator

Up to here, we have found that for a sufficiently small delay τ and for a sufficiently high sampling frequency compared to the signal variations: phase difference $\psi(t)$ and delay $\tau(t)$ are linearly related through the instantaneous frequency $\theta(t)$:

$$\psi(k) \approx \theta(k)\tau(k), \tag{3.33}$$

where we can easily compute the the phase difference and the instantaneous frequency from the received signals using:

$$\psi(k) \approx \arg\left[x(k)\bar{y}(k)\right], \tag{3.34}$$

$$\theta(k) \approx \frac{1}{4}\Big[\arg\left[x(k+1)\bar{x}(k-1)\right]+\arg\left[y(k+1)\bar{y}(k-1)\right]\Big]. \tag{3.35}$$

We only need to find the delay estimate $\hat{\tau}$ which minimizes

$$\min_{\hat{\tau}} \|\psi-\theta\hat{\tau}\| \tag{3.36}$$

Therefore, we can apply the system identification theory to (3.33) and easily compute a Weighted Least-Square estimation of the delays $\tau(k)$.

The delay build-up is due to the nonlinear propagation of the manipulation pulse through soft tissue, and may be expected to generate a smoothly varying delay along depth. We choose to represent our delays with a locally linear model. For each sample k,

$$\hat{\tau}\left(k+l\right) = a_k + b_k\cdot l \qquad \text{where} \qquad l\in[0,1]\,, \tag{3.37}$$

we will minimize the WLS criterion

$$J\left([a_k,b_k]\right) = \sum_l \left|\psi(l)-\theta(l)\left(a_k+b_k l\right)\right|^2 c\left(k+l\right) w(l), \tag{3.38}$$

where c is a weight function, and w is a window function (typically chosen around 1 mm length, in order to have a delay varying slowly over the window size). In vector notation:

$$J\left(\underline{\alpha}\right) = \left(\underline{\psi}-\underline{\theta}.\left[\underline{l}\underline{1}\right]\underline{\alpha}\right)^T D\left(\underline{\psi}-\underline{\theta}.\left[\underline{l}\underline{1}\right]\underline{\alpha}\right) \tag{3.39}$$

$$= \underline{\psi}^T D\underline{\psi} - 2\underline{\alpha}^T\underline{\underline{\Theta}}^T D\underline{\psi} + \underline{\alpha}^T\underline{\underline{\Theta}}^T D\underline{\underline{\Theta}}\underline{\alpha} \tag{3.40}$$

where $\underline{l}=[-L,...,L]^T$, $\underline{1}=[1,...,1]^T$, $D=\mathrm{diag}\left(c\cdot w\right)$, $\underline{\alpha}=[ab]^T$, $\underline{\Theta}=[\underline{l}.\underline{\theta}\quad\underline{\theta}]$, and '.' is element by element multiplication. $J\left(\underline{\alpha}\right)$ is minimized when $\underline{\hat{\alpha}}$ solves

$$\underline{\underline{\Theta}}^T D\underline{\underline{\Theta}}\underline{\hat{\alpha}} = \underline{\underline{\Theta}}^T D\underline{\psi}. \tag{3.41}$$

We have a two-by-two system for each k:

$$\underline{\underline{\Theta}}^T D\underline{\underline{\Theta}}(k) = \begin{bmatrix} S_0(k) & S_1(k) \\ S_1(k) & S_2(k) \end{bmatrix}, \tag{3.42}$$

$$\underline{\underline{\Theta}}^T D\underline{\psi} = \begin{bmatrix} T_0(k) \\ T_1(k) \end{bmatrix}, \tag{3.43}$$

where

$$S_n(k) = \sum_l c(k+l)\theta(k+l)^2 w(l) l^n \tag{3.44}$$

$$T_n(k) = \sum_l c(k+l)\theta(k+l)\psi(k+l) w(l) l^n \tag{3.45}$$

Then

$$a_k = \frac{S_0(k)T_1(k) - S_1(k)T_0(k)}{S_0(k)S_2(k) - S_1(k)^2} \tag{3.46}$$

$$b_k = \frac{S_2(k)T_0(k) - S_1(k)T_1(k)}{S_0(k)S_2(k) - S_1(k)^2} \tag{3.47}$$

These two last computed estimates a_k and b_k represent from our model (3.37) accurate estimates for the nonlinear propagation delays as:

$$\hat{\tau}(k) = a_k \qquad\qquad \frac{\partial \hat{\tau}}{\partial k}(k) = b_k \tag{3.48}$$

Weighted least-square estimation is known for its computational efficiency using its recursive form. Along with linear interpolation, it may therefore be implemented to run in real-time on a ultrasound scanner. This algorithm has been adapted at ISB both for experimental probes and on the modified Ultrasonix scanner [26] used for the experiments conducted in this project.

In [27], SURF imaging has been used *in vivo* in pigs to display contrast agents with contrast-to-tissue ratios of micro-bubbles nonlinear scatterers ranging from 15-40 dB, with an up to 6 dB increase due to the delay compensation algorithm. For applications like contrast agent imaging, where the high intensity of the nonlinear scattering requires only a low manipulation pressure, the level of suppression obtained with delay correction is sufficient. However, for applications requiring the detection of low intensity nonlinear scatterers, where a high manipulation pressure has to be used, e.g. detection of micro-calcifications, the level of tissue suppression achieved with delay correction is not sufficient. It is therefore necessary to investigate and correct for the other sources of distortion in the signal to improve tissue linear scattering suppression.

3.4 Estimation and correction of the pulse-form distortions

If the impact of the nonlinear propagation delays may be approximated as a simple accumulative time-shift in the received signal, and corrected for, the effects of compressions/expansions of the imaging pulse have a more complicated result on the received signal. During forward propagation, the HF imaging pulse is manipulated with different gradients depending on the evolution with depth of the phase relation between the HF and LF pulses.

The result of this succession of compressions / expansions is a pulse-form distortion of the HF imaging pulse. Such a distortion may be noticed in the scattered signal, and thus also in the signal received by the scanner: e.g. if we consider the signals scattered from a homogeneous phantom containing only linear scatterers for two successive SURF pulse complexes of inverse manipulation pressure, the difference in the received delay-corrected HF-filtered signals corresponds to the pulse-form distortion (as well as some eventual SURF aberration phenomenon in a minor proportion). This distortion can also be noticed as a shift in the corresponding frequency spectra.

In order to correct for this complex pulse-form distortion, one may try to design a filter which will correct the changes in the pulse-form between the positively and negatively manipulated HF scattered signals due to linear scattering, without suppressing the information about the nonlinear scattering present in the signals. This approach as already been presented in equation (3.11) with the estimation of an inverse filter $\hat{H}_{k,i}^{-1}(\omega)$ for the distortion in each of the two received HF signals.

A best alternative to suppress linear scattering optimally will consist in the estimation of only one filter transforming the delay-corrected negatively manipulated HF signal $S_{2,i}$ into the positively manipulated signal $S_{1,i}$, by minimizing the average mean square error:

$$\left\langle \left| E(\omega) \right|^2 \right\rangle_\Gamma = \left\langle \left| S_{1,i}(\omega) - \hat{S}_{1,i}(\omega) \right|^2 \right\rangle_\Gamma \tag{3.49}$$

where

$$\hat{S}_{1,i}(\omega) = G_i(\omega) \left(S_{2,i}(\omega) + N_{2,i}(\omega) \right) \tag{3.50}$$

and $N_{2,i}(\omega)$ is white noise. The filter which minimizes (3.49) is the Wiener filter given as:

$$\hat{G}_i(\omega) = K_i(\omega) \frac{\left\langle S_{1,i}(\omega) S_{2,i}^*(\omega) \right\rangle_\Gamma}{\left\langle \left| S_{2,i}(\omega) \right|^2 \right\rangle_\Gamma} \tag{3.51}$$

where $K_i(\omega)$ is the Wiener gain

$$K_i(\omega) = \frac{1}{1 + \frac{N_s}{\left\langle |S_{2,i}(\omega)|^2 \right\rangle_\Gamma}} \tag{3.52}$$

N_s is a noise parameter such as $\frac{\left\langle |S_{2,i}(\omega)|^2 \right\rangle_\Gamma}{N_s}$ is approximately the Signal-to-Noise Ratio (SNR).

We have already mentioned for the pulse-form estimation filter to be correct, the distortion due to compression/expansion should be approximately equal on the time/depth interval T_i. A good estimation of this filter may be obtained from equations (3.49)-(3.52) by selecting an appropriate averaging domain. The average should be done on signal recordings where the pulse-form distortion is approximately equal: one may therefore choose to do averaging on a Γ as neighboring beams or successive frames.

An important remark is that using this single pulse-form correction filter, one do not estimate anymore the exact nonlinear scattered signal $\hat{X}_{n,i}(\omega)$ as in (3.11), but rather a filtered version of this signal corresponding to $(1 + K_i(\omega)) \hat{H}_{1,i}(\omega) \hat{X}_{n,i}(\omega)$.

Note that such a pulse-form correction filter has never been implemented before. It will then be a challenge for this thesis to develop and test a correction filter.

Chapter 4

Characterization of the propagation of SURF pulse complexes from real geometry transducers

4.1 Presentation of the simulations

4.1.1 Presentation of Abersim

Abersim [28] is an open-source toolkit for numerically simulating acoustic field propagation developed at ISB. The software has an interface for MATLAB [29], which allows an easy access to the processing of treated data, and graphic displays, as well as a pure C implementation for computational speed purpose. Originally developed for the study of aberrations, the version 2.0 of the program allows complex simulations of 3D ultrasonic wave propagation in nonlinear, heterogeneous and absorbing materials like soft tissue [30].

On a more physical point of view, Abersim is a program which solves numerically the wave equation (2.20)

$$\underbrace{\nabla^2\phi\left(\underline{r},t\right)-\frac{1}{c^2\left(\underline{r};p\right)}\frac{\partial^2\phi\left(\underline{r},t\right)}{\partial t^2}}_{\text{Nonlinear propagation}}-\underbrace{h_p\underset{t}{\otimes}\frac{1}{c_0^2}\frac{\partial^2\phi\left(\underline{r},t\right)}{\partial t^2}}_{\text{absorption}}$$
$$=\underbrace{\frac{\sigma_l\left(\underline{r}\right)}{c_0^2}\frac{\partial^2\phi\left(\underline{r},t\right)}{\partial t^2}+\nabla\left(\gamma\left(\underline{r}\right)\nabla\phi\left(\underline{r},t\right)\right)}_{\text{Linear scattering source terms}}-\underbrace{\frac{\sigma_n\left(p;\underline{r}\right)}{c_0^2}\frac{\partial^2\phi\left(\underline{r},t\right)}{\partial t^2}}_{\text{Nonlinear scattering source term}}$$

for a given wave field on the surface of the transducer. The wave equation has two solutions propagating in opposite directions. Abersim will choose the solution only propagating into the body, i.e. the positive z-direction, and solves it at a user-defined range of depth steps.

It has been shown in Chapter 3 that due to the low intensity of the scattered wave, nonlinear propagation effects could be neglected on the way back to the transducer. Therefore, the forward propagation simulations provided by Abersim will reflect the entire nonlinear propagation effects of the SURF pulse complexes.

Abersim is a very powerful tool when it comes to numerically simulating the propagation of an ultrasound wave field. However, such computations are highly time consuming. In [18], the study was of the SURF pulse propagation was restricted to flat annular arrays due to their rotational axis of symmetry which reduced the simulation to a 1D problem. In this study, we attached to reproduce the real probe geometries to be able simulate the full 3D propagation of SURF pulses and to compare how those simulations differ from the idealized ones previously conducted.

4.1.2 Presentation of the SURF probes

The SURF technology has been implemented at the ISB department on a modified Ultrasonix SonixRP (Ultrasonix Medical Corp., Vancouver, Canada, [26]) scanner presented on Figure 4.1(a). The Ultrasonix Sonix RP scanner is a system designed for research and provides unfiltered RF up to a 40 MHz framerate. The scanner was extended in order to drive the SURF dual-frequency probes: a 128 channel LF pulser was built and attached to the scanner, along with a new probe-connector board in order to support the extra number of channels.

The probes used, named *Viglen* and *Okla*, are respectively presented on Figures 4.1(c) - 4.1(d). They are both based on dual-frequency linear arrays designed at ISB and manufactured by Vermon (Tours, France, [31]). As depicted on Figure 4.1(b), the LF and HF piezoelectric elements are organized in a stack, i.e. the LF elements are located behind the HF elements. The aperture required for an adequate focusing of an ultrasound beam is in a general case wider for the LF than for the HF. Therefore, the SURF probes possess either bigger LF elements in the elevation direction (this is the case for Okla), either are divided in 3 elevation rows, where the center row is constituted of both LF and HF element layers, while the outer rows only contain LF elements. The outer LF rows are connected in parallel due to their symmetry (they transmit with the same focusing delays). On the center row, each LF element covers 4 HF elements in the azimuth direction except for the two outer ones. The probes exact dimensions may be found in Table 4.1, and a more in depth description of the design of SURF probes is given in [11] and [32].

Table 4.1: SURF probes characteristics

	Viglen		Okla	
	LF	HF	LF	HF
# Elements Azimuth	192	52	192	52
# Elements Elevation	1	3	1	1
Elements Size Elevation	7 mm	7 mm	3.3 mm	9.9 mm
Pitch Azimuth	237 μm	948 μm	190 μm	720 μm
Radius of Curvature Azimuth	∞		50 mm	
Lens Size Elevation	3.5 mm		3.3 mm	
Lens Focus Elevation	40 mm		20 mm	

Viglen has been originally designed for transabdominal early fetal imaging, and its center frequencies were set to 0.9 / 7 MHz for the LF and HF respectively, with an HF elevation focus chosen at 40 mm. Okla is a curved linear array integrated into a prostatic probe, with frequency bands physically centered on 1.25 / 10 MHz, and a closer HF elevation focus of 20 mm. Designing a dual frequency band probe is not an easy task, and both probes have some manufacturing drawbacks: a rather poor shielding as well as the creation of intermediate frequency in the probe electronics have a destructive impact on the quality of the RF-data acquired by the scanner.

(a)

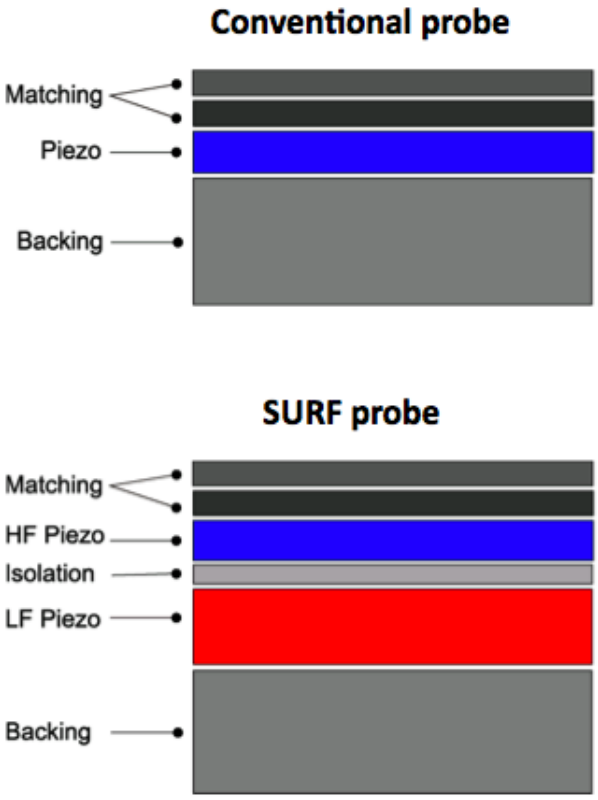

(b)

(c)

(d)

Figure 4.1: (a) Modified Ultrasonix SonixRP scanner, (b) Description of the SURF dual-frequency probes build-up (c) Picture of the Viglen dual-frequency linear probe, (d) Picture of the Okla dual-frequency prostatic probe.

However, such technical details are not the main purpose of this study, and we will concentrate on the simulation of the ideal probes. None of these two probes were originally designed for the study of breast tissues, where micro-calcifications must be detected mainly within the depth range [0 25] mm, and therefore the resolution of the imaging system will not be optimal. However such an adequate probe, named *Vora*, is currently designed at ISB and will be manufactured soon, promising better results in our case of study.

4.1.3 XdSim: a tool for the simulation of SURF pulses propagation on Abersim

XdSim is a small MATLAB software newly designed by Thor A. Tangen for making full 3D simulation of SURF pulses complexes propagation with Abersim easier. From the selection of a pre-defined dual-frequency probe model and the configuration of the transmit parameters, it generates the initial ultrasound field and the propagation parameters required to execute the Abersim simulation.

XdSim was not designed to handle curved linear arrays. Therefore, I have modified the application to take into account any azimuthal radius of curvature specified in the probe models. As we mentioned above, Abersim only handle the propagation in the direction forward to the probe elements plane. In the case of a curved linear array such as the Okla probe, where there is no plane containing the array elements, the directivity of each individual elements could not be respected. A solution to this problem was to find an equivalent aperture, called *effective aperture*, perpendicular to the probe central axis, located at the point on the surface of the probe the closest to the focus, with a width equal to the size of the real beam going through this plane. This concept of effective aperture is illustrated on Figure 4.2.

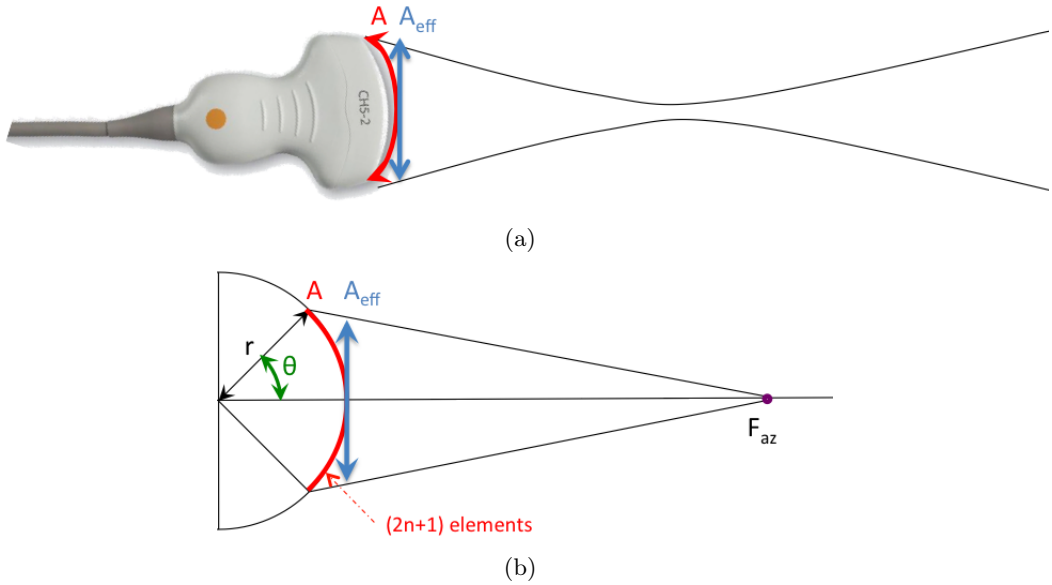

Figure 4.2: Illustration of the concept of effective aperture for a linear curved array transducer. (a) The effective aperture A_{eff} is located in the closest plane to the transducer surface being perpendicular to the central axis of the transducer, covering the entire real beam width. (b) Model used for finding an equation for A_{eff} dependent on the transducer parameters.

The effective aperture size A_{eff} can be easily computed from the transducer parameters as

$$A_{\text{eff}} = \frac{2 \cdot F_{\text{az}} \cdot r \cdot \sin(\theta)}{F_{\text{az}} + r \cdot (1 - \cos(\theta))}, \qquad \text{with} \qquad \theta = \frac{(2 \cdot n + 1) \cdot pitch_{\text{az}}}{2 \cdot r} \tag{4.1}$$

where F_{az} denotes the azimuthal focusing length, r the azimuthal radius of curvature, $(2 \cdot n + 1)$ the number of elements used for transmit, and $pitch_{\text{az}}$ the pitch in azimuth of the transmitting array.

4.2 Setup configurations used for the simulations

In [18], we explored the different SURF pulse configurations (with the possible combinations of LF / HF pulses as plane / focused beams) that may be used on a conventional ultrasound scanner. Two specific configurations appeared to be of a special interest when tested with an idealized circular symmetric transducer:

- The HF beam is focused while the LF beam is set as plane wave beam, with the initial phase-relation between the HF and LF pulses close to zero for having a perfect alignment of the two pulses at the HF focal depth. This setup has the advantage of limiting the effect of compression/expansion of the HF pulse while generating big nonlinear propagation delays which are easier to correct for, with the drawback of producing important SURF aberrations.
- both HF and beam LF beams are co-focused on the same focal point, with an initial phase-relation between the HF and LF pulses of $-T_m/4$ such as the two pulses have a perfect alignment in the selected focal depth. This setup limits the nonlinear propagation delays as well as the SURF aberration phenomenon, with the drawback of generating important compression/expansions of the HF pulse for which no real time correction algorithm has been developed yet.

For both of this settings, the study in [18] has shown that using an LF aperture bigger than the HF one (e.g. a LF relative aperture of 200% compared the the HF aperture) leaded to a better focusing pattern of the LF beam, and limited the appearance of unexpected distortions of the HF pulse during the forward propagation.

In this study, we want to characterize the full 3D propagation of SURF pulses from the real probes Viglen and Okla, using these two main beamforming configurations.

The propagation has been simulated with diffraction in muscle at 37^oC, which is a nonlinear, attenuating ($0.52\ \text{dB}\cdot\text{MHz}^{-1}\cdot\text{mm}^{-1}$), homogeneous medium. The speed of sound in this medium is approximately 1490 m/s. The simulated data was saved for post-processing at every $\Delta z = 0.5$ mm depth step with a sampling frequency $f_s = 160$ MHz.

The propagation of the SURF pulses has been simulated with Abersim and pre-configured with the transmit pulse configuration generator XdSim described above. The SURF pulse characteristics were common for the simulations with Viglen and Okla in order to be able to compare them, and are exposed in Table 4.2. The beamforming configurations selected are exposed in Table 4.3. The configuration identification codes, e.g. (F-V) or (P-O), will be used in the sequel to denote easily to the beamforming setups.

The given amplitudes of the LF and HF waves are amplitudes of the pulse on the surface of the transducer, and were selected to represent pressures values that could be used for detection of

Table 4.2: Simulated SURF pulses characteristics

		Center freq. f_c [MHz]	Bandwidth B_r [%]	Number of periods N_p	Az. Aperture D [# elem.]	Az. Aperture D [mm]	Focal length F [mm]	F-number ($F_\# = \frac{F}{D}$)
Viglen	LF	0.9	60	2.5	8	16.1	20 or ∞	1.2 or ∞
	HF	8	80	1.5	16	7.8	20	2.6
Okla	LF	0.9	60	2.5	12	15.8	20 or ∞	1.3 or ∞
	HF	10	80	1.5	20	7.6	20	2.6

Table 4.3: Description of the four beamforming configurations used for the Abersim simulations

Simulation	Probe	LF	HF	HF initial position [ns]	LF amplitude [kPa]	HF amplitude [kPa]
(F-V)	Viglen	focused	focused	-188	0.39	0.49
(F-O)	Okla	focused	focused	-114	0.35	0.42
(P-V)	Viglen	plane	focused	-37	1.17	0.51
(P-O)	Okla	plane	focused	0	0.95	0.41

micro-calcifications. Limits to the pressure amplitudes used in ultrasounds imaging are mainly delimitated by the Mechanical Index (MI)

$$\mathrm{MI} = \frac{P_{\mathrm{neg}}}{\sqrt{f}}, \tag{4.2}$$

where P_{neg} is the maximum negative pressure in MPa and f is the transmitted frequency in MHz. The mechanical indexes is an indicator of the likelihood of undesired mechanical bioeffects that could injure the patient (streaming and cavitation) and the MI values over 1.9 should not be used in vivo [33]. A quick estimation shows that the MI imposes limits on the amplitude of the LF manipulation wave since the maximum negative pressure should not be below -1.8 MPa.

- The amplitudes of the HF imaging pulse have been selected in order to reach an imaging pressure p_i of approximately 700 kPa at depth corresponding to the focus (20 mm).
- As seen in Chapter 2.4, the amplitude of the LF manipulation pulse should be as high as possible. We have chosen to simulate a rather realistic case with pressure amplitude arround 1 MPa at depth corresponding to the HF focus (20 mm).

The shape of the given pulses at depth $z = 0$ and in the focus ($z = 20$ mm) are presented for all the configurations in the azimuth and elevation planes on Figures 4.3, 4.4, 4.5 and 4.6.

The post-processing of the simulated data was done using MATLAB. In the sequel, the LF manipulation and HF imaging parts of the signals have been extracted using FIR bandpass filters of 160 taps covering the respective frequency bands [0.1 2] MHz and [4 50] MHz.

4.3 Results

4.3.1 Results in focus

An example shape of a SURF pulse complex in focus is given in Figure 4.7 for the setup (C-V). The power spectrum of the pulse confirms that even with the higher harmonics due to nonlinear propagation, there is a clear separation between the imaging and manipulation pulses. This

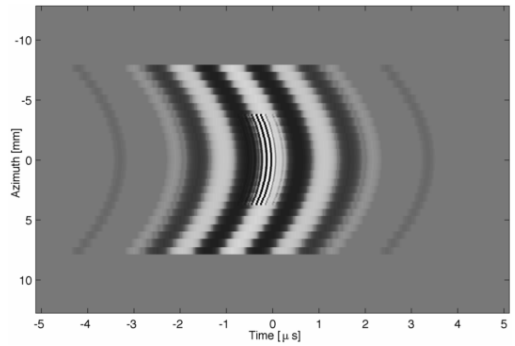

(a) (F-V)

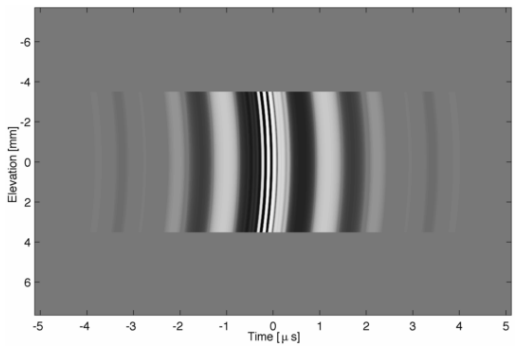

(b) (F-V)

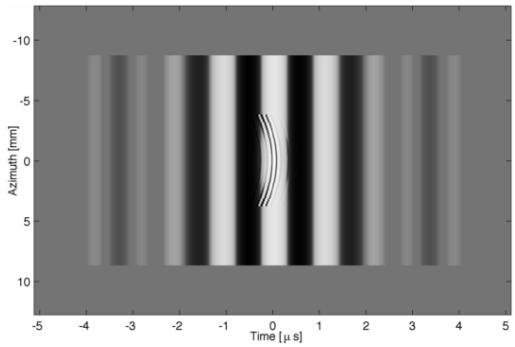

(c) (P-V)

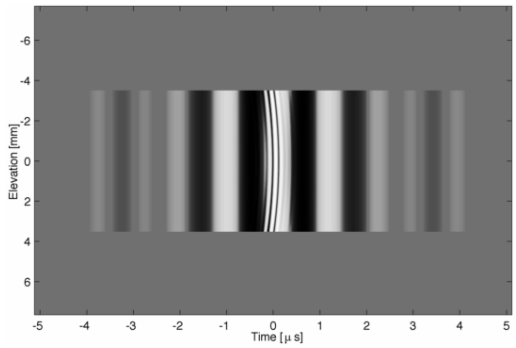

(d) (P-V)

Figure 4.3: Simulated SURF pulses on Viglen transducer surface (depth $z = 0$) in the azimuth and elevation planes for the different settings.

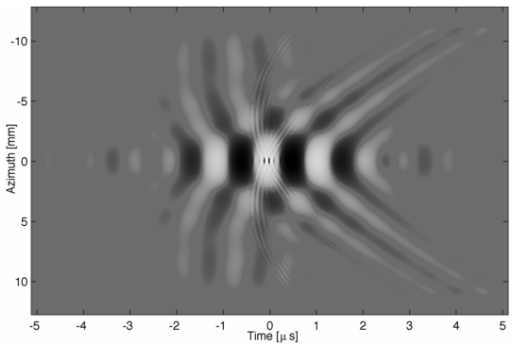

(a) (F-V)

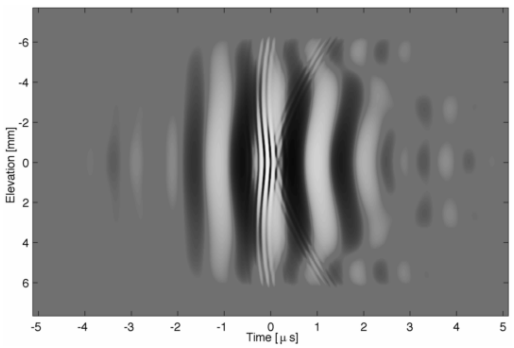

(b) (F-V)

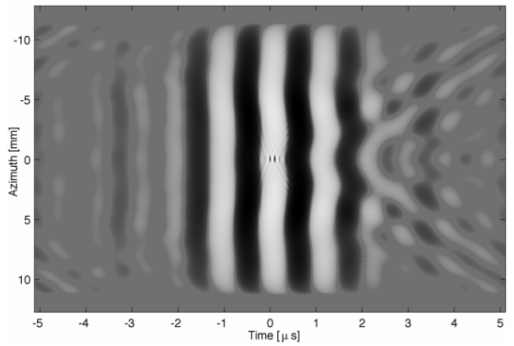

(c) (P-V)

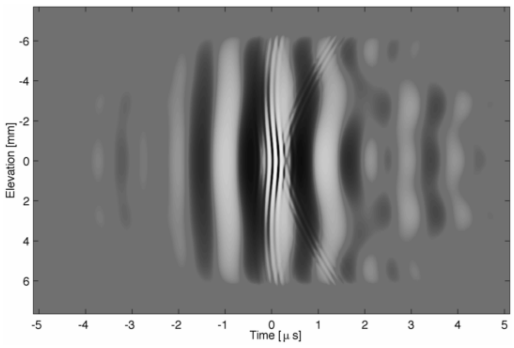

(d) (P-V)

Figure 4.4: Simulated SURF pulses on Viglen HF focus (depth $z = 20$mm) in the azimuth and elevation planes for the different settings.

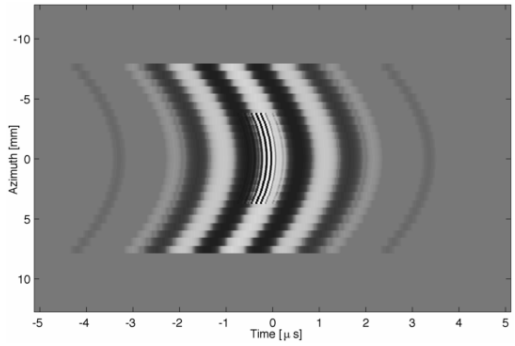

(a) (F-O)

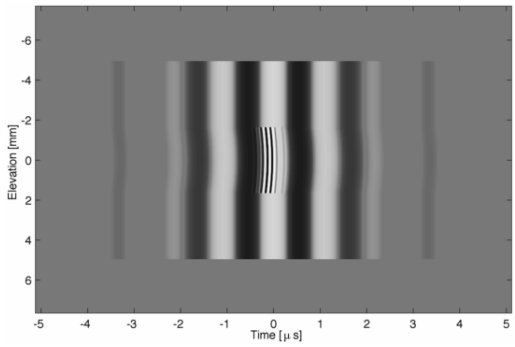

(b) (F-O)

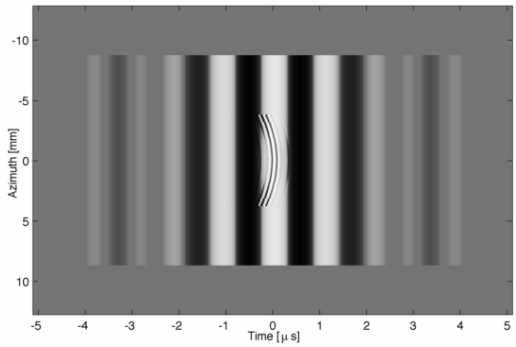

(c) (P-O)

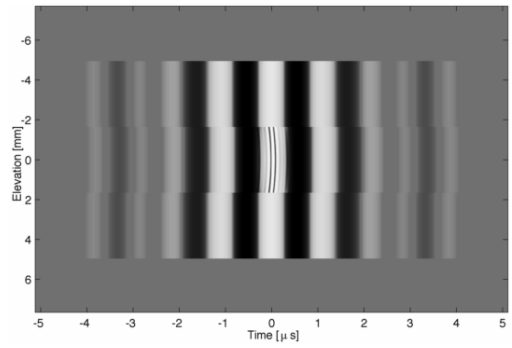

(d) (P-O)

Figure 4.5: Simulated SURF pulses on Okla transducer surface (depth $z = 0$) in the azimuth and elevation planes for the different settings.

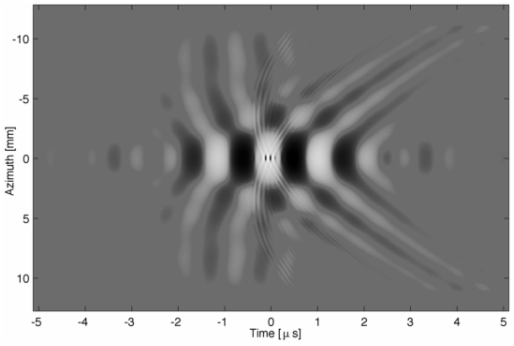

(a) (F-O)

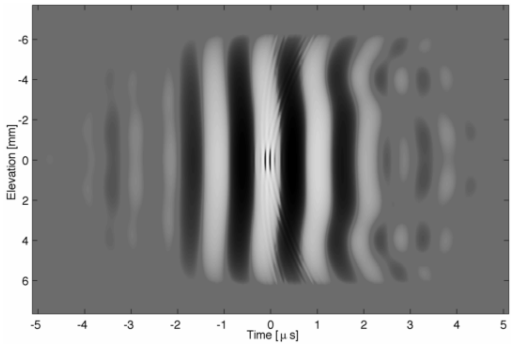

(b) (F-O)

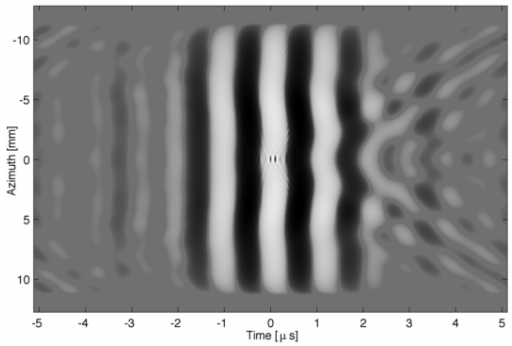

(c) (P-O)

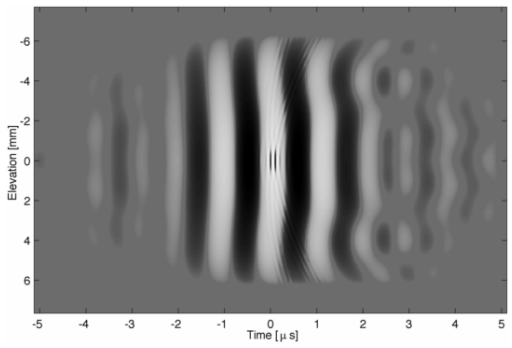

(d) (P-O)

Figure 4.6: Simulated SURF pulses on Okla HF focus (depth $z = 20$mm) in the azimuth and elevation planes for the different settings.

separation is even clearer with the Okla probe where the frequency separation between the LF and HF is 2 MHz bigger.

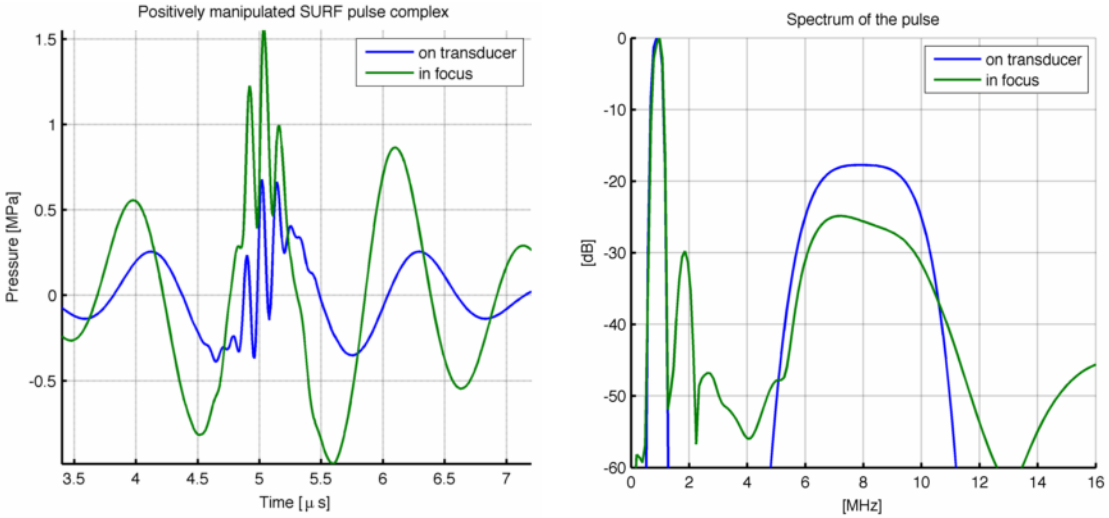

(a) (b)

Figure 4.7: Example of an unfiltered positively manipulated SURF pulse complex and its power spectrum in the center of the transducer surface and in focus for simulation setup (C-V). The spectra were normalized independently of each other.

The distortions of the imaging pulse may be observed by looking at the filtered HF pulse characteristics, as presented on Figures 4.8 and 4.9 for the different configurations. We clearly observe distortion of the pulse shape due to compression/expansion, while delays can hardly be seen by the eye on this graph (a few nanoseconds). The compression/expansion effect is characterized by net shifts in the spectra. The pulses propagating on a peak of the manipulation pressure has its spectrum shifted up in frequencies with an increase in bandwidth, while the pulse propagating on a trough has its spectrum shifted down with a decrease in bandwidth. Change in the shape of the spectra are also due to SURF aberrations and attenuation of the higher frequencies. This explains that the intensity of the HF pulses is lower when manipulated by a plane LF wave.

4.3.2 Result on the central axis of the transducer

The phase relation was defined in Chapter 3 as the distance between the HF and LF pulses. It was computed by localizing at each depth the maximum of the imaging pulse and measuring the distance to the closest manipulation peak/trough. The evolution with depth of the phase relation was told to characterize all the distortions applied to the HF pulse. The profile of the phase relation on the central axis of the transducer for the different setups is presented in Figure 4.10. After a depth > 27 mm, the focus is far beyond and the central axis of the transducer is the location of edges waves driving apart from each other. The HF imaging pulse maximum is therefore difficult to locate because the pulse literally splits in two parts, and so does the manipulation pulse when focused. Therefore, *the values of the profiles presented in this section relying on the phase relation (e.g. the experienced pressure) are not accurate for depths* > 27 *mm.*

The experienced pressure p_e is the pressure induced by the manipulation pulse on the imaging pulse, and is computed as the pressure p_m of the filtered LF manipulation pulse at the position

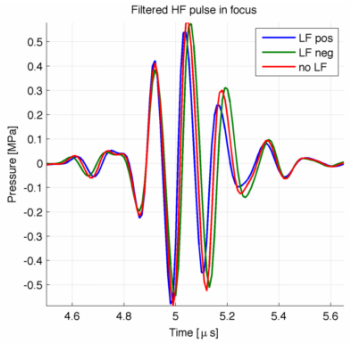

(a) (F-V)

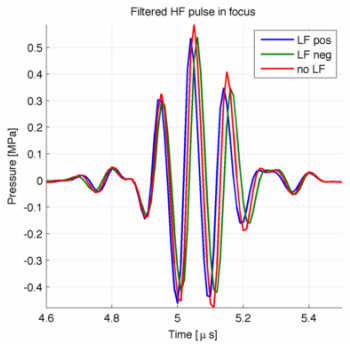

(b) (F-O)

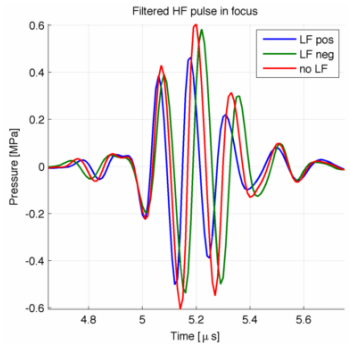

(c) (P-V)

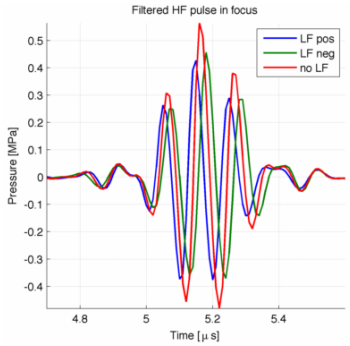

(d) (P-O)

Figure 4.8: Filtered HF imaging pulses in focus (depth $z = 20$ mm) for the different manipulations pressures, for each configuration setup.

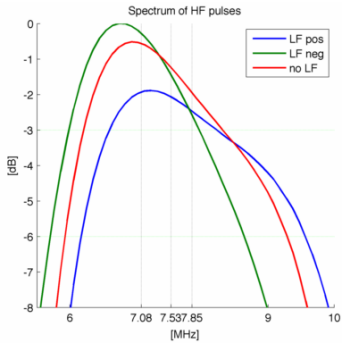

(a) (F-V)

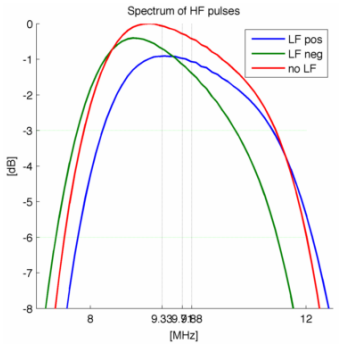

(b) (F-O)

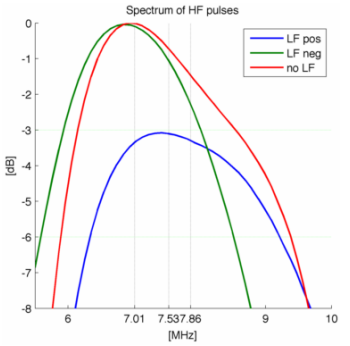

(c) (P-V)

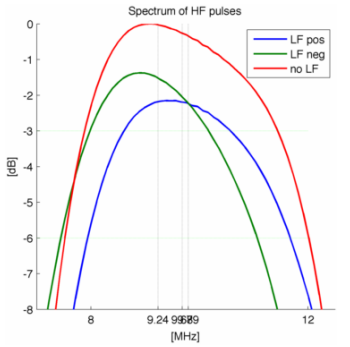

(d) (P-O)

Figure 4.9: Filtered HF imaging pulses spectra in focus (depth $z = 20$ mm) for the different manipulations pressures, for each configuration setup.

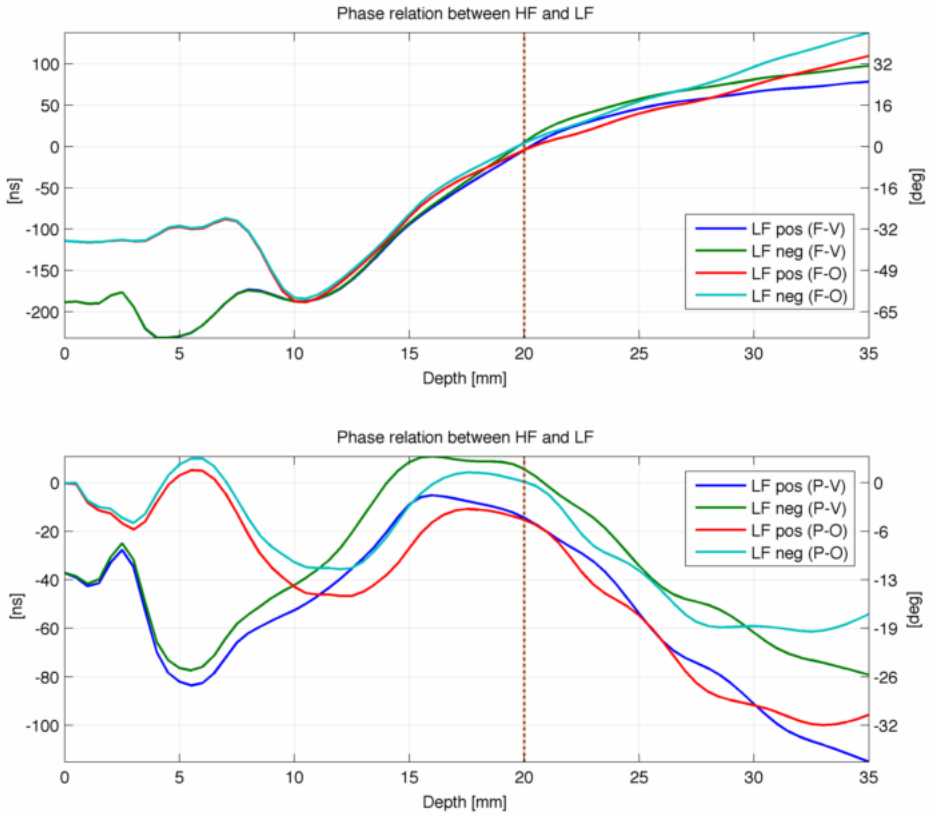

Figure 4.10: Profiles of the phase relation between the HF and LF pulse along the transducer axis for the different configurations (upper panel: focused LF beams, lower panel: plane LF beams). The left scale is expressed in nanoseconds while the right scale is in degree of the LF pulse phase.

of the maximum of the envelope of the HF imaging pulse. The maximal experienced pressure difference ΔLF is an approximative indicator of the compression / expansion. It is computed by taking the maximal difference of the manipulation pressures between the indexes corresponding to the -6dB extrema of the imaging pulse. The experienced pressures and the maximal experienced pressure differences are presented along with the manipulation pressure in Figure 4.11 for the different configurations on the central axis of the transducer.

The filtered HF imaging pressure profiles along the central axis for the different configurations are given in Figure 4.12. They were computed by taking at each depth the maximum of the envelope of the filtered HF pulse. With the plane LF configurations, we observe a large attenuation of the HF pulses, while the focused LF configurations induce a much smaller attenuation of the imaging pressure.

Delay between the pulses at a certain depth may be computed by simply maximizing the Normalized Correlation (NC) between the two signals x and y:

$$R[m] = \frac{\sum_{k=0}^{N} (x[k]y[k-m])}{\sqrt{\sum_{k=0}^{N} |x[k]|^2 \sum_{k=0}^{N} |y[k-m]|^2}}. \tag{4.3}$$

Normalized correlation has values ranging between 0 and 1, where 0 means no correlation and 1 is a perfect match. Finding the delay between the signals is equivalent to determining the

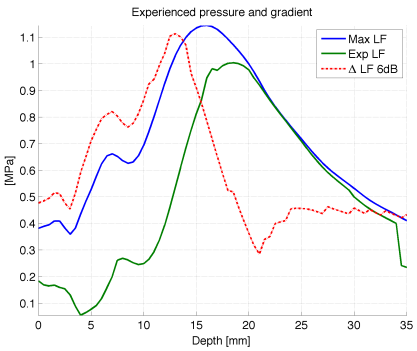

(a) (F-V)

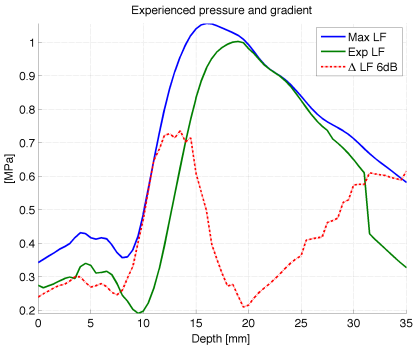

(b) (F-O)

(c) (P-V)

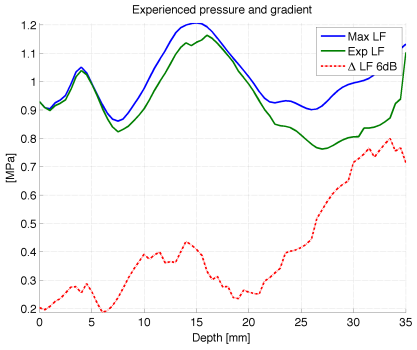

(d) (P-O)

Figure 4.11: Profiles of the manipulated pressures, experienced pressures, and maximal experienced pressure difference for the different configurations.

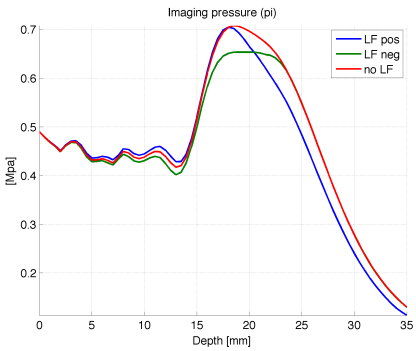

(a) (F-V)

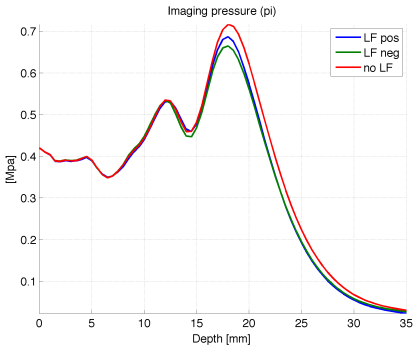

(b) (F-O)

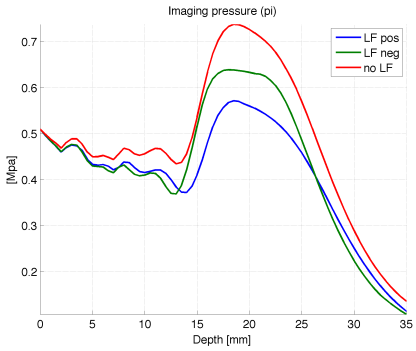

(c) (P-V)

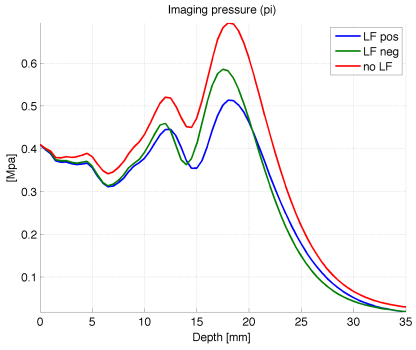

(d) (P-O)

Figure 4.12: Profiles of the filtered HF imaging pressures for the different configurations.

location where the NC function is maximal. Due to discretization, the true maximum will be located within the interval of indexes $]m_{max} - 1 \quad m_{max} + 1[$ where m_{max} is the index maximizing the NC function. A parabolic interpolation of the Normalized Correlation function is often used to get a better accuracy of the maximum, and allows an easy expression for the delay estimate:

$$\hat{\tau} = m_{max} + T_s \cdot \frac{R[m_{max} - 1] - R[m_{max} + 1]}{2\left(R[m_{max} - 1] - 2R[m_{max}] + R[m_{max} + 1]\right)} \tag{4.4}$$

where T_s is of course the sampling time period. Evolution of the delays between the two pulses along the central axis may be computed using the normalized correlation maximization (4.4) for all the depths, and Figure 4.13 presents the delays estimated between imaging pulses positively and negatively manipulated, for the different configurations. As explained above, the focusing of the imaging pulse is replaced after the focal zone on the transducer axis by the edge waves, and the doubled shape of the pulse on axis at each depth is not favorable to the estimation of a correct delay. Therefore, values for depths > 27 mm should be considered with precautions, and may be erroneous (see the discontinuities in the delay curves estimates for the plane LF beam configurations).

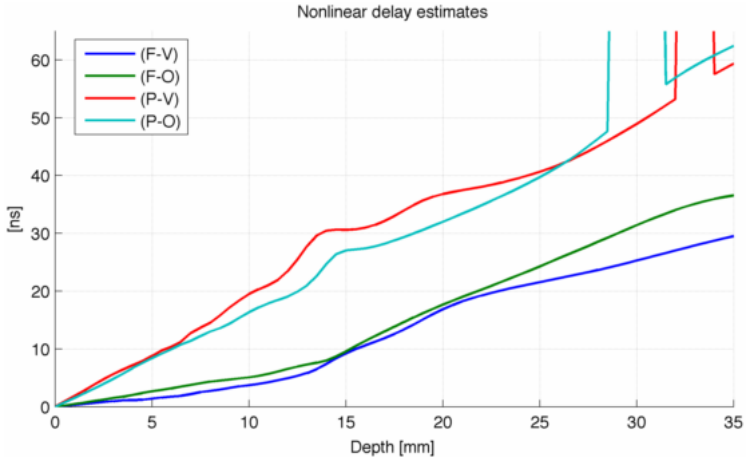

Figure 4.13: Profiles of the nonlinear propagation delay estimates along the transducer axis for the different configurations.

The phenomenon of compression / expansion was characterized as creating a net shift in the HF pulse spectrum. The buildup of such distortions may be observed by estimating the the center frequency and bandwidth of the filtered HF pulse at each depth, as presented in Figures 4.14 and 4.15. The spectra appears to present non negligible variations even in the absence of absorptions due to the propagation in water. The total difference in the center frequency is over 0.8 MHz between positively and negatively manipulated pulses.

4.3.3 Results in the azimuth and elevation planes of the transducer

The transducers used in this study have a rectangular geometry, presenting two planes of symmetry of special interest: the so called azimuth (for elevation coordinate $y = 0$) and elevation (for azimuth coordinate $x = 0$) planes.

Presenting the profiles of the different indicators in the azimuth and elevation planes represent an important number of graphs. In order not to be submerged by a new succession of figures,

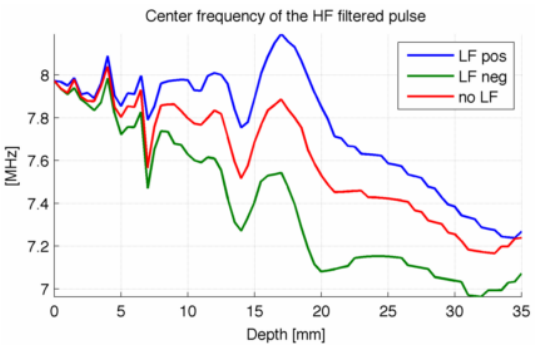

(a) (F-V)

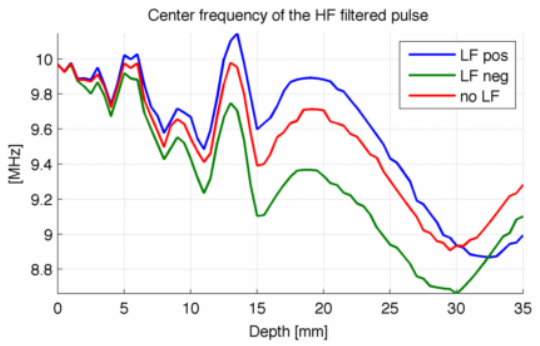

(b) (F-O)

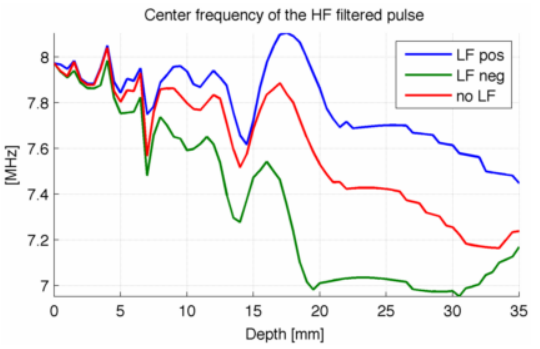

(c) (P-V)

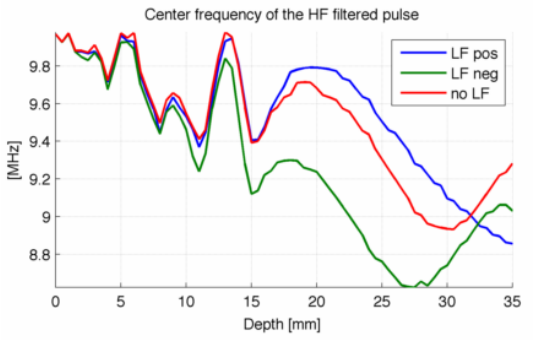

(d) (P-O)

Figure 4.14: Profiles of the center frequency estimates of the HF imaging pulse along the transducer axis for the different configurations.

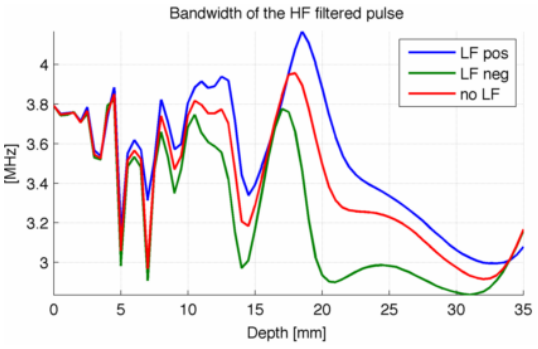

(a) (F-V)

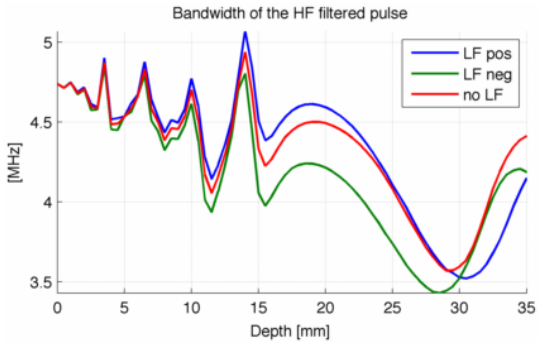

(b) (F-O)

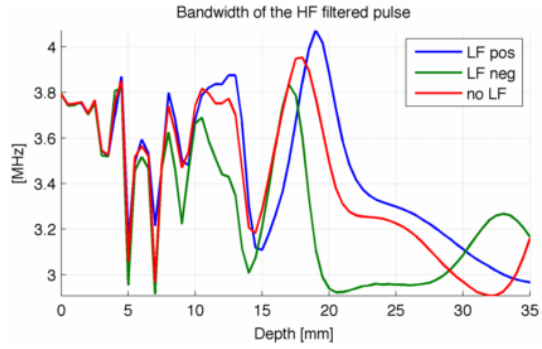

(c) (P-V)

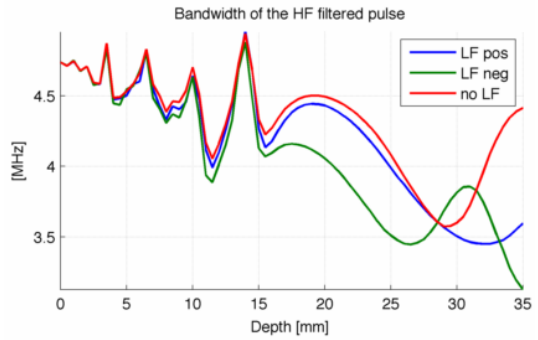

(d) (P-O)

Figure 4.15: Profiles of the bandwidth estimates of the HF imaging pulse along the transducer axis for the different configurations.

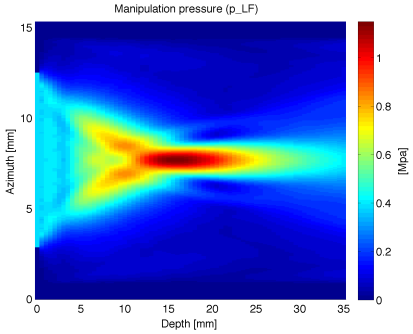

(a) (F-V)

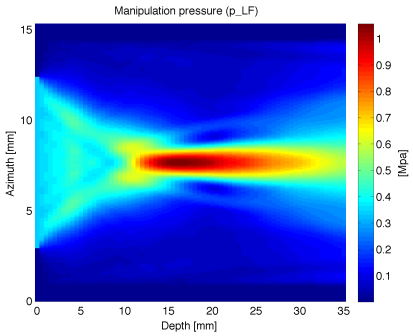

(b) (F-O)

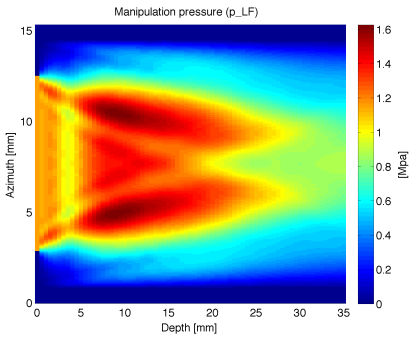

(c) (P-V)

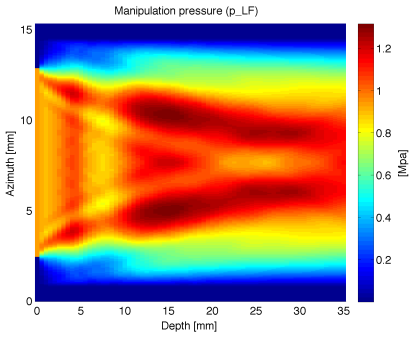

(d) (P-O)

Figure 4.16: Profiles of the LF manipulation pressure in the azimuth plane for the different configurations.

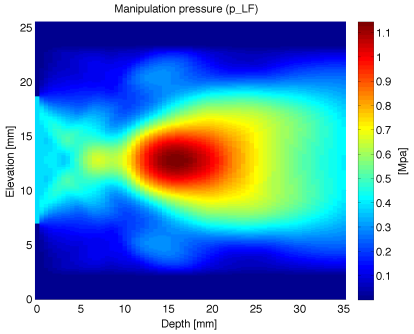

(a) (F-V)

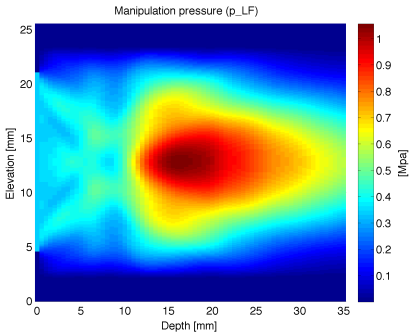

(b) (F-O)

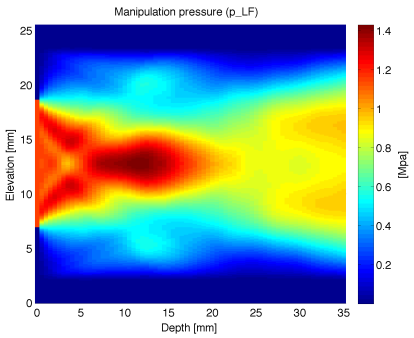

(c) (P-V)

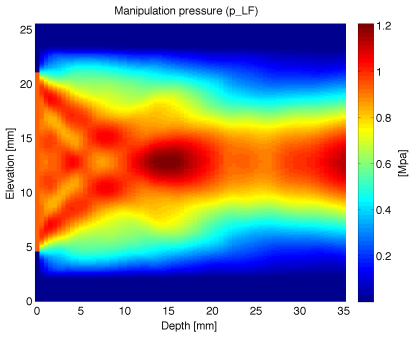

(d) (P-O)

Figure 4.17: Profiles of the LF manipulation pressure in the elevation plane for the different configurations.

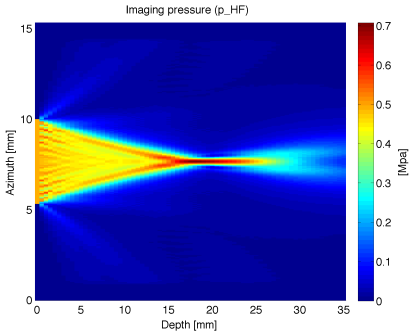

(a) (F-V)

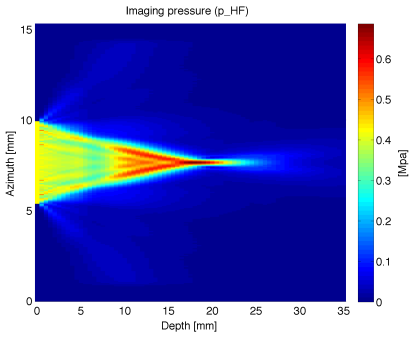

(b) (F-O)

Figure 4.18: Profiles of the HF imaging pressure in the azimuth plane for the focused configurations.

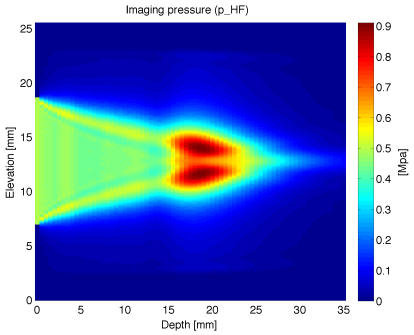

(a) (F-V)

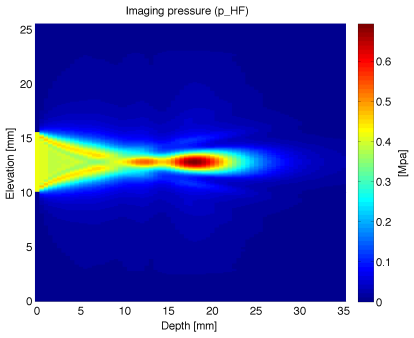

(b) (F-O)

Figure 4.19: Profiles of the HF imaging pressure in the elevation plane for the focused configurations.

only some interesting figures will be presented and discussed here, while the attentive reader may refer to the Appendix A for an extensive presentation of the propagation in the azimuth and elevation plane.

The computation of the beam profiles in the azimuth and elevation planes allows the understanding of the diffraction pattern induced by the transducer geometries and setup configurations. Such beam profiles have been computed by considering the maximum of the filtered pulses envelopes at each position, and are presented in Figures 4.16, 4.17, 4.18 and 4.19, with further reference to Appendix A for the profiles not displayed. At first sight, a difference in the diffraction patterns of the Viglen and Okla probes exists for the LF beams, while the HF beams mainly differ only in the elevation plane where two foci are present for the Viglen probe. Moreover, the true focal zones are located before the pre-configured focal depth of 20 mm.

The SURF aberration phenomenon appears when the change in sound speed of the HF imaging pulse due to the LF manipulation pressure has an impact on the focusing delays of the HF pulse. The focusing delays may be determined using the normalized correlation technique described above, by looking at the delay difference between the HF pulse at a specific location and on the transducer central axis at the same depth. In the presence of SURF aberrations, the focusing of the HF pulse will be altered by the manipulation pressure. Hence, in the presence of SURF aberrations there will be a non negligible difference in the focusing delays between the positively and negatively manipulated HF pulses. This indicator has been estimated only within the -6dB boundaries of the HF beam profiles, where the SURF pulse complex is present in a significant manner, and is displayed in Figures 4.20 and 4.21 for the different configurations in the azimuth

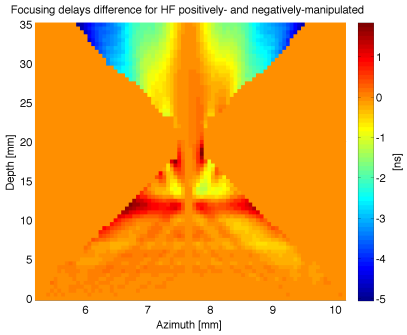

(a) (F-V)

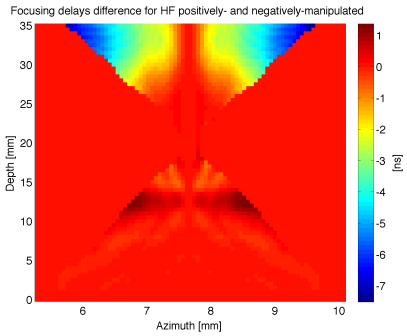

(b) (F-O)

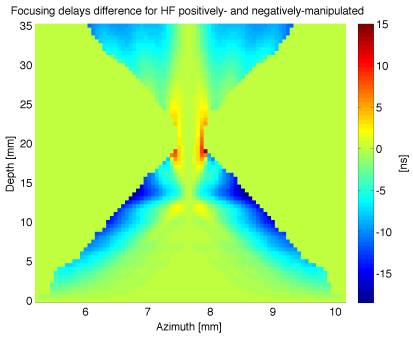

(c) (P-V)

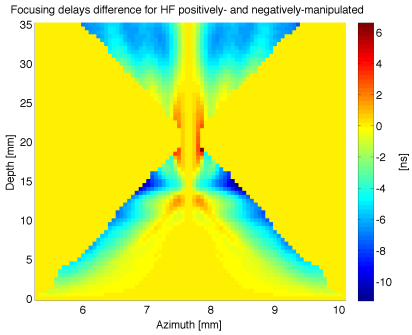

(d) (P-O)

Figure 4.20: Profiles of the focusing delays difference between positively and negatively manipulated HF pulses, used to quantify SURF aberrations, in the azimuth plane for the different configurations.

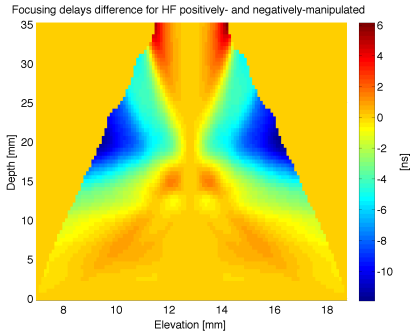

(a) (F-V)

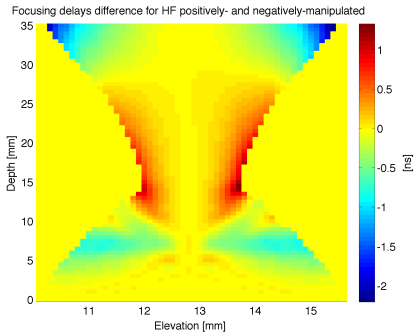

(b) (F-O)

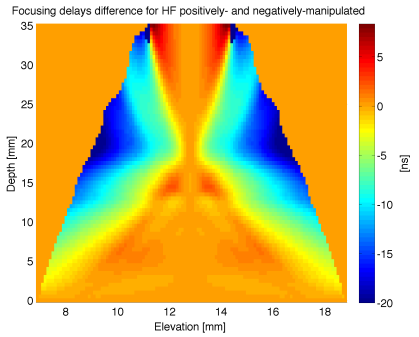

(c) (P-V)

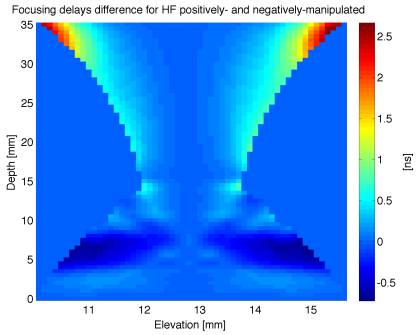

(d) (P-O)

Figure 4.21: Profiles of the focusing delays difference between positively and negatively manipulated HF pulses, used to quantify SURF aberrations, in the elevation plane for the different configurations.

and elevation planes. We may observe the presence of higher differences in the focusing delays between the transducer surface and the focal depth in the azimuth plane for the simulations with plane wave LF beams.

Profiles in the azimuth and elevation plane of the phase relation, of the experienced pressure, and of the maximum difference in experienced pressure within the HF pulse have all been computed within the -6dB boundaries of the HF beam, and are presented in Appendix A.

4.3.4 Performances in the imaging of nonlinear scatterers

The efficient detection of nonlinear scatterers is conditioned by the suppression of the differences in the positively and negatively manipulated imaging pulses. This difference is created by the nonlinear propagation effects and may be measured at each depth from the delay-corrected HF-filtered signals by two indicators:

- The Relative Amplitude Difference (RAD) measures the difference in the amplitude of the positively and negatively manipulated pulses, either by considering the ratio between the maxima of the HF pulse envelopes across the pulse, either by computing the ratio of the root mean square (RMS) values the envelopes of the pulses:

$$RAD_{max} = \frac{\max_t \left(\left| \widetilde{p^{\oplus}_{HF}}(t) \right| \right)}{\max_t \left(\left| \widetilde{p^{\ominus}_{HF}}(t) \right| \right)} \quad , \quad RAD_{rms} = \frac{\mathrm{rms}_t \left(\left| \widetilde{p^{\oplus}_{HF}}(t) \right| \right)}{\mathrm{rms}_t \left(\left| \widetilde{p^{\ominus}_{HF}}(t) \right| \right)} \tag{4.5}$$

- The Relative Tissue Suppression (RTS) measures the level of suppression one may expect from the probe without correcting for the distortions of the imaging pulse. It is computed as the ratio between the difference of the two pulses and the positively manipulated pulse, and may be expressed as above with maximal and RMS values:

$$RTS_{max} = \frac{\max_t \left(\left| \widetilde{\{p^{\oplus}_{HF} - p^{\ominus}_{HF}\}}(t) \right| \right)}{\max_t \left(\left| \widetilde{p^{\oplus}_{HF}}(t) \right| \right)} \quad , \quad RTS_{rms} = \frac{\mathrm{rms}_t \left(\left| \widetilde{\{p^{\oplus}_{HF} - p^{\ominus}_{HF}\}}(t) \right| \right)}{\mathrm{rms}_t \left(\left| \widetilde{p^{\oplus}_{HF}}(t) \right| \right)} \tag{4.6}$$

The RAD and RTS are respectively presented for the different configurations in Figures 4.22 and 4.23.

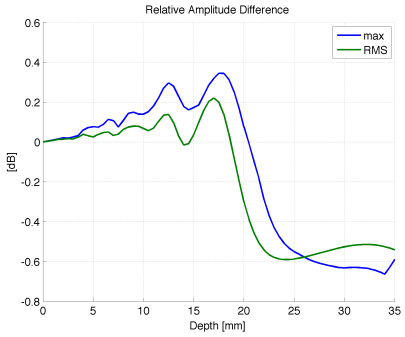

(a) (F-V)

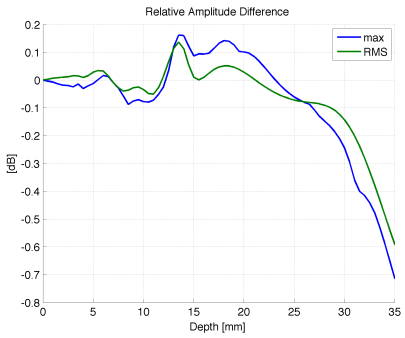

(b) (F-O)

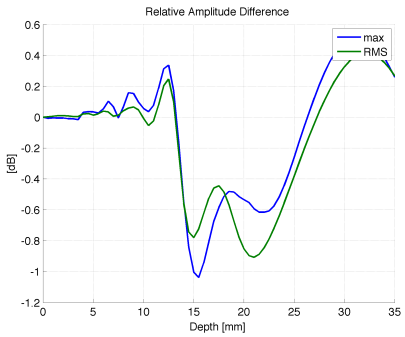

(c) (P-V)

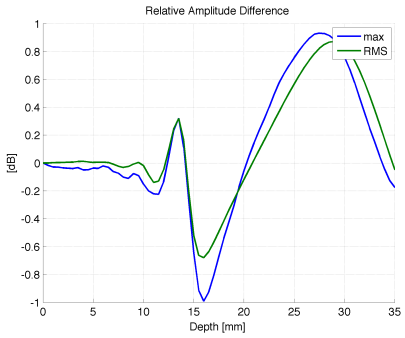

(d) (P-O)

Figure 4.22: Relative Amplitude Difference (RAD) simulated profiles along the transducer central axis for the different configurations.

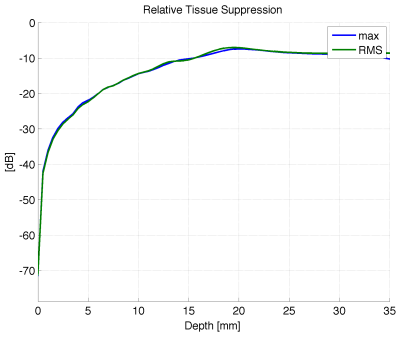

(a) (F-V)

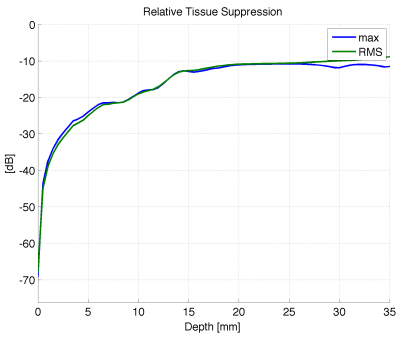

(b) (F-O)

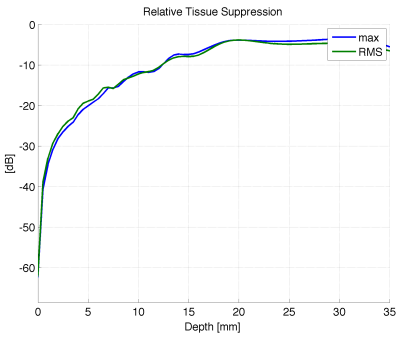

(c) (P-V)

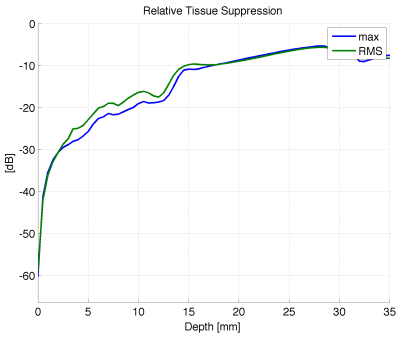

(d) (P-O)

Figure 4.23: Relative Tissue Suppression (RTS) simulated profiles along the transducer central axis for the different configurations.

4.4 Discussion

4.4.1 On the results in focus

The SURF pulse complex in focus

The nonlinear forward propagation of the SURF pulses possess some general characteristics (exposed in Figure 4.7). The pulse complexes on the transducer surface start as the superposition of an HF pulse located on a slope of the LF pulse, and evolve up to the HF focal depth where the superposition consist in a perfect alignment of the HF imaging pulse on a peak/trough of the LF manipulation pressure. During all the propagation, the power spectra of the HF and LF pulses present a net frequency separation. This spectral separation is important: if the nonlinear propagation of the manipulation pulse causes the formation of LF higher harmonics that contribute to the frequency band of the HF imaging pulse with a noticeable intensity, then they will be kept in the received HF-filtered spectrum as distortions, having a direct impact on the imaging system. Moreover, we denote that quite dramatic changes have happened to the HF imaging frequency pulse spectrum compared to the LF spectrum. This is due to both the frequency dependent attenuation during the propagation in the muscle tissue, which has a bigger impact on the imaging pulse, and the distortions due to SURF aberrations and the compression/expansion experienced by the HF pulse during the nonlinear propagation.

HF imaging pulses in focus

As mentioned above, the impact on imaging of the SURF pulse complex forward propagation are limited to the changes happening to the HF imaging frequency band. Therefore, the study of the consequences in focus of nonlinear forward propagation may be restricted in our case to the study of the imaging pulse shape and spectrum as presented in Figures 4.8 and 4.9.

- For all the configurations presented, the filtered HF pulse spectra present some similarities. The positively manipulated pulses possess a spectrum with a higher center frequency than the non-manipulated pulse, while the negatively manipulated pulses have a spectrum that is down-shifted in frequencies. This means that the overall result of compressions/expansions of the imaging pulses during the forward propagation results mainly in a compression of the HF pulse for the case of a positive LF pulse and an expansion of the HF pulse for a negative LF pulse.
- When considering the intensity of the pulses spectra, we notice that the positively manipulated HF pulse present more distortions compared to a similar non manipulated pulse than the negatively manipulated pulse. This means that the HF pulses traveling close to a peak of the manipulated pressure present more distortions when arriving in the HF focus. Such phenomenon is the result of the frequency dependent attenuation, and was not observed when simulations were conducted in water, like in [18, p. 36].
- If we now consider the situations with plane a LF beam (P-V) and (P-O), we denote that the frequency spectra of the manipulated pulses have an intensity of 1 dB lower in average compared to the frequency spectra of the manipulated pulses in the corresponding configurations (F-V) and (F-O) where the LF beam is focused. This lower intensity may also be noticed in the imaging pulses shapes in Figures 4.8(c) and 4.8(d), where the non-manipulated pulse is predominant. This phenomenon is due, as we shall see later, to the fact that SURF aberrations are more intense in the configurations with a plane LF beam,

and produce a de-focusing of the HF imaging beam, lowering the intensity of the observed signal in focus.

- It is also of interest to notice that the simulated HF filtered imaging pulses present some similarities intrinsic to the probes, whatever the LF manipulation beam is focused or not. For the configurations with the Viglen probe (F-V) and (P-V), the positively manipulated pulse spectrum intensity is always far beneath the one of the negatively manipulated pulse (from 2 to 3 dB), while the intensity between the spectra for the positively and negatively manipulated pulses in the configurations with the Okla probe (F-O) and (P-O) only differs in less than 1 dB. One may also notice that for the Viglen simulations, the negatively manipulated pulses spectra are always closer in intensity to the non-manipulated pulse spectrum than to the positively manipulated pulse spectrum ; this phenomenon will be explained later.

4.4.2 On the results on the transducer central axis

Phase relation between the HF and LF pulses

In Chapter 3, we noticed that the buildup of distortions of the HF imaging pulse due to nonlinear forward propagation could be studied if we had the knowledge of the manipulation pressure field as well as the phase relation between the HF and LF pulses at all depths. First studies ([34], [18]) have shown that this phase relation was independent of the manipulation pressure for annular array probes. Further studies of this phase relation as done in Appendix B or in [35] have shown that, for real probes, *the phase relation between the HF and LF pulses was actually dependent of the intensity of the LF pressure field.* The configuration setups chosen here have been calibrated such as the phase relation was approximately null at the focal depth (i.e. that the HF pulse is located either on a peak, either on a trough of the LF pulse). The resulting phase relation profile may be observed in Figure 4.10.

Let's remind first that the values of the phase relation on the transducer axis for depth $z > 27$ mm are erroneous, since after the focus the imaging pulse splits in two distinct parts corresponding to the edge waves, and that many different references may be chosen to compute the corresponding phase relation.

- For the focused LF beam situations (F-V) and (F-O), the phase relation starts respectively around -188 ns and -114 ns, which is far away from the initial value of $-T_m/4 = -278$ ns obtained in the case of an ideal annular transducer in Chapter 3.2. The HF imaging pulse then oscillates for the first 10 mm on the flank of the manipulation pulse. From this depth, the phase relations starts to be reduced in a similar manner for the configurations (F-V) and (F-O), to reach a perfect alignment in the focus. We remark that the phase relation is nearly independent of the sign of the manipulating pressure before the focal depth, meaning that the positively and negatively manipulated HF pulses slide in a similar way up to the focus, experiencing close to symmetric manipulation pressures (and pressure gradients).
- For the plane LF beams situations (P-V) and (P-O), values of the phase relation from the transducer surface to the HF focal depth are smaller than for the focused LF beam configurations. Before the focal depth, the phase relation is also very similar whatever the sign of the manipulation pressure is (even though the change in the scale of the lower panel in Figure 4.10 tends to think the opposite). For these configurations, the HF imaging pulse

travel close to the peak/trough of the manipulation pressure, and will therefore create more nonlinear propagation delays and less compression/expansion than with a focused LF.

Experienced pressure and maximum difference in the experienced pressure

The experienced pressure p_e and the maximum difference in the experienced pressure ΔLF (presented in Figure 4.11) are two interesting concepts when it comes to understand how delays and compression/expansions are created during the pulse forward propagation, since they are directly computed from the combination of the two key factors describing the forward propagation distortions buildup: the LF manipulation pressure and the phase relation between the HF and the LF.

The experienced pressure p_e is actually directly related to the buildup of nonlinear propagation delays, since it represents the average amount of manipulation pressure across the HF pulse, while the maximum difference in the experienced pressure ΔLF indicates the level of variations of the manipulation pressure across the HF pulse, and therefore indicate the intensity of the compression/expansion buildup at each depth. Let's remind that these curves are not accurate for depths $z > 27$ mm, since they are computed with the help of the phase relation.

A general and useful observation is that the maximum experienced pressure is close to 90% of the maximum manipulation pressure for all the configurations, and that the maximum in the experienced pressure profile is located a few millimeters after the maximum of the manipulation pressure profile (5 mm for the focused LF situations, 1 mm for the plane LF). This lag time between the variations of the two curves is directly related on the phase relation intensity. Moreover, we see that the experienced pressure curve will tend towards the manipulation pressure curve just after the focal point.

- For the focused LF configurations (F-V) and (F-O), the experienced pressure is small (inferior to 320 kPa) until depth 10 mm where it suddenly increases as the phase relation between the LF and HF decreases, to reach a maximum experienced pressure just before the focal depth (around 19 mm, which correspond to the true focus of the HF beam). The nonlinear propagation delay observed in focus will be mainly generated in the zone from depth 15 mm to 20 mm where sufficient levels of experienced pressure are reached. The maximum difference in experienced pressure along the HF imaging pulse ΔLF presents small values compared to the manipulation pressure level when the phase relation is close to zero while presenting high values compared to the manipulation pressure when the pulse is on the flank (highest gradient) of the LF pulse. With Viglen (F-V), the HF pulse oscillates on the flank of the manipulation pulse (phase relation between $-50°$ and $-70°$ for depth < 10 mm), and the ΔLF will be intense from the transducer surface until the focus, thus creating a high level of compression/expansion. With Okla (F-O), the HF pulse stays close to the top/peak of the LF pulse (phase relation of $-50°$) until the manipulation pressure raises (for depth from 10 to 20 mm), and the effects of compression/expansion will be minimized in this situation compared to (F-V).
- For the plane LF configurations (P-V) and (P-O), we observe an experienced pressure really close to the level of the manipulation pressure, due to the fact that the imaging pulses stay always close to the peak/trough of the LF pulse. This causes the formation of nonlinear propagation delays to be maximized from the very beginning of the pulse propagation. The maximum difference in experienced pressure along the HF imaging pulse ΔLF is here also dependent on the probe used: with Viglen (P-V) the phase relation is

bigger (up to $-30°$ at depth 5 mm), causing the ΔLF to be important in the area 5-10 mm, and generating important level of compression/expansions, while this phenomenon is nearly not existent with the Okla probe (P-O), were we can considered that the creation of compression/expansion is minimized.

Filtered HF imaging pressure

The distortions in the filtered imaging pulses shapes and spectra observed previously may be better understood with the help of the profiles of the maximal imaging pressures along the central axis of the transducer presented in Figure 4.12. The profiles are presented with the non-manipulated HF pulse as a reference.

- Let's first remark by comparing Figure 4.12 with 4.11 that distortions of the manipulated HF imaging pulses profiles only appear in a non-negligible manner when either the experienced pressure, either the maximum difference in experienced pressure ΔLF is above 600kPa.
- For the focused LF configurations (F-V) and (F-O), we observe an attenuation of the negatively manipulated pulse compared to the positively manipulated one. This is mainly due to the nonlinear propagation of the pulse [5]: we have an introduction of phase variations between the fundamental frequency and its harmonics, which results in an asymmetry of the distorted wave (the peak compression exceeds the magnitude of the peak rarefaction). Put in other words, the negatively manipulated HF pulses are slightly attenuated as a part of the trough of the LF manipulation pulse.
- The profiles of the imaging pressure when the LF is a plane beam (P-V) and (P-O), present more drastic attenuations of the manipulated pulses. This difference with the focused LF beam setting is mainly due to the importances of the SURF aberrations in these situations: the difference in the diffraction pattern between the plane LF beam and the focused HF beam causes a phase relation which is not constant across the HF pulse, and the resulting focusing is weakened. Note that this phenomenon is more important for the positively manipulated HF pulses. It is therefore of interest when investigating the SURF aberration phenomenon to consider the positively manipulated pulse, since it represent the maximal variations that may happen due to such aberrations. Moreover, this remark may be used smartly to reduce the level of SURF aberrations: one may imaging a SURF imaging method where the negatively manipulated is subtracted not to a positively manipulated pulse but to a non-manipulated HF pulse... it reduces the nonlinear scattering in the received signal by a factor 2, but also reduces the effect of SURF aberrations by 2, allowing an easier use of the plane LF configurations.

Nonlinear propagation delays

Nonlinear propagation delays between the positively and negatively manipulated imaging pulses were already explained as resulting from the presence of a non negligible experienced pressure by the HF pulse. We observed the presence of such high experienced pressures after depth $z = 10$ mm for the focused LF situation, and from the surface of the transducer for the plane LF cases. The impact of this difference between the plane and focused LF configurations may be seen in Figure 4.13: delays for the setups (P-V) and (P-O) are 3 times more important than delays for (F-V) and (F-O) for depth $z \leq 10$ mm, and 2 times more important for depth $z > 10mm$.

When analyzing the build-up of the delay between the positively and negatively manipulated imaging pulses with depth, one may easily qualify the curves shape of 'piecewise linear' (term first used in [36]). Such shapes include the presence of inflections points: the first one is located at depth $z = 14$ mm and concerns both probes, while the second is located around depth $z = 20$ mm and only appears in the delay curves estimated from the Viglen simulations (F-V) and (P-V).

As opposed to the simulations conducted with annular arrays in [18, chap. 5], the nonlinear delay curves for the co-focused configurations (F-V) and (F-O) are no longer quasi-null (i.e. under 2 ns) until reaching depths close to the focal zone (for $z < 15$ mm). The special geometries of the real rectangular probes do not allow the initial phase relation to be close to a quarter of the LF period ($T_m/4$) in order to have a perfect alignment of the two pulses in focus (phase relation equals to zero at depth $z = 20$ mm), as it was permitted for an ideal annular array (as presented in Chapter 3.2). This will cause the HF pulse to propagate without starting in the middle of the LF pulse flank, and such a propagation with a non negligible experienced pressure will lead to the creation of propagation delays from the surface of the transducer (depth $z = 0$ mm).

Center frequency and bandwidth of the imaging pulse

Changes in the center frequency and bandwidth of the imaging pulse may have three main causes: the frequency dependent attenuation, the compression/expansion of the pulse, and the superposition in the signal of two pulses or more with a slight delay in time or in frequency. The profiles of the center frequency observed in Figures 4.14 and 4.15 do illustrate all these effects:

- In a general case, the non-manipulated as well as the manipulated pulses are affected by the accumulation of HF pulses on the transducer axis due to focusing. Such accumulation of signals with small delays in time or frequency causes the spectrum to oscillate in the frequency domain, and this oscillations are recognizable on all the three curves (for the non-, positively- and negatively-manipulated HF pulses). All the curves are also touched by the frequency dependent attenuation, which causes the center frequency of the pulses to decrease with increasing depth.

- For the focused LF configurations (F-V) and (F-O), the shifts in center frequency and bandwidth correspond to the compression/expansions occurring in the HF pulse from depth $z = 0$ mm. Positively manipulated pulses are compressed while negatively manipulated pulses are expanded.

- For the plane LF configurations (P-V) and (P-O), a small amount of compression/expansion exists, while the SURF aberration phenomenon creates even bigger shifts in the frequency spectra, causing bigger variations in the center frequency and bandwidth estimates.

A general remark is that the shifts in center frequency and bandwidth are more important for the Viglen probe than for the Okla probe. This is due to the better LF focusing capabilities on the Okla probe, as the later analysis will confirm.

4.4.3 On the results in the azimuth and elevation planes of the transducer

Many results have been presented both in this Chapter and in Appendix A in the azimuth and elevation planes of the transducers. Most of the propagation phenomenons have already been observed and analyzed in details when discussing about the profiles on the central axis of the transducer. It is therefore important to remember that all the results presented in the azimuth and elevation planes were introduced in order to differentiate the effects hidden from us when we only looked at the central axis profiles, if they exist. In the sequel, we will thus only comment the phenomenons that have not been explained and discussed in the previous sections.

Pressure profiles

The imaging and manipulation pressure profiles produced by Viglen and Okla in the azimuth and elevation planes are useful in understanding the exact impact of the probe geometries and specifications on the resulting SURF pulse propagation.

- When transmitting a focused LF beam, as detailed for configurations (F-V) and (F-O) in Figures 4.16 and 4.17, the manipulation pressure profiles look very similar for the two probes. In the azimuth, both probes possess approximately the same aperture and the same F-number, providing a quite similar focusing. A deeper study shows that he Fresnel parameter of the LF beam, computed in the azimuth from equation (3.7), is respectively $\{0.51,\ 0.53\}$ for the configurations (F-V) and (F-O). This means that the focusing provided in azimuth by the Viglen probe is slightly better, even though it is a generally "bad" focusing. We can notice that in practice by observing that both focusing zone are located around depth $z = 16$ mm, (and not at depth 20 mm where it should be focused) but that the focal zone is less elongated for the Viglen probe (it finishes at depth 19 mm, compared to 25 mm for the Okla probe). But this difference is only due to the number of elements chosen in azimuth to transmit the beam, and the effect may be inverted by transmitting the LF beam with one more element with Okla. In the elevation plane, however, we may notice a bigger difference. First, the elevation aperture is clearly bigger in the Okla probe: this is due to the fact that the Okla probe has LF elements covered by 3 rows of HF elements, where the central row is itself covered by a physical lens of elevation focus at depth 20 mm, while the Viglen probe is only used with one elevation row for both LF and HF elements, entirely covered by a physical lens of elevation focus at depth 40 mm. This causes the manipulation pressure profile to look less focused for the Okla probe, since the LF elements are radiating as plane wave on the elevation extremities, while radiating a focused beam on the central elevation row. The Fresnel parameter for the focused LF parts of the transducer in the elevation plane is respectively $\{21.6,\ 12.16\}$ for the Viglen and Okla probes, and the focusing effect of these transducers in elevation is therefore very poor. We actually notice wide (and poor) focal zones around depth 15 mm, far away from the focal depth of the elevation lenses.
- For the situations with a plane LF beam (P-V) and (P-O), the manipulation pressure present similar characteristics. In azimuth both the probes furnish a plane LF beam with some regular characteristics. In elevation, however, the Okla probe is still the superposition of a focused (at 20 mm) and a two plane beams, while the Viglen probe only consists of a focused (at 40 mm) beam. The observed elevation profiles are really similar to the ones observed for the focused LF, except that the pressure level is in average 400 kPa higher with Viglen.

- The study of the azimuth and elevation profiles for the focused HF beams is probably more instructive. First, we may notice that the profiles are approximately similar whatever the type (plane/focusd) of LF beam used, and therefore only the configurations (F-V) and (F-O) have been presented in Figures 4.18 and 4.19 to distinguish between the HF pressure field created with the Viglen and the Okla probes. The Fresnel parameter for the Viglen and Okla probes are respectively $\{0.25,\ 0.21\}$ in azimuth and $\{2.43,\ 1.37\}$ in elevation. This means that we may expect a good and sharp focusing in the azimuth plane, while having a poor focusing situation in the elevation planes. The focusing capabilities of Okla probe is exactly described by the precedent conclusion. However, the superposition for the Viglen probe of a HF beam electronically focused at depth 20 mm in azimuth and physically focused by a lens at depth 40 mm in elevation is responsible for the formation of two foci in the elevation profile at depth 18 mm. This strange situation of a HF imaging beam focused on two different locations at the same time has a dramatic impact on the spatial resolution of the system, and will be responsible as well to the creation of many distortions such as SURF aberrations for both focused and plane LF beams with the Viglen probe.

SURF aberrations

By definition, in the presence of SURF aberrations, the focusing of the HF imaging pulse will be altered by the LF manipulation pressure. Hence, the presence of SURF aberrations can be quantified by studying the presence of high differences in the HF focusing delays between the positively and negatively manipulated HF pules, as presented in Figures 4.20 and 4.21. This difference in focusing delays, expressed in nanoseconds, has to be compared of course with the HF pulse period: 125 ns for the Viglen probe, and 100ns for Okla probe. Hence, if such a difference is contained within 2 ns, the focusing process will be negligibly affected by SURF aberrations, while if the difference is above higher levels such as 5 or 10 ns, the delay between the HF pulses will be big enough to play a significant part in focusing and create a SURF aberration phenomenon.

The build-up of the SURF aberrations takes place in the depth range from the surface of the transducers to the location of the foci (i.e. from depth $z = 0$ mm to $19 - 20$ mm), called in the sequel the area of interest.

- In azimuth, for the configurations with focused LF beams (F-V) and (F-O), the difference in focusing delays is bounded between -1.5 ns and 1.5 ns in the area of interest. There will be a negligible level of SURF aberrations created in azimuth for (F-V) and (F-O). This means that the difference in the azimuthal focusing patterns of the HF and LF beams are not big enough to generate SURF aberrations.

- In azimuth, for the configurations with plane LF beams (P-V) and (P-O), high level of difference in the focusing delays (8 ns to 17 ns) are observed on the sides of the HF beam from depth 10 mm to 15 mm. Such delays are not negligible and will lead to the creation of important SURF aberrations in azimuth for (P-V) and (P-O). This situation was expected since the focusing pattern of a plane LF associated with a focused HF possess big differences, and results in attenuated HF imaging pulses in the focal area, as observed previously on the central axis of the transducers.

- In elevation, for the configurations with the Okla probe (F-O) and (P-O), the difference in focusing delays are negligible in the area of interest. There will be a negligible level of

SURF aberrations created in elevation for (F-O) and (P-O). The physical lens focusing both LF and HF beams with Okla is the similar for both beams, and the resulting difference in the focusing patterns is small enough not to generate SURF aberrations.

- In elevation, for the configurations with the Viglen probe (F-V) and (P-V), the presence of two foci at depth 18 mm not aligned with the central axis of the transducer is generated without the framework of the standard focussing process. The difference in focusing delays when approaching these two focal zones coming from the surface of the transducer rapidly reaches high levels (-10 ns), generating a high level of SURF aberrations in elevation for (F-V) and (P-V). This creation of SURF aberrations in the elevation plane with Viglen explains a lot of the disturbances that we observed on the central axis for the HF imaging plot: disturbances in the center frequencies and bandwidth of the filtered HF pulses, bigger attenuation of the HF pules close to the focus, ...

The study of the difference in focusing delays has shown that the generation of SURF aberration has to be investigated both in the azimuth and elevation directions. Such aberrations impacting in a non negligible manner on the resulting profiles on the central axis of the transducer, their importance has to be characterized for every beamforming configuration used.

4.4.4 On the performances in the imaging of nonlinear scatterers

Relative Amplitude Difference (RAD)

The Relative Amplitude Difference (RAD) between the positively and negatively manipulated pulses presented in Figure 4.22 is an indicator which may be compared to the experiments conducted with a real scanner, by comparing the RAD of the two successively received signals.

The RAD has been here computed after nonlinear propagation delays correction, on the central axis. This indicator therefore reflect the other distortions created by the nonlinear propagation of the SURF pulse.

- SURF aberrations play in important role in the importance of the RAD. In the previous section, we highlighted the fact that for the plane LF beam configurations (P-V) and (P-O), the SURF aberration build-up could already be distinguished at depth $z = 10$ mm, while this phenomenon only appeared close to the focus (near depth 14 mm) for the (F-V) situation. The SURF aberration result in big shifts in the RAD curves (for both the RMS- and maximum-based estimates), that can be clearly seen on the curves at the depths indicated just above.
- Compression/expansion of the pulse will result in a change of shape of the HF pulse envelope, but not in a dramatic change in the total pulse intensity (its RMS intensity). Therefore, the compression/expansion appears in in Figure 4.22 as a separation of the "max" curve from the "RMS" curve. One may notice that the effect of compression/expansion of the HF pulse are distinguished on the RAD curves from the focused LF configurations from the surface of the transducer (depth $z = 0$ mm) while it really appears for the plane LF configurations only after depth 15 mm (where the maximum in experienced pressure gradient has been reached).

From all the simulations, it appears that the configuration (F-O) is the one providing less amplitude difference due to a restricted amount of compression/expansion balanced with the absence of SURF aberrations.

Relative Tissue Suppression (RTS)

The Relative Tissue Suppression (RTS) presented in Figure 4.23 is an indicator that easily quantify the amount of suppression of linear scattering the SURF imaging process is capable to ensure. It can also be computed easily on real experiments based on the received signals from the scanner in the absence of nonlinear scatterers.

The levels of RTS, established here on the central axis of the transducers, quantify the ratio of the linear scattering that can be suppressed to the total scattering. Such levels are directly comparable to the results from Chapter 2.4, where we saw that a -24.9 dB level of RTS had to be reached in order to conduct a valid imaging of the nonlinear scatterers such as micro-calcifications.

A quick look at the curves presented in Figure 4.23 demonstrates that, even in the configuration (F-O) where the pulse distortions are minimized until the focus (i.e. the RAD is small until depth 20 mm), such levels of RTS can not be reached in the focus by a simple estimation and correction of the nonlinear propagation delays. A pulse-form correction filter will therefore be presented and tested in the next Chapter.

Chapter 5

Pulse form correction for efficient tissue suppression

5.1 Need for correcting the pulse-form distortions

The simulations of the propagation of SURF pulse complexes from Chapter 4 have shown that the nonlinear propagation effects have two main effects on the imaging system:

- the spatial resolution of the imaging system is limited (a phenomenon generated by the diffraction pattern of the LF manipulating beam as well as the SURF aberrations)
- the HF-filtered back-scattered signals from SURF pulses with different manipulation pressure polarities present a difference even in the absence of tissue nonlinearities, due to the existence of nonlinear propagation delays and the distortion of the pulse-form resulting from compression/expansion.

In order to efficiently image nonlinear scatterers such as micro-calcifications, one must therefore choose a setup configuration where the spatial resolution is as less limited as possible by the SURF propagation effects, and one must estimate and correct for delays and pulse-form distortions.

Delay correction has already been tested and implemented in real-time, and has improved the suppression of linear scattering with about 6 dB in vivo [27]. The experiments and simulations presented in this chapter have been designed for testing the efficiency of a new procedure correcting for the pulse-form distortions in the received signals.

5.2 Methods

In order to test the pulse-form correction filter, different data sets have been gathered, both from experimentation and simulation. They correspond to the signal received from differently manipulated SURF pulses propagating in an homogeneous tissue composed only of linear scatterers. The configuration setup with both LF and HF pulses co-focused on a same focal point has shown to be affected mainly be delays and compression/expansion, while it minimizes the SURF aberration phenomenon. Therefore, this configuration has been chosen to test our pulse-form correction filter in this chapter.

Simulations have shown that for detecting tissue nonlinearities for depth typically used in breast scanning (up to 25 mm), the Okla probe presented a better spatial resolution and a higher frequency separation than Viglen. Even though this inherent characteristics make the Okla probe more capable of imaging micro-calcifications, this probe is experimental and presented a non negligible amount of noise in the recorded signal due to a poor shielding of the electronic parts of the probe, making the acquisition of data impossible at depth > 15 mm. In the sequel, we shall therefore only test the pulse-form correction filter on data acquired with the Viglen probe.

5.2.1 Phantom measurements

All the laboratory experiments completed in this chapter have been done using the modified Ultrasonix SonixRP scanner presented in Chapted 4.1.2. For the phantom measurements, a CIRS model 049 (CIRS, Virginia, USA, [37]) elastography phantom was used. There are no wires or other resolution scatterers in the phantom, while the inclusions are located deeper than 30 mm, so the part of the phantom which is imaged is homogeneous with only ambient scattering. The probe is fixed to a Physik Instruments (Karlsruhe, Germany) multistage robot.

For each setup, 100 images spaced 1.5 mm apart in elevation direction are recorded. For each image, 50 frames are recorded and averaged to increase the SNR. Measurements consist of the recording of three data sets of received RF-signal:

1. the positively manipulated SURF pulse echoes
2. the negatively manipulated SURF pulse echoes
3. echoes from classical B-mode imaging (SURF with no LF manipulation present) to serve as a reference.

Only the 10 beams corresponding to the central part of the image were kept for processing, where no side effects can be denoted. The received data corresponding to the first 4 mm has been left because there are some near-field issues when receiving with the prototype probes.

5.2.2 Simulations of scattering from tissue

Data sets equivalent to the one acquired experimentally with Viglen have been simulated at ISB by Thor Andreas Tangen. The nonlinear 3D forward propagation of the SURF pulses have been simulated with the help of Abersim as described in Chapter 4.1. Scattering has been introduced to this data via a convolution of the propagated beam field with randomly located linear scattering source terms. Finally, the back-scattered signals are transformed into an RF-signal, and thus an image's beam, by numerically simulating the dynamic focusing of the probe. For each setup, the final data set consists of 1 frame of 384 independent beams, to which gaussian white noise is added with a SNR of 20 dB.

5.2.3 Processing before pulse-form correction

The processing was done on the received signal using MATLAB.

The received RF data was:

1. Filtered with a 60 taps bandpass filter with cutoff frequencies at 3 and 8 MHz.

2. IQ data is extracted using a 5.5 MHz demodulation and a 50 tap lowpass filter with 4 MHz bandwidth.

3. The IQ data is decimated by 4 (down to a sampling frequency of 10 MHz). This process was allowed by complex demodulation.

4. The delays between the positively and negatively manipulated pulses is estimated using the algorithm described in Chapter 3. The window size was set to 2 mm.

5. The delays were compensated on the IQ signals using cubic spline interpolation.

We denote $x_k(t)$ and $y_k(t)$ the IQ signals corresponding to a positive and negative manipulation pressure of the frame k in the elevation direction ($0 \leq k \leq 100$), and the respective delay-compensated signals are denoted $\hat{x_k}(t)$ and $\hat{y_k}(t)$. $\hat{z_k}(t)$ is formed by subtracting the two corrected signals.

The Relative Tissue Suppression (RTS) is computed as

$$\text{RTS} = \sum_{k=1}^{100} \frac{|\hat{z_k}(t)|}{|\hat{x_k}(t)|}. \tag{5.1}$$

The Relative Amplitude Difference (RAD) is computed in a similar fashion

$$\text{RAD} = \sum_{k=1}^{100} \frac{|\hat{x_k}(t)|}{|\hat{y_k}(t)|}. \tag{5.2}$$

For the case where no LF manipulation pressure is transmitted, no delay estimation nor correction is done, since it is both useless and could hypothetically remove to this case it's property of the optimal level of suppression.

For the center frequency and bandwidth recordings, the data was first filtered as presented on step 1 above. Then only a window of 1.5 mm around the focus was used. The data was windowed with a hamming window before a 512 points FFT was computed. The estimated center angular frequency $\hat{\omega}_c$ was computed as

$$\hat{\omega}_c = \frac{\int_{\omega_1}^{\omega_2} \omega \bar{p}(\omega) d\omega}{\int_{\omega_1}^{\omega_2} \bar{p}(\omega) d\omega} \tag{5.3}$$

where $\bar{p}(\omega)$ is the average power spectrum on the 100 frames, and ω is the angular frequency. The integration limits ω_1, ω_2 where chosen as the frequencies corresponding to the -6 dB values of the power spectrum to each side of its maximum. The estimated bandwidth corresponds to the spacing between these -6 dB limits.

5.2.4 Implementation of the pulse-form correction filter

The principle of the estimation of a correction filter for the distortions of the pulse form due to compression/expansion was already presented in Chapter 3.4. Such filter has been implemented in an iterative scheme on MATLAB. The complete code for the function may be found in Appendix C.

According to [3, chap. 8.2], the received signal from two differently manipulated pulses may be modeled as the convolution in real-time of the scanner transmit and receive spatial impulse

responses, the pulse excitation, and the scattering pattern. Such a convolution may be easily represented in the Fourier domain for the time/depth interval T_i:

$$\begin{aligned} X_{+,i}(\omega) &= H_{t,i}(\omega) \cdot H_{r,i}(\omega) \cdot U_{+,i}(\omega) \cdot \Sigma_{+,i}(\omega), \\ X_{-,i}(\omega) &= H_{t,i}(\omega) \cdot H_{r,i}(\omega) \cdot U_{-,i}(\omega) \cdot \Sigma_{-,i}(\omega), \end{aligned} \tag{5.4}$$

where $X_{\pm,i}(\omega)$ is the received signal spectrum (positively "+" or negatively "-" manipulated), $H_{t/r,i}(\omega)$ are respectively the spatial impulse response of the transmit and receive chain of the ultrasound scanner, $U_{\pm,i}(\omega)$ is the excitation command of the positively/negatively manipulated SURF pulse complex, and $\Sigma_{\pm,i}(\omega)$ is the scattering.

Scattering from tissue may be separated into its linear and nonlinear components as

$$\Sigma_{\pm,i}(\omega) = \Sigma_{l,\pm,i}(\omega) + \Sigma_{n,\pm,i}(\omega). \tag{5.5}$$

In an ideal situation where the scattering observed is only linear and is the same for both the negatively and positively manipulated SURF pulse complexes ($\Sigma_{+,i}(\omega) = \Sigma_{-,i}(\omega) = \Sigma_{l,\pm,i}(\omega)$) on the time/depth interval T_i, the pulse-form correction filter established in (3.51) will be reduced to

$$\hat{G}_i(\omega) = K_i(\omega) \frac{\left\langle X_{+,i}(\omega) X^*_{-,i}(\omega) \right\rangle_\Gamma}{\left\langle |X_{-,i}(\omega)|^2 \right\rangle_\Gamma} \simeq K_i(\omega) \frac{\left\langle U_{+,i}(\omega) U^*_{-,i}(\omega) \right\rangle_\Gamma}{\left\langle |U_{-,i}(\omega)|^2 \right\rangle_\Gamma}. \tag{5.6}$$

This means that the filter $\hat{G}_i(\omega)$ is correcting exactly for the difference in the diffraction pattern between the positively and negatively manipulated HF pulses, i.e. the difference in the pulse-form distortions.

In order to implement this filter, one must determine:

- a time/depth interval T_i where the distortion due to compression/expansion should be approximately constant, and where the linear scattering component should be equal for both positively and negatively manipulated pulses,
- the averaging area Γ on which the filter must be estimated.

Estimating the correction filter on a time/depth interval T_i is equivalent in signal processing to taking the estimate of a windowed version of the received signal, where the window contains T_i. This *estimation window* was chosen as a Tukey window, as show on Figure 5.1. The estimation window should be as small as possible to represent an interval where the compression/expansion effects are approximately constant. However, the estimation window should be big enough to contain sufficient information about the distortions to correct for: one will choose to consider a window length of a few HF pulse lengths. Finally, the scatterers responsible for the signal received on the extremities of the estimation window may not be the same for the positively and negatively manipulated pulses. The filter estimation will therefore not be correct for the sides of the window. One may limit this phenomenon by choosing the estimation window parameter α such as the transition region of the Tukey window (i.e. the region where the window value is different from 1) is bigger than the range resolution of the system: this leads to a transition region bigger than half of the HF pulse length.

Once the time interval T_i has been selected, one must determine on which data set Γ the estimation will be based, i.e. on which data set the averaging of equation (3.51) will be done.

- If we choose to estimate the filter for one specific beam on a specific frame, the filter estimate will be equivalent to a filter transforming the negatively manipulated received

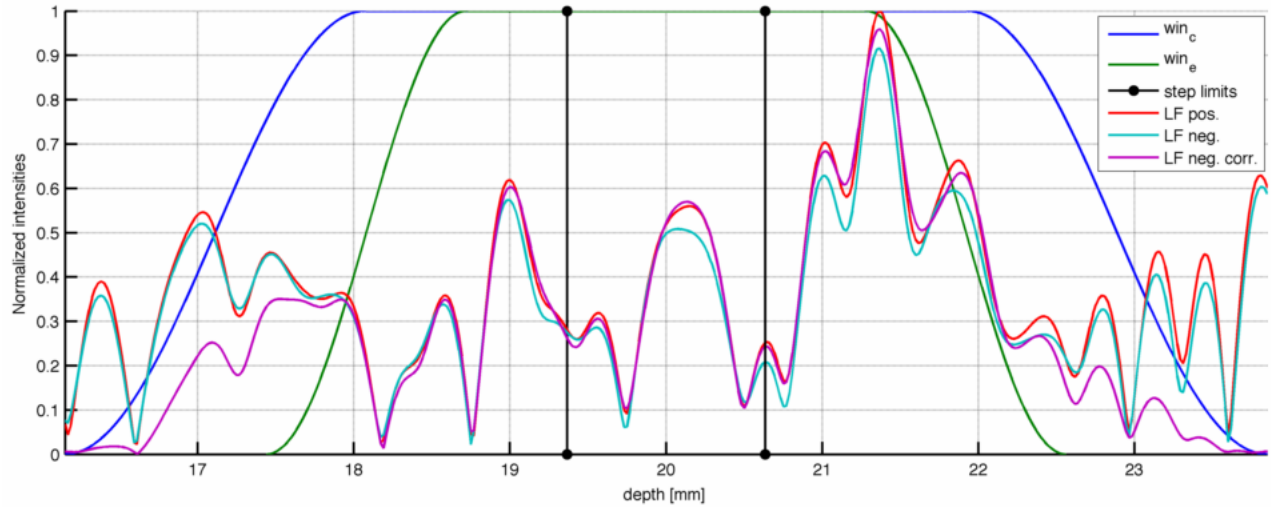

Figure 5.1: Illustration of the implementation of the pulse-form correction filter on a step around depth 20 mm in the absence of nonlinear scatterer. The estimation and correction windows (respectively denoted win_e and win_c) are Tukey windows. The transition region of the estimation window is chosen to be bigger than the range resolution of the system. Some example HF-filtered IQ-demodulated signals are presented for both positive and negative LF-manipulations (only the normalized absolute values of the IQ-signals are displayed here). The corrected signal for the negatively manipulated pulse is shown to be close to the signal from the positively manipulated pulse within the step limits.

signal in the positively manipulated signal. Such perfect filter will be useless since it will compensate for all the differences in the two received signals, and will therefore also remove the difference in the signals due to nonlinear scatterers. In order to correct for the distortions in the signal while saving the differences due to the nonlinear scatterers, one must estimate the Wiener filter on a larger data set Γ presenting the same kind of distortions due to compression/expansion, but resulting from different scatterers.

- A natural choice may be to estimate the filter by averaging on the different beams from the image. This has the advantage of allowing a filter to be estimated within only one frame, and therefore to have a quasi-real-time correction scheme. However, the real probes usually contains anomalies such as dead piezoelectric elements, and the resulting SURF pulse characteristics (delays, compression/expansion) may be different from beam to beam. In such cases, averaging on the different beams may provide for a bad estimate of the filter.
- Finally, the estimate may be computed by averaging on the successive frames. This method has the advantage of being independent of the probe defects, but requires similar types of tissues to be imaged at each frame. A change in the nature of the object imaged (due to a probe shift for example) will cause the received signals to be intrinsically different: the distortions present in the HF-imaging pulse will be different on the successive frames due to a change in the propagation medium that is imaged.

In the sequel, the method of averaging on the different beams will be used for correcting for pulse-form distortions in the simulated RF data sets (since no defects are present in the simulated probe), while averaging on the successive frames will be done for the experimentally acquired data (since the phantom imaged is supposed to be homogeneous).

When averaging, some of the samples may present some big variations between the positively

and negatively manipulated signal compared to most of the other samples. Such samples usually do not correspond to the distortions due to compression/expansion, and they will may lead to an inaccurate estimate of the pulse-form correction filter if they are taken into account when averaging on Γ during the estimation scheme. A way to remove for these samples in the estimation scheme is to implement a weighting average. The weighting coefficients must have a high values for signals with small distortions while being close to zero when the positively and negatively manipulated signals do not seem similar. Such weighting coefficients may be computed by considering the cosinus of the difference in phase angle of the two signals: for normal distortions, the signals may present difference in amplitudes, but their fluctuations should be close, and therefore the difference in their phase angle should be small ; while two signals not correlated would present high differences in phase angle. The weighting coefficients w_i, cosinus of phase angle difference, may be computed for each sample as:

$$\begin{aligned} w_i &= \frac{\Re\left\{X_{+,i}(\omega)\, X^*_{-,i}(\omega)\right\}}{\left|X_{+,i}(\omega)\, X^*_{-,i}(\omega)\right|} \\ &= \frac{\Re\left\{|X_{+,i}(\omega)| \exp^{j\angle X_{+,i}} \cdot |X_{-,i}(\omega)| \exp^{-j\angle X_{-,i}}\right\}}{\left|X_{+,i}(\omega)\, X^*_{-,i}(\omega)\right|} \\ &= \frac{|X_{+,i}(\omega)| \cdot |X_{-,i}(\omega)| \cdot \Re\left\{\exp^{j(\angle X_{+,i} - \angle X_{-,i})}\right\}}{\left|X_{+,i}(\omega)\, X^*_{-,i}(\omega)\right|} \\ &= \cos\left(\angle X_{+,i} - \angle X_{-,i}\right) \end{aligned} \tag{5.7}$$

The correction filter has been estimated on a set of beams/frames using an estimation window as depicted on Figure 5.1. But we have seen that due to the presence of different scatterers on the sides of the estimation windows, the filter estimate could not be optimal for these depths. A solution to this problem has been found by applying the estimated correction filter on a wider window, the *correction window*, and by then extracting the corrected signal as the very central part of the estimation window, called the *step*. A bigger correction window allows the scatterers located just outside the borders of the estimation window to be filtered and corrected for, and the "correction step by step" approach allows to keep only the best corrected part of the signal. Such notions are presented on Figure 5.1. In our results, only one step around the focal depth (20 mm) has been corrected to show the influence of the pulse-form correction filter. A further approach would be to correct the entire signals using overlapping steps (implemented in the code furnished in Appendix C), but is not of interest for the present study.

The filter obtained after estimation on a specific time/depth interval as described above is usually not optimal. Thus, an iteration scheme has been implemented in order to improve the estimate of the pulse-form correction filter. The filter estimate $\hat{G}_{n,i}(\omega)$ at step n on the time/depth interval T_i is computed from the weighted iterative scheme:

$$\hat{G}_{n,i}(\omega) = \hat{G}_{n-1,i}(\omega) \cdot (1 - \lambda(n)) + \hat{G}_{n-1,i}(\omega) \cdot G_{n,i}(\omega) \cdot \lambda(n) \tag{5.8}$$

where $\hat{G}_{n-1,i}(\omega)$ is the filter estimated at the previous step, $G_{n,i}(\omega)$ is the filter estimated based on the signals already corrected using $\hat{G}_{n-1,i}(\omega)$, and $\lambda(n)$ is a weighting function usually equals to 1 for $n = 0$ and decreasing with n. In order to limit the influence of noise in the iteration scheme, the signals are filtered using a FIR bandpass filter (denoted *RF-filter* in the sequel) after each step to remove the creation of harmonics outside the frequency band of interest.

Finally, one may find interesting to determine at which time we should correct for the pulse-form distortions. Should this processing be done before or after the delay correction ? We have seen when discussing on the choice of the estimation window that the window should be as small as possible while containing sufficient information about the variations of both positively and negatively manipulated signals. Correcting for the delays will reduce the difference in the phase angle between these two signals, and therefore allow the use of a smaller estimation window. Hence, the correction of pulse-form distortions will be executed only at the end of the processing, after correcting for the nonlinear propagation delays.

In order to summarize the configuration used for the pulse-form correction filter in the further presented results, some key facts have been gathered in Table 5.1.

Table 5.1: Configuration used for estimation of the pulse-form correction filter

Estimation window	4 HF pulse lengths, α-parameter 0.5 so that the transition regions equal 1 HF pulse length (twice the range resolution) on each side
Correction window	6 HF pulse lengths, the α-parameter has no influence
Step	2 HF pulse lengths, only one step around focal depth (20 mm)
Noise parameter	Ns = 0 (used in the Wiener gain)
Averaging area	• averaging on successive frames for experimental data • averaging on the different beams for simulated data
Iterations	10 iterations weighting function: $\lambda(n) = \max(0.9^n, 0.05)$ RF-filter: • FIR filter with 60 taps and bandpass [3.5, 9] MHz for experimental data • FIR filter with 60 taps and bandpass [4.5, 10] MHz for simulated data

5.3 Results

5.3.1 Results of the Tissue Suppression general procedure

All the results presented in this section are computed and displayed in a similar and comparable way for both experimental and simulated data.

Figure 5.2 shows the nonlinear propagation delays estimates, along with the superposition of the standard deviation of these estimates on the same graph (dashed green lines). We observe that the delays curves estimated for simulated and experimental data have the same shape "piecewise linear", with an inflection point around depth $z = 12$ mm. The delays obtained with the scanner are in average 1-2 ns higher than the ones obtained from simulated data, while the variance of the delay estimate is higher in the simulations. The delay curve for the non-manipulated HF pulse (also called B-mode in the graph legend) is really close to the zero value, as it was expected since the manipulation pressure is at the origin of the propagation delays.

The shifts in the center frequency of the received HF imaging pulse are presented in Figure 5.3, before and after the pulse-form correction filtering. All the curves are decreasing due to the frequency dependent attenuation of the propagating material. The non-corrected center frequency estimates have higher values and oscillate more for the simulation data than for the experimental measurements. Only the negatively manipulated HF-filtered received signal has been corrected with the pulse-form correction filter to look like the positively manipulated

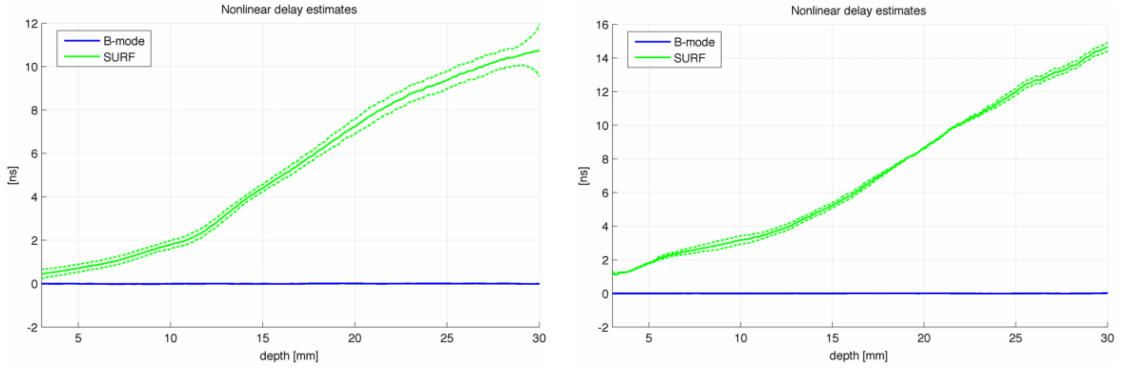

(a) from simulation data (b) from experimental measurements

Figure 5.2: Nonlinear propagation delays estimates for (a) the simulated and (b) the experimental results.

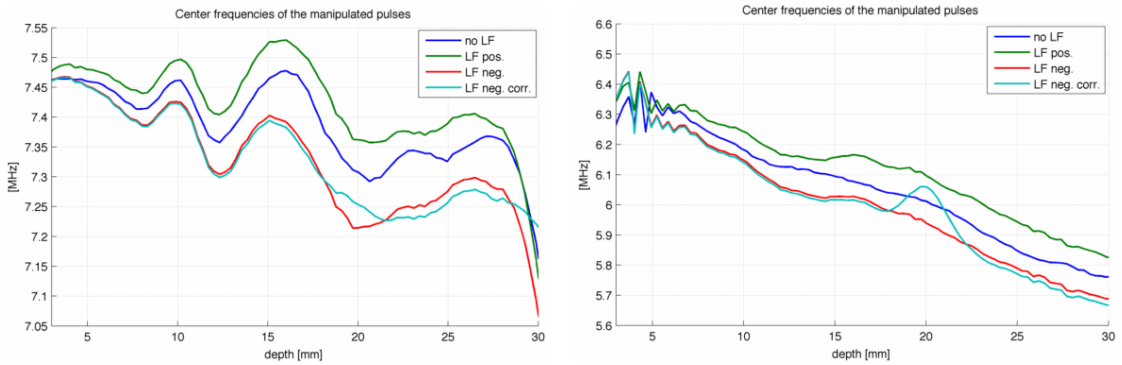

(a) from simulation data (b) from experimental measurements

Figure 5.3: Center frequency of the HF imaging pulse before and after the pulse-form correction for (a) the simulated and (b) the experimental results.

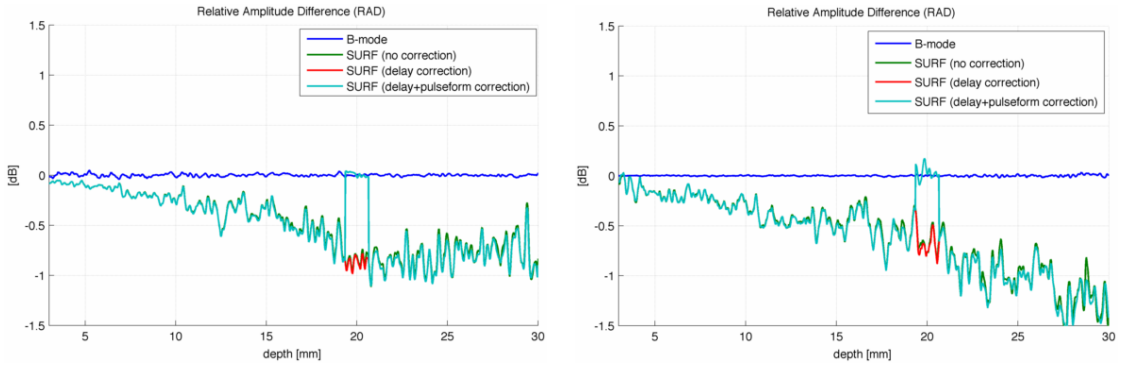

(a) from simulation data (b) from experimental measurements

Figure 5.4: Relative Amplitude Difference (RAD) between the positively and negatively manipulated pulses at the different steps of the imaging process for (a) the simulated and (b) the experimental results.

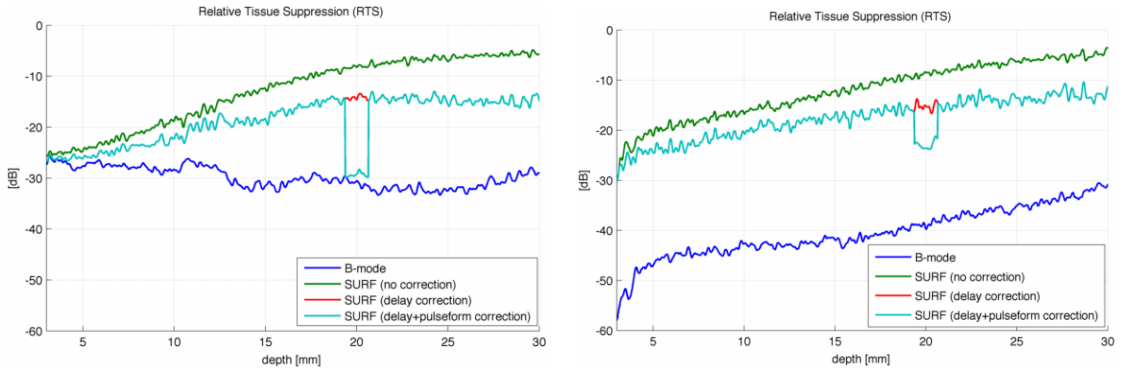

(a) from simulation data

(b) from experimental measurements

Figure 5.5: Relative Tissue Suppression (RTS) at the different steps of the imaging process for (a) the simulated and (b) the experimental results.

received signal. The pulse-form correction takes place on the interval [19.4, 20.6], and may be seen as a positive shift in the center frequency estimate on the curve of the corrected signal. This shift is bigger for the experimental data set. The corrected signals center frequency doesn't reach, however, the level of the center frequency of the positively manipulated pulse.

In Figure 5.4 the Relative Amplitude Difference (RAD) between the positively and negatively manipulated pulses is displayed at the different steps of the imaging process (on the raw received HF signal, after nonlinear propagation delays estimation and correction, and after the pulse-form correction filter). The RAD of the non-manipulated signal (B-mode) is close to zero, and gives an idea of the level of noise in the imaging system. As a general rule, the RAD curves increase in intensity with depth, and are very noisy. For both experimental and simulated data, we may observe that the propagation delay correction worsen the RAD slightly (about 0.1 dB), whereas the pulse-form correction applied on the interval [19.4, 20.6] create a clear diminution of the RAD. The corrected amplitude difference is inferior to 0.2 dB in intensity for the real phantom measurements, while it has RAD values comparable to the one of the B-mode for the simulation data.

Figure 5.5 presents the Relative Tissue Suppression (RTS) resulting from the imaging process after the different corrections applied to the received signals. Even though they are computed as an average over a high number of samples (100 frames for the experiments, 384 beams for the simulations), the curves are quite noisy. The RTS curve for the B-mode imaging gives an idea of the noise level present in the imaging system: there is clearly a higher intensity of noise in the simulation data (noise floor at -30 dB), while the noise floor for the experimental data is down to -40 dB for depths < 20 mm. The RTS curves for the manipulated signals (before and after delay correction) for simulations and experiments look very similar in shape and levels, even though they present a small 2-3 dB difference, especially close to the transducer surface where the scanner is known to have some issues. The biggest difference lie in the RTS curves from the pulse-form corrected signals. In the corrected depth interval, the level of suppression is close to the noise floor (at -29 dB) for the simulated data, while we only obtain -22 to -23 dB of tissue suppression with the experimental setup.

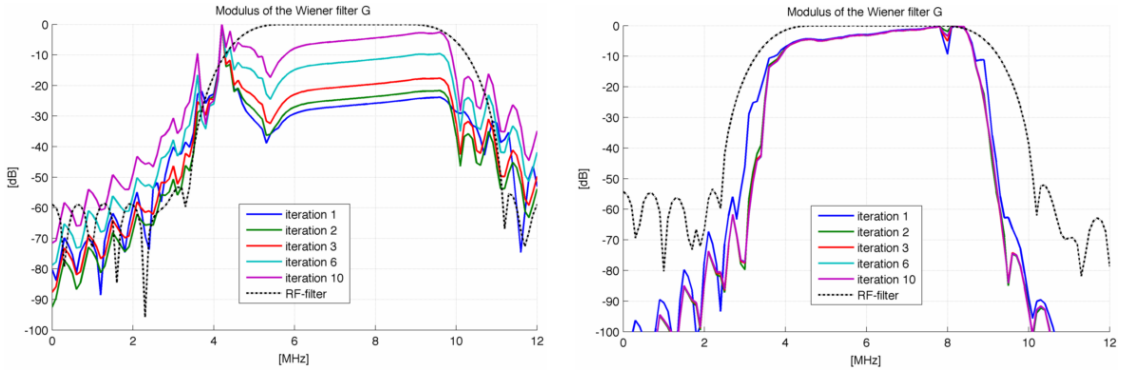

(a) from simulation data (b) from experimental measurements

Figure 5.6: Power spectrum of the pulse-form correction filter estimated, presented at different iterations, for (a) the simulated and (b) the experimental results, along with the RF-filer used for stabilization of the iterative process.

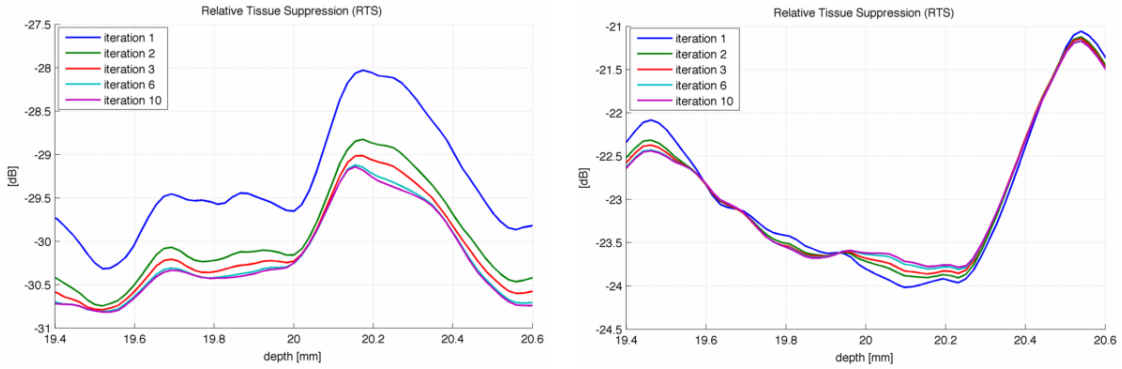

(a) from simulation data (b) from experimental measurements

Figure 5.7: Relative Tissue Suppression (RTS) in the corrected depth interval, presented at different iterations of the pulse-form correction process, for (a) the simulated and (b) the experimental results.

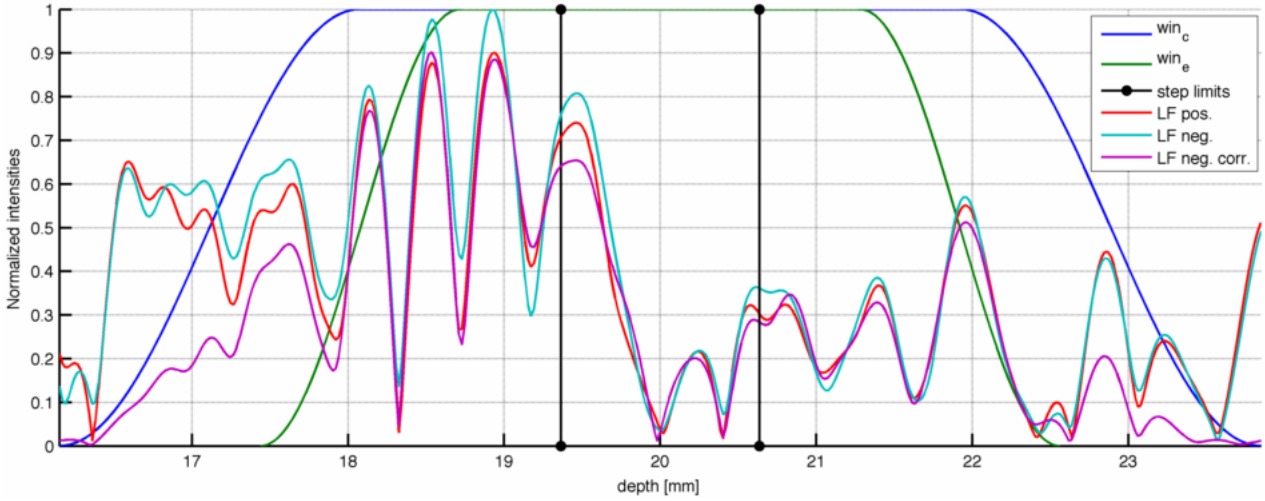

Figure 5.8: Effects of the pulse-form correction filter on the signals received from the scanner (experimental data). A comparable graphic has already been presented in Figure 5.1 for the simulation data, along with more explanations on which curves are displayed.

5.3.2 Results detailing the working of the pulse-form correction filter algorithm

The evolution during the iterative process of the power spectrum of the estimated pulse-form correction filter is presented in Figure 5.6 for both experimental and simulation setups. The bandpass RF-filter, applied after each iteration on the signals in order to remove the noise generated outside the imaging frequency band is also depicted (dashed black curve). One may observe a bigger evolution of the pulse-form correction filter estimate between the iterations for the simulation data than for the experimental data set, where the filter seems to converge more quickly. For the simulation setup, the filter estimated at the first iteration amplifies the frequencies around 4.2 MHz, which is out the imaging frequency band, and we can see that this amplification is reduced in importance over the different iterations.

Within the corrected depth interval, it may be of interest to look at the impact of the pulse-form correction filter after each iteration on the Relative Tissue Suppression (RTS), as presented in Figure 5.7. We can see that the curves for the iterations 6 and 10 are really close to each other: the RTS indicator converges quickly for both the simulated and experimental data sets. The level of correction is from the first iterations higher for the simulations, as already presented in the previous section (-30 dB of RTS for simulations compared to -23 dB for data from the scanner). On the opposite of the curves for the RTS of the simulations, which improve at each iteration, the curves of tissue suppression of the experimentally acquired data converge into a curve that do not provide a better correction at all depth compared to the previous iterations (especially around depth $z = 20.1$ mm).

The impact of the pulse-form correction filter on the processed signals is presented for the simulation and experimental data sets respectively in Figures 5.1 and 5.8. Along with the received and corrected signals, the depth delimitations of the correction step, as well as the correction and estimation windows win_c and win_e. The difference in the quality of correction of the negatively manipulated signal between the experimental and simulation setups can be easily seen by the human eye. If the corrected curve seems to fit properly the positively manipulated curve on the correction step/interval for the simulation data, we can observe big differences in the experimentally-acquired signals on the same interval (e.g. around depth $z = 19.5$ mm).

5.4 Discussion

5.4.1 On the possibility of comparing between the experiments and the simulations

The estimated profiles of the nonlinear propagation delays (Figure 5.2) and of the imaging pulse center frequency (Figure 5.2) confirm the similarity of the experimental and simulation setups. But, even though the simulation has been designed to imitate the experiment by selecting similar apertures on the transducer, approximatively similar pressure levels, and approximatively similar initial phase relation between the HF and the LF pulses, we can of course denote some differences between the setups:

- First, we noticed that the level of the estimated nonlinear propagation delays was higher in the experiments. This means that the pressure experienced by the HF pulse in the experiments is slightly higher than in the simulations, and therefore the phase relation between the HF and LF pulse has not been the same in the two setups. In Appendix B,

we evoke the fact that the phase relation between the HF and LF pulses is dependent of both the level of manipulation pressure and the propagating material (via the speed of sound). If the exact evolution of the phase relation may be known for the simulations, the phase relation is rather uncertain with the scanner (it has been calibrated based on water-tank measurements, but this makes the calibration wrong when scanning a phantom which possess different material characteristics, and therefore a different speed of sound). Hence, a small variation in the phase relation between the experiments and the simulations may exist, creating a slight change in the values of the propagation delays, but without affecting too much the study of the pulse-form correction filter via a comparison of the experiments to simulations.
A higher standard deviation in the estimates of the nonlinear delay had also been observed for the simulation. A key requirement for simulating some received data to test the pulse-form correction mechanism was to simulate a data set with at least as much noise as in the experimentally acquired data. Such higher standard deviation is just confirming that we have achieved the requirements, and that pulse-form correction on the simulated data should be a more difficult task to complete. This higher level of noise can also be observed via the "noise floor" in the RTS curves in Figure 5.5: the RTS curve computed based on two successive non-manipulated (B-mode) pulses is representative of the level of noise in the system. The SNR was found to be higher for experiments than for simulations. A good explanation to the presence of such a low level of noise in the experimental data sets is that each RTS curve is computed based on 100 frames, which are themselves the mean of 50 frames automatically done by the experimental acquisition procedure, whereas the RTS curves of the simulations are only based on 384 independent beams.

- The center frequency estimates of the HF pulse were following a comparable decline due to the frequency dependent absorption, but the center frequency curves from the simulated data sets oscillated a lot and were located at a higher level (around 7.4 MHz compared to the 6 MHz of the scanner). This observation doesn't mean that we made a huge mistake when completing the simulations, but is the result of the filtering happening in the scanner receiver chain. The scanner is not an ideal system, and the receiving electronics components (the probe, the coaxial cables, as well as the received board inside the scanner) induce a filtering of the received signals. Such a phenomenon has already been explained and commented in [18, chap. 4.4] where a transfer function of the receiving chain was presented. Since the experiments conducted in [18], the electronics of the scanner have been modified, and some of the negative effects of the transfer function have been limited. However, some frequency filtering is still happening to the data received with the scanner which suppress some informations such as the oscillations in the HF pulse center frequency, and reduces the center frequency of the imaging signal down to 6 MHz.

To summarize, the experimental and simulation setups have their own singularities due to the intrinsic difference between data acquired and data simulated, but we are facing two similar data sets, where a reasonable and advised comparison should be possible.

5.4.2 On the efficiency of the pulse-form correction filter

The Relative Amplitude Difference (RAD) and Relative Tissue Suppression (RTS) are two useful indicators when it comes to the study of the impact of nonlinear propagation effects on a SURF imaging system. The goal of the ideal SURF imaging system in the presence of linear scattering only is to obtain a RAD as close to 0 dB as possible, while getting a RTS ratio as small as

possible, i.e. having RTS values as close as possible from the noise floor. We defined this noise floor as the curve obtained when computing the RTS for two consecutive non-manipulated (B-mode) pulses. It should theoretically be only affected by the thermal noise in the electronics, that can not be removed, and therefore correspond to the minimal RTS values achievable.
In our study, the RAD and RTS presented in Figures 5.4 and 5.5 showed that we obtained better results when applying pulse-form correction on the simulated data:

- On the corrected depth-interval from simulations, the level of the RAD is close to 0 dB, with variations equal in intensity to the noise in the RAD curve for the B-mode ; while the RTS curve is located around -29 dB only 1 dB above the noise floor. Such good results mean that for the simulation data sets, we corrected the signal with a pulse-form correction filter which is really close to ideal correction filter.
- The results obtained for the experimental data sets are however not as good: even though the RAD curve over the corrected depth-interval is close to zero (contained between ± 0.15 dB), the level of variations is sensibly higher than the noise level. This is conformed by the RTS curve which only performs a correction up to -23 dB of tissue suppression, far from the -38 dB of the noise floor.

While the algorithm for estimating and compensating for the nonlinear propagation delays gave an average diminution of 8 dB of linear scattering from tissue, *the pulse-form correction filter provides an additional diminution of respectively 7 dB and 15 dB of the linear scattering component for experimental and simulated data sets.* Such results have to be compared with the considerations on the level of tissue suppression required for detecting nonlinear scattering from incompressible particles such as micro-calcifications surrounded by linear scattering from tissue, established in Chapter 2.4. A level of RTS of -24.9 dB was required in order to ensure the detection of even the smallest micro-calcifications. *This detection is performed around depth 20 mm by the SURF imaging method with the new pulse-form correction filter when it is applied on the simulation data sets, but not on the measurements conducted with the scanner on the phantom.* It is of interest to investigate why the pulse-form correction filter acts with such limitations when applied on experimentally acquired data.

5.4.3 On the iterative pulse-form correction scheme

By applying the same pulse-form correction filter on two approximatively similar data sets, we observed two radically different results. The study of the iterative scheme may give some clues of why the filter is not correcting the experimental data correctly.

If we compare the shape of the power spectra of the pulse-form correction filters estimated in Figure 5.6, we observe a similar shape of a "tilted plateau" between the frequency bands [5.5, 9.5] MHz for the simulations and [3.5, 8.5] MHz for the experimental data. This plateau has the effect of attenuating with a linear inverse frequency dependance in the above-cited frequency bands. By doing this, the filter increases the center frequency of the corrected negatively manipulated pulse, such as it goes closer to the spectrum of the original positively manipulated HF pulse spectrum, as we already observed in Figure 5.3.
In the case of the simulations, we may observe a zone of important magnitude at the left of the "plateau" (in the frequency band [3.5, 5] MHz), but this zone has a tendency to enhance some frequency components of the signal outside the imaging frequency band, and is highly attenuated by the iterative process (and nearly entirely removed by the RF-filter), while the "plateau" is not affected by the iterations.

In both setups, we observe that the shape of the "plateau" zone of the pulse-form correction filter is not affected in a significant manner by the iterative process, and that these iterations converge to a filter where this "plateau" plays a significant role. We can therefore deduce that *this specific tilted "plateau" shape is an effective compensation of the nonlinear propagation effects.*

The convergence process may also be observed when comparing the RTS ratio on the corrected depth interval for the different iterations, as presented in Figure 5.7. For both the simulation and the experimental data sets, the RTS curves converge to a limit curve, which is a maximal improvement close to the noise floor for the simulated data, and a stabilization around -23 dB for the data from the scanner. The iterative scheme is estimating a pulse-form correction filter with a pretty similar shape in the two setups, and leads to a convergence of the RTS indicator. This last observation leads to the conclusion that *the iterative scheme is working correctly for both the simulation and experiments, but some limitations external to the pulse-form correction filter estimation are generating the difference.*

The pulse-form estimation has been based on the Wiener filter, which estimates a filter minimizing the difference between the two signals on an averaging area Γ. This averaging area Γ is constituted of successive frames spaced 1.5 mm apart in elevation for the experimental data, and of entirely independent beams for the simulations. We ensured that the pulse-form correction filter was also independent of the transducer specificities (anomalies, dead elements, ...) by estimating the filter on the frames for the experiments.
Therefore, the pulse-form correction filter efficiency can only be limited by two factors left to discussion:

- The first limitation may be due to the *speckle* nature of the signal received from an ultrasound imaging system: the interferences in the scattered ultrasound field from different scatterers will lead to the creation of artifacts, called speckles, in the received signal ([4, chap. 7]). The speckles are dependent of the geometrical repartition of the scatterers in the observed tissue, and of the ultrasound beam. Thus, the differences between the positively and negatively manipulated HF beams from SURF pulse complexes denoted in Chapter 4 will lead to a difference in the back-scattered components $\Sigma_{l,+,i}(\omega)$ and $\Sigma_{l,-,i}(\omega)$ of our model from equations (5.4) and (5.5). Such a difference between the linear scattering sources is a contradiction with the hypothesis necessary to establish the ideal filter in equation (5.6). In other words, *the presence of different speckle patterns for the positively and negatively manipulated pulses, which are independent on each frame, will lead to the estimation of a pulse-form correction filter which do not correct for this difference in the speckle pattern (but just in the difference in the average speckle pattern), since the correction has to be common to all the averaging area* Γ *(i.e. all the frames).*
  Speckles are present naturally in the experimental measurements while only gaussian distributed scatterers have been added to the simulations, creating a speckle pattern with a null average when compared to a high number of beams. This means that the filter estimated for the experimental measurements is impacted in its performances by the presence of this speckle pattern, while it is not for the simulations. One may easily imagine some solutions to minimize the presence of speckles and, thus, improve the filter: the use of techniques such as spatial compounding, with both LF and HF plane wave beams steered in successively different directions, and associated in receive to a Multiple Line Acquisition (MLA) system, may be implemented on the scanner. Frequency compounding may also be investigated. Such techniques are currently at a stage of development, and their early applications still need to be improved to obtain a sufficient reductions of the speckles.

- A second limitation, which may explain a lot of the limitations of the pulse-form correction

in the experimental data, is the level of nonlinear scattering from the phantom. The elasticity phantom used in the experiments, a CIRS model 049 (CIRS, Virginia, USA, [37]), is mainly composed of small Sephadex ([38]) balls, and the exact properties of this material such as the nonlinear scattering component is unknown. The presence of nonlinear scattering from the Sephadex balls may simply lead to a reduced level of RTS, since it is a part of the normal working of pulse-form correction filter not to remove the nonlinear scattering used by the SURF imaging procedure. Hence, *the presence of nonlinear scattering from the Sephadex balls may explain the difference in the observed performances of the pulse-form correction filter between the experiments and the simulations.*

Chapter 6

Conclusion

The real-time detection of nonlinear scattering from stiff particles such as micro-calcifications based on ultrasounds is a goal that may be reached soon with the help of dual frequency band techniques such as SURF imaging. The study of the interaction between two frequency-independent forward propagating ultrasound beams led to the discovery and first quantifications of the complex distortions experienced by the HF pulse. Such distortions appeared to become relatively important when the LF manipulation pressure reached high intensity levels such as the ones required for the detection of micro-calcifications. Further studies were required to predict how these distortions are dependent of the beamforming configuration, as well as the geometry of the transmitting transducer and the propagating medium characteristics. Moreover, if the nonlinear propagating delay have been characterized and successfully corrected for in the presence of low levels of manipulation pressures, the other distortions still require an efficient correcting process that may run in real-time on the SURF scanners.

Throughout this Master Thesis, the nonlinear propagation effects have been more extensively investigated. Numerical simulations based on the geometrical specifications of the first manufactured experimental SURF probes have been conducted to test if the first "rules of thumbs" extracted from theoretical and idealized models (for some of them still used in the daily development of the SURF methods), may be or not trusted. The results permitted the characterization for the real applications of the nonlinear propagation distortions as well as the importance of their impact on the received signal:

- The importance of using a SURF probe dedicated to the exact desired application has been highlighted by the simulations on Viglen, where the resolution of the system is highly impacted by the presence for the HF beam of two foci separated from the transducer axis in the elevation direction. This situation is the result of the presence of a physical lens on the surface of the transducer focused at 40 mm in elevation, and leads to the creation of important distortions such as SURF aberrations.

- A big challenge in the dual frequency band methods is to control the timing between the LF and HF pulses throughout the propagation of the pulse complex. The study of the profiles of the phase relation has shown a dependency of this timing to the manipulation pressure level, to the apertures geometries and to the speed of sound in the propagating medium.

- The phenomenon of compression/expansion and its effects on the HF pulse shape and spectrum result from the manipulation pressure difference over the imaging pulse. Such

distortions may be limited with the use of sharply focused HF beams, and/or the superposition on a plane LF beam. However, their existence can not be avoided if the difference in experienced pressure is above 600 kPa among the HF pulse.

- The SURF aberration phenomenon results from a difference in the focusing and diffraction patterns of the HF and LF beams. The level of aberration may be quantified in simulations by the computation of the difference in the focusing delays between positively and negatively manipulated pulses. It appears that SURF aberrations could be neglected for the co-focused situations (for probes adapted to the conducted study, in the opposite of Viglen). In the configurations where a plane LF beam is used in superposition to a focused HF beam, the level of SURF aberrations was such that it reduced the level of suppression from linear scattering by 3 dB.

This report was also the occasion to present and test the design and implementation of a new *pulse-form correction filter* compensating for the distortions induced by a different manipulation pressure on the HF pulse. The pulse-inversion scheme used by the SURF imaging technique has shown to furnish an 8 dB level of suppression of the linear scattering from tissue in the typical applications (with a manipulation pressure level around 1 MPa and an low level of SURF aberrations), far from the 25 dB theoretical level of suppression required for the efficient detection the smallest micro-calcifications.
While the nonlinear propagation delay estimation and correction algorithm has shown to improve this previous level by 8 dB in average, the new pulse-form correction filter has demonstrated to give an additional 7 dB of suppression on the experimentally acquired data sets, bringing the total level of reduction of the linear scattering up to 23 dB.
This same pulse-form correction filter applied on simulated data sets has performed a more proper correction of 15 dB, reducing the linear scattering components in the image of 29 dB (only 1 dB close to noise floor), ensuring a 4 dB contrast level between the micro-calcifications and the surrounding tissue.

Chapter 7

Further work

The simulations conducted in this report have shown that of the SURF probes, neither Viglen, neither Okla did provide a sufficiently good spatial resolution combined with a minimization of the nonlinear propagation effects when the manipulation pressure is around 1 MPa. The detection of micro-calcifications require a probe with frequency and focal capabilities adapted to this specific application. Such a probe, named Vora, is already under design, and further simulations and investigations of this probe capabilities will require to be conducted.

The pulse-form correction filter developed in in this paper appeared to present several limitations. The possibilities of improvement of this filter must be explored: adaptation of the algorithm to a quasi-real-time application, implementation of a nicer correction on a big depth interval using overlapping steps, apply the filter in different directions (e.g. on both azimuth and range directions) to reduce the spatial (and speckle) dependency, increase the understanding of the estimation process and improve it...

Some improvements may also be done on the SURF scanner: implementation of frequency and spatial compounding allowing the transmission of dual frequency band pulse complexes with HF and LF as both plane wave beams, for reducing the speckle dependancy of the images and increasing the framerate (which is a big deal with SURF imaging where twice the usual number of beams must be transmitted) while in the meantime limiting the compressions/expansions and the SURF aberrations; introduce a better configuration of the initial phase relation, with an automatic calibration dependent on the manipulation pressure level and a specified speed of sound; limit the current issues with the level of noise introduced by the poor shielding of the probes or the creation of intermediate frequencies and attenuation of the high frequency band by the electronics of the receive chain; and test the new SURF imaging schemes including non-manipulated pulses, or negative HF pulses associated to negatively manipulated pulses...

A further investigation of the phantoms also requires to be conducted: throughout this project, a phantom containing micro-calcifications has been realized following the recipe in [15] to test the pulse-form correction algorithm. However, the micro-caclifications have shown to be too big and detectable on a classical B-mode image, removing the possibilities to see the improvements the SURF imaging may give.
An other problem encountered with phantoms was the unknown level of nonlinear scattering of the Sephadex balls. This must be investigated further, for example once the SURF procedure for characterization of tissues (and thus, of the nonlinear compressibility parameter $\beta_{na}\kappa_a$) has been developed as described in [7].

Finally, the water-tank studies conducted on the Okla probe have shown that the simulations conducted with Abersim were not exact since it did not take into account the directivity of the elements, which caused some problems when simulating the propagation of fields from curved transducers. A way to solve this problem is to adapt the XdSim software for the generation of the initial pulse field by the Field II framework, and then to complete the nonlinear propagation with Abersim. An alternative to Abersim for the propagation of SURF pulses has also been proposed in [39] using the power GPUs, improving the simulation speed sensitively.

Appendix A

Additional results to the Abersim simulations conducted in Chapter 4

The simulations conducted in Chapter 4 of the nonlinear forward propagation of SURF pulse complexes from the Okla and Viglen probes in muscle provided an important amount of data. Most of the interesting results have been presented and discussed in Chapter 4.3 and 4.4, but many of them haven't, in a concern to keep a minimum of clarity in the presentation.

These unpublished results are presented here in the absence of any discussion, and the reader may refer to the extensive discussion previously conducted to easily understand the phenomenons involved.

A.1 Results in the azimuth and elevation planes of the transducer

The computation of the beam profiles in the azimuth and elevation planes allow the understanding of the diffraction pattern induced by the transducer geometries and setup configurations. Such beam profiles have been computed by considering the maximum of the filtered pulse envelopes at each position, and are presented in Figures A.1, A.3, A.5 and A.7. The depth-normalized profiles were also computed by normalizing the computed values with the maximum found in the plane corresponding to each depth. So called "boundaries" were displayed on the graphs corresponding to the -6dB limits of the beam profiles at each depth. Such depth-normalized pressures are presented in Figures A.2, A.4, A.6 and A.8. At first sight, a big difference in the diffraction patterns of the Viglen and Okla probes exists for the LF beams, while the HF beams mainly differ only in the elevation plane. Moreover, the true focal zones are located before the pre-configured focal depth of 20 mm.

The phase relation between the HF and LF pulses may also be computed in the elevation and azimuth planes, and may be observed in Figures A.9 and A.10 for the different configurations. The profiles exposed here have been computed only within the -6dB boundaries of the beam profiles, where the SURF pulses are notably present. Inhomogeneities in the phase relation in these planes explain the complexity of the distortions observed in focus. We denote that the configurations with focused LF beams have a more homogeneous phase relation up to the focus than the configurations using plane LF beams. Once again, the phase relation can not

be estimated after the focus (depth $>$ 27 mm), so the presented values have a high risk of inaccuracy, and will not be taken into account for the discussion of the results.

Different phase relations implies different manipulation pressures experienced by the HF imaging pulse. The profiles of the pressures experienced by the HF pulse, as well as the maximal difference in manipulation pressure experienced by the HF imaging pulse, are presented in the azimuth and elevation planes for the different configuration setups in Figures A.11, A.12, A.13 and A.14. The profiles computations were limited to the zone within the -6dB boundaries of the HF beam profiles, and the values presented may be erroneous in the zone where the phase relation may not be correctly determined (depth $>$ 27 mm).

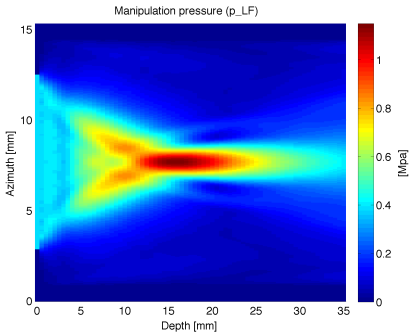

(a) (F-V)

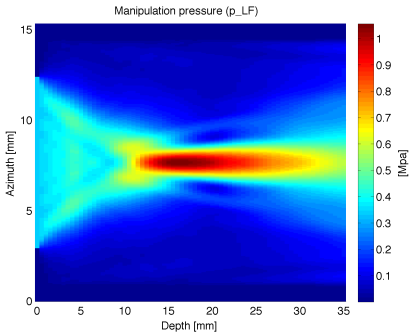

(b) (F-O)

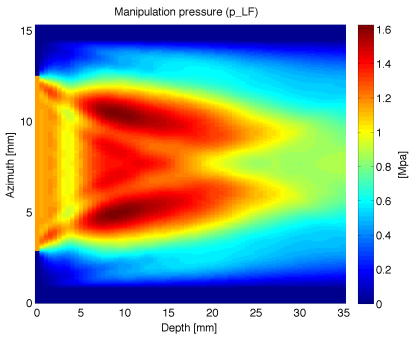

(c) (P-V)

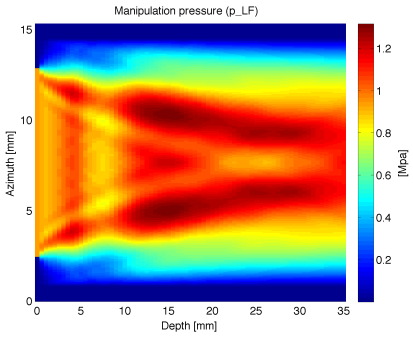

(d) (P-O)

Figure A.1: Profiles of the LF manipulation pressure in the azimuth plane for the different configurations.

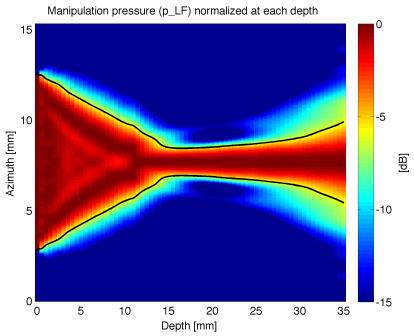

(a) (F-V)

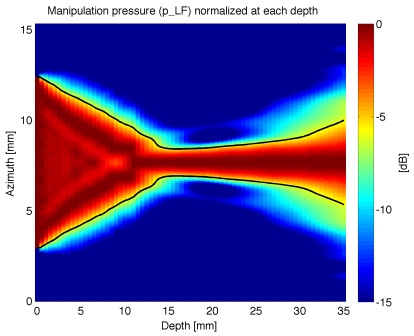

(b) (F-O)

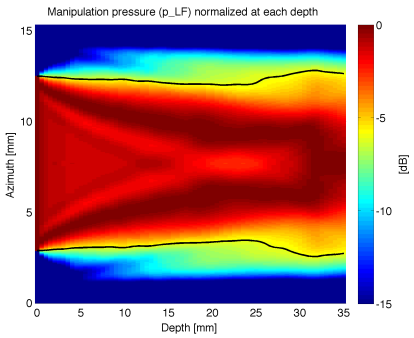

(c) (P-V)

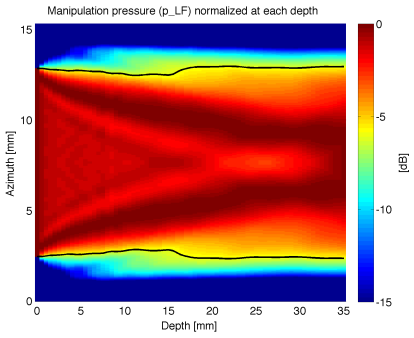

(d) (P-O)

Figure A.2: Normalized profiles of the LF manipulation pressure in the azimuth plane for the different configurations.

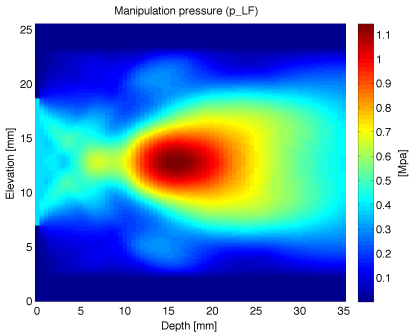

(a) (F-V)

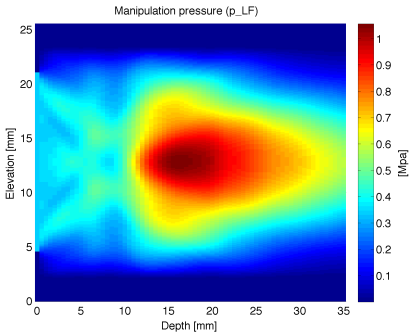

(b) (F-O)

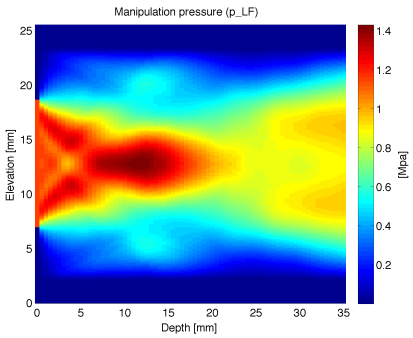

(c) (P-V)

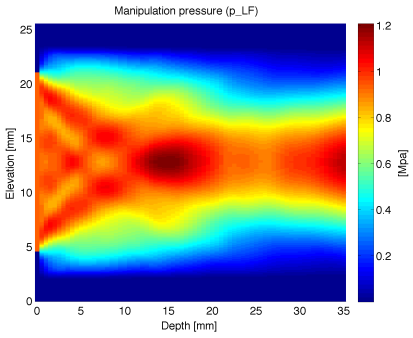

(d) (P-O)

Figure A.3: Profiles of the LF manipulation pressure in the elevation plane for the different configurations.

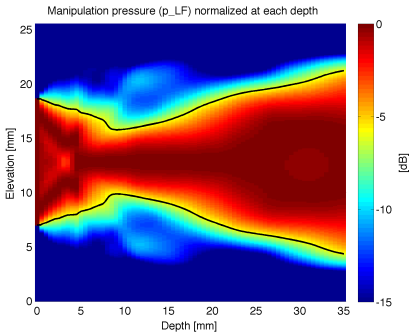

(a) (F-V)

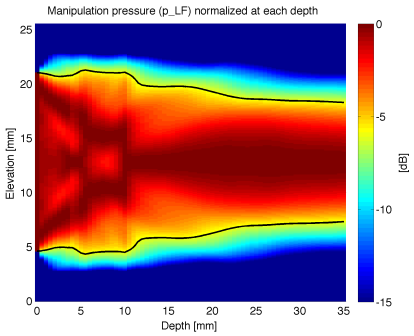

(b) (F-O)

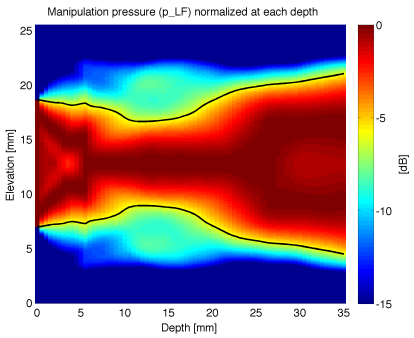

(c) (P-V)

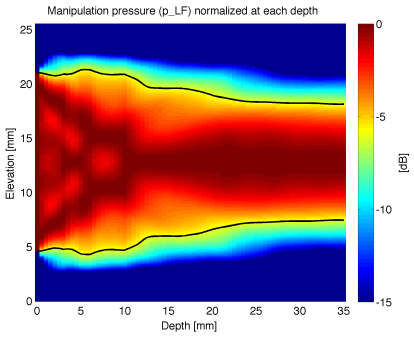

(d) (P-O)

Figure A.4: Normalized profiles of the LF manipulation pressure in the elevation plane for the different configurations.

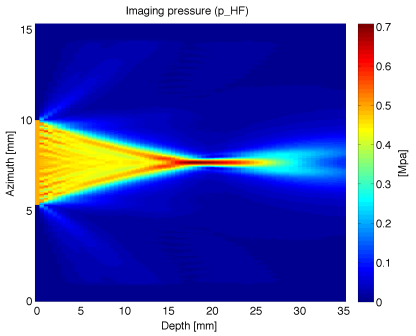

(a) (F-V)

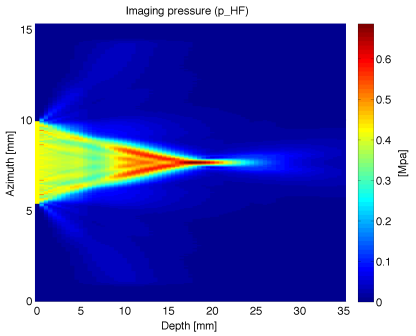

(b) (F-O)

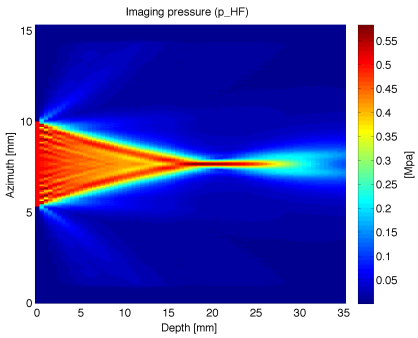

(c) (P-V)

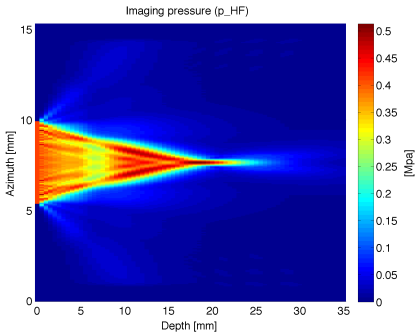

(d) (P-O)

Figure A.5: Profiles of the HF imaging pressure in the azimuth plane for the different configurations.

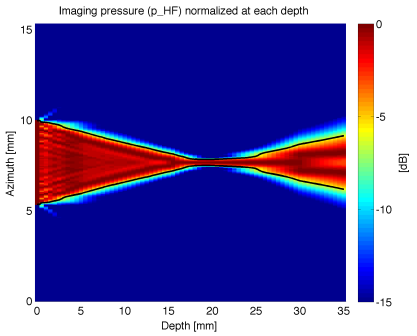

(a) (F-V)

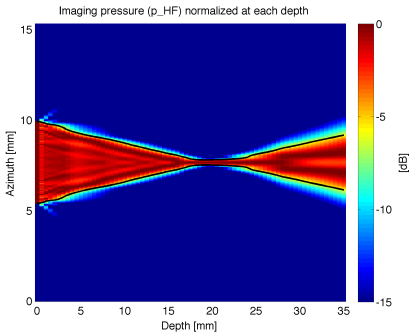

(b) (F-O)

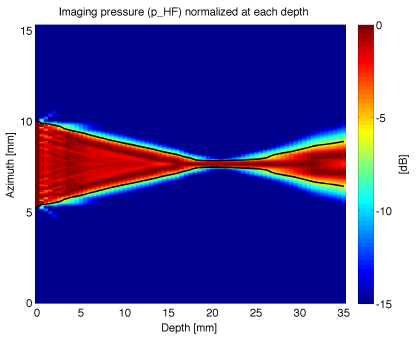

(c) (P-V)

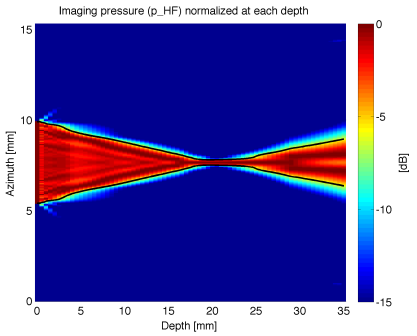

(d) (P-O)

Figure A.6: Normalized profiles of the HF imaging pressure in the azimuth plane for the different configurations.

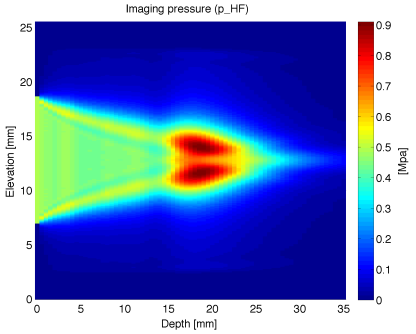

(a) (F-V)

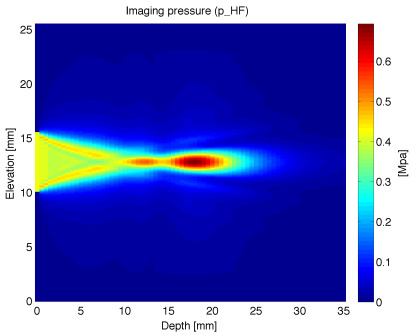

(b) (F-O)

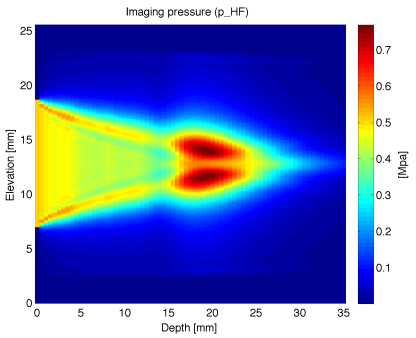

(c) (P-V)

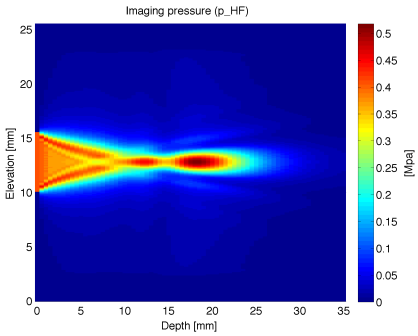

(d) (P-O)

Figure A.7: Profiles of the HF imaging pressure in the elevation plane for the different configurations.

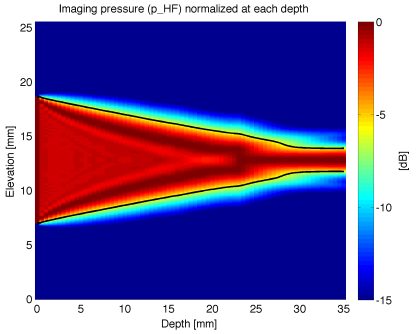

(a) (F-V)

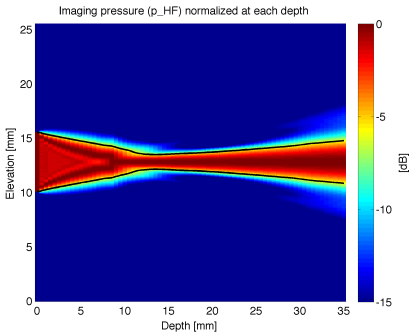

(b) (F-O)

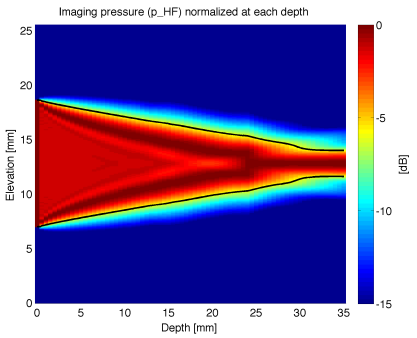

(c) (P-V)

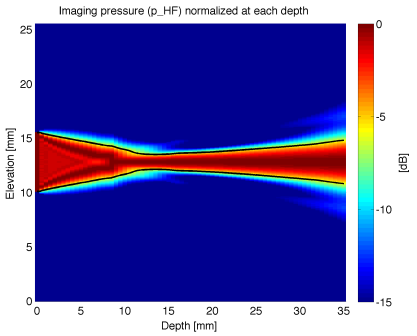

(d) (P-O)

Figure A.8: Normalized profiles of the HF imaging pressure in the elevation plane for the different configurations.

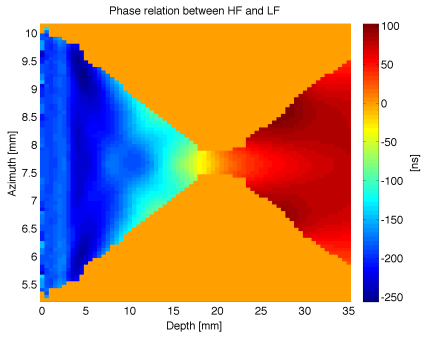

(a) (F-V)

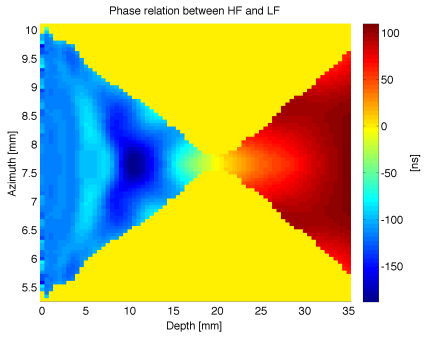

(b) (F-O)

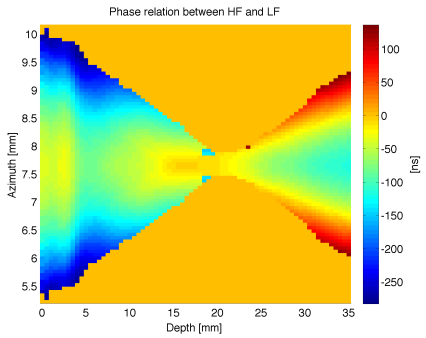

(c) (P-V)

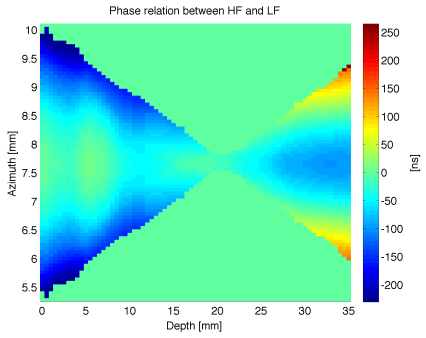

(d) (P-O)

Figure A.9: Profiles of the phase relation between the LF and the HF in the azimuth plane for the different configurations.

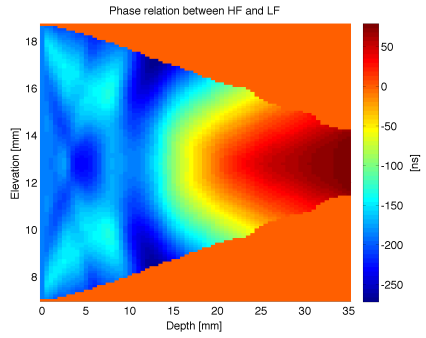

(a) (F-V)

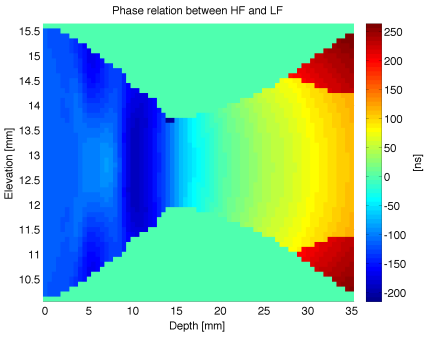

(b) (F-O)

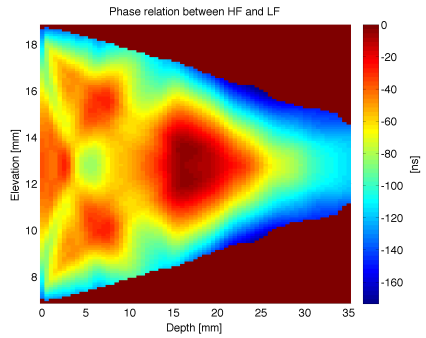

(c) (P-V)

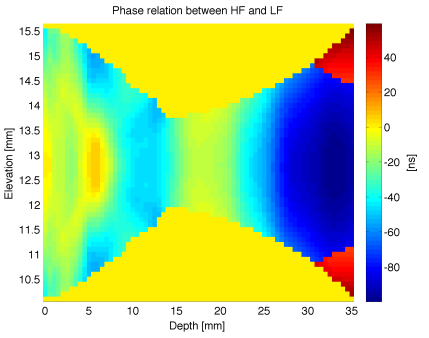

(d) (P-O)

Figure A.10: Profiles of the phase relation between the LF and the HF in the elevation plane for the different configurations.

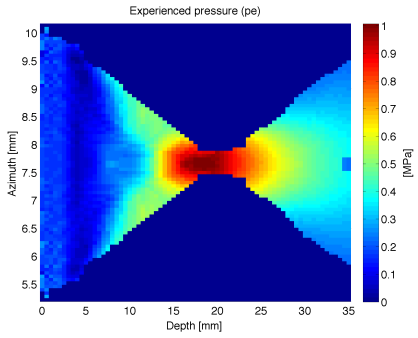

(a) (F-V)

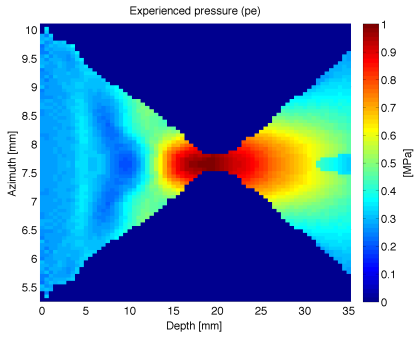

(b) (F-O)

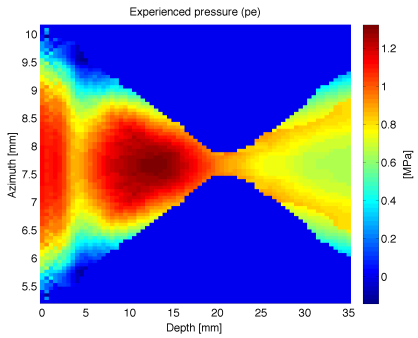

(c) (P-V)

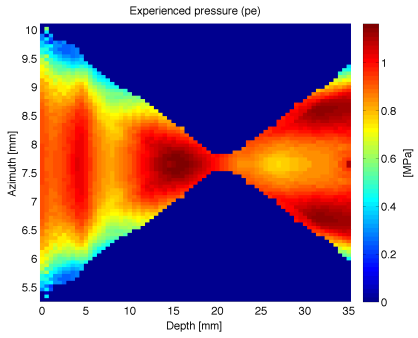

(d) (P-O)

Figure A.11: Profiles of the manipulation pressure experienced by the HF-imaging pulse in the azimuth plane for the different configurations.

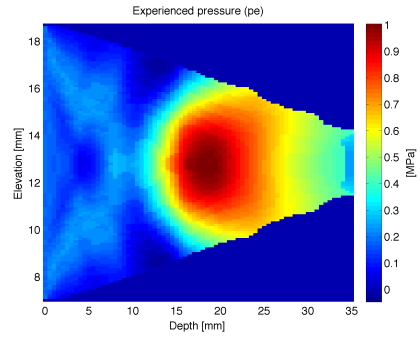

(a) (F-V)

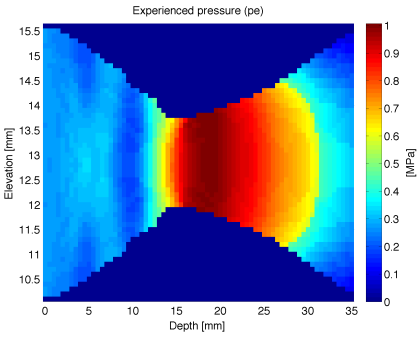

(b) (F-O)

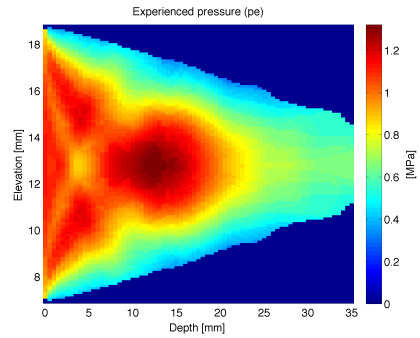

(c) (P-V)

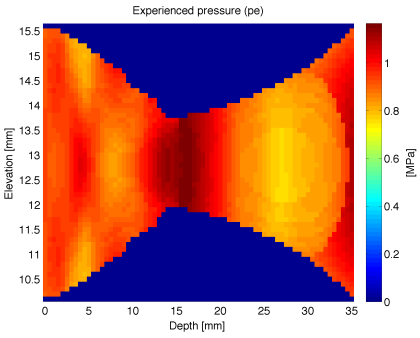

(d) (P-O)

Figure A.12: Profiles of the manipulation pressure experienced by the HF-imaging pulse in the elevation plane for the different configurations.

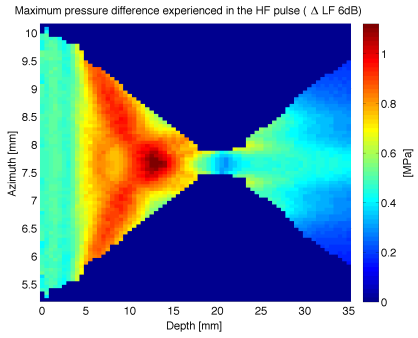

(a) (F-V)

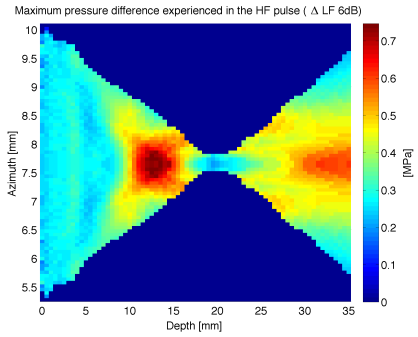

(b) (F-O)

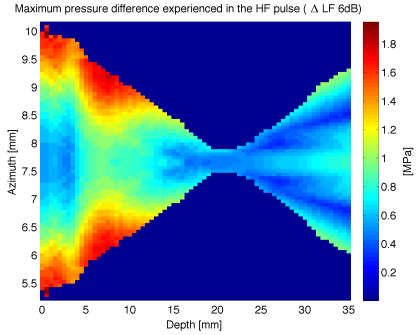

(c) (P-V)

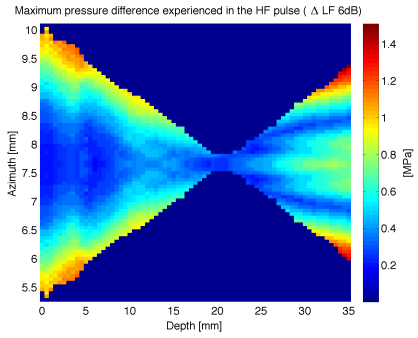

(d) (P-O)

Figure A.13: Profiles of the maximal difference of manipulation pressures experienced by the HF-imaging pulse in the azimuth plane for the different configurations.

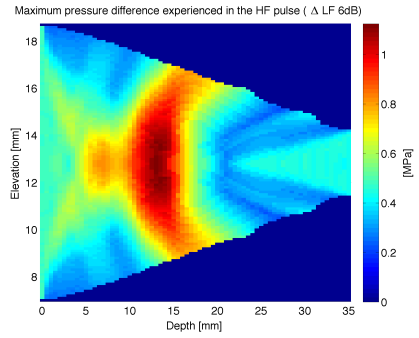

(a) (F-V)

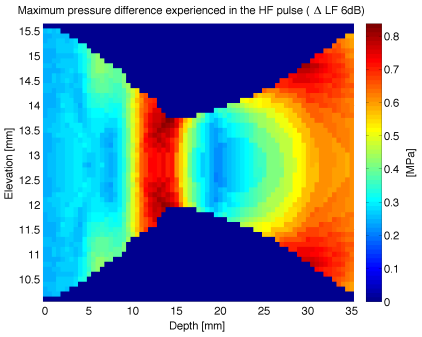

(b) (F-O)

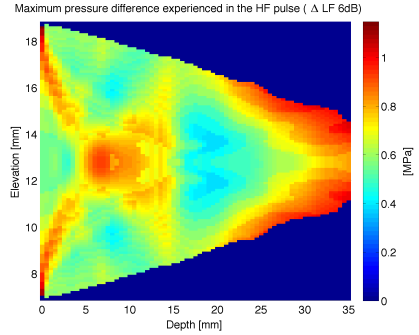

(c) (P-V)

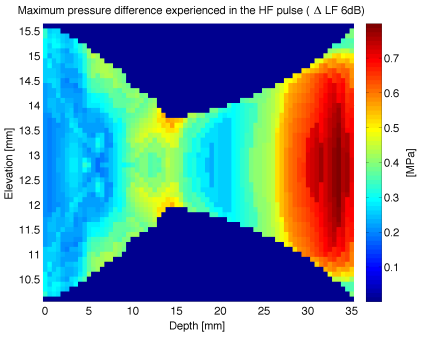

(d) (P-O)

Figure A.14: Profiles of the maximal difference of manipulation pressures experienced by the HF-imaging pulse in the elevation plane for the different configurations.

Appendix B

Water tank investigation of the Okla probe for co-focused SURF pulses

The purpose of this appendix was to verify and document the timing between the high-frequency (HF) and low-frequency (LF) pulses using Okla probe for a situation were both HF and LF are co-focused, and it may be considered as an complement of [40] and [35]. The measurements were performed on march 8th, 2010. This appendix is mainly here to help future students at ISB, and the presented results may be out of date, since both scanner's hardware and software are continuously updated.

B.1 Measurements setup and processing

B.1.1 Water tank

The watertank setup at ISB was used for the measurements. A MATLAB software, ProbeLab (http://svn.isb.medisin.ntnu.no/svn/ProbeLab/trunk) was used for control of the measurement setup, with the Precision Acoustics 200μm SN 1237 needle hydrophone. Water temperature was measured to 21.7°C, corresponding to a sound speed of 1487,6 m/s. The scope was set to average 64 steps.

There has been recorded both axis scans and point scans. The recorded axis scans span from 5 to 35 mm with increment of 0.5 mm.

B.1.2 General Ultrasonix settings

The most important Ultrasonix settings that will affect the measurement for these application are detailed in Table B.1. Unless otherwise specified, these are the settings used.

B.1.3 Processing

The processing of the observed SURF pulses has been done on MATLAB. First, the HF is filtered using a 600 tap bandpass filter with cutoff frequencies at 3 and 30 MHz, while the LF is filtered with an equal length filter with cutoff frequencies at 0.1 and 2 MHz.

Table B.1: Ultrasonix system settings

Tx Frequency B	10 MHz
HF Pulse	+ - +
Tx Aperture Curve	[27 57 100 48]
Tx Aperture Depth	60 mm
Tx Aperture Max	46
LF Tx Frequency	0.9 MHz
LF Number of half cycles	5
LF Tx Rel Apt Size	110% or 200%
LF Tx Aperture Max	20

The presented axis profiles were calculated by taking the maximum of the envelope at each depth.

B.2 Timing between LF and HF pulses using confocal waves

B.2.1 finding initial probe stack delay

In order to find the correct position of the HF pulse, the *probe stack delay* was determined according the the scanner timing definition in [41]:

- for a focus depth of 15 mm, the probe stack delay was found to be -225 ns
- for a focus depth of 20 mm, the probe stack delay was found to be -157 ns

These values have been observed to be correct for both the 110% and 200% relative aperture settings, as depicted in Table B.2.

Table B.2: Settings for defining the probe stack delays for the SURF TCI application

LF					HF		
Wave	Sign	Voltage [V]	f_c [MHz]	Nc	Focus [mm]	HFpos [ns]	Power [dB]
CF	+	50	0.9	5	15 or 20	0	-16

B.2.2 Phase change between HF and LF as a function of LF voltage

Recordings were performed to check the voltage dependency of the phase relation between the HF and LF. The results are presented on Figure B.1 as well as the scanner error definition of ± two samples at 80 MHz (the precision of the delays the scanner is able to handle).

One may see that even though the timing seems adequate for a LF voltage of ±50V, a compensation system similar to the probe stack delay may have to be implemented for use of the SURF probes at different voltages.

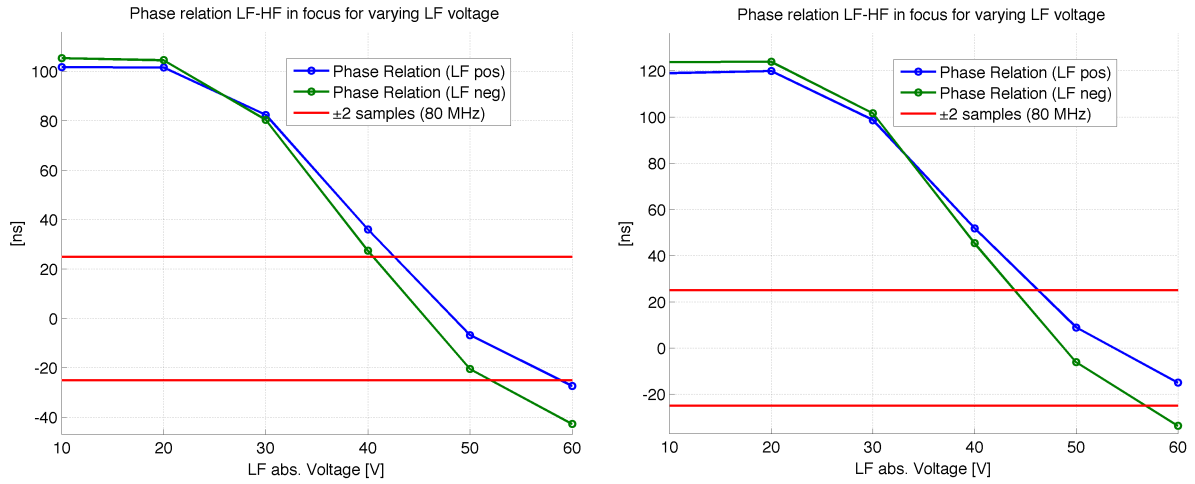

(a) (b)

Figure B.1: Observed phase relation between LF and HF pulses in focus for varying LF voltage. The LF and the HF beams are co-focused at depth 20 mm, and the relative aperture is 110% in (a) and 200% in (b).

B.3 Pressure calibration curves

When dealing with nonlinear scattering, it is useful to know which are the pressure levels involved, since the received signal with be directly related to the pressure experienced by the tissue. Therefore, pressure calibration curves have been established for the LF pressure in focus (20 mm) in water, and are reported in Figure B.2

The HF pressure has been measured in focus (20 mm) in water are reported in Table B.3.

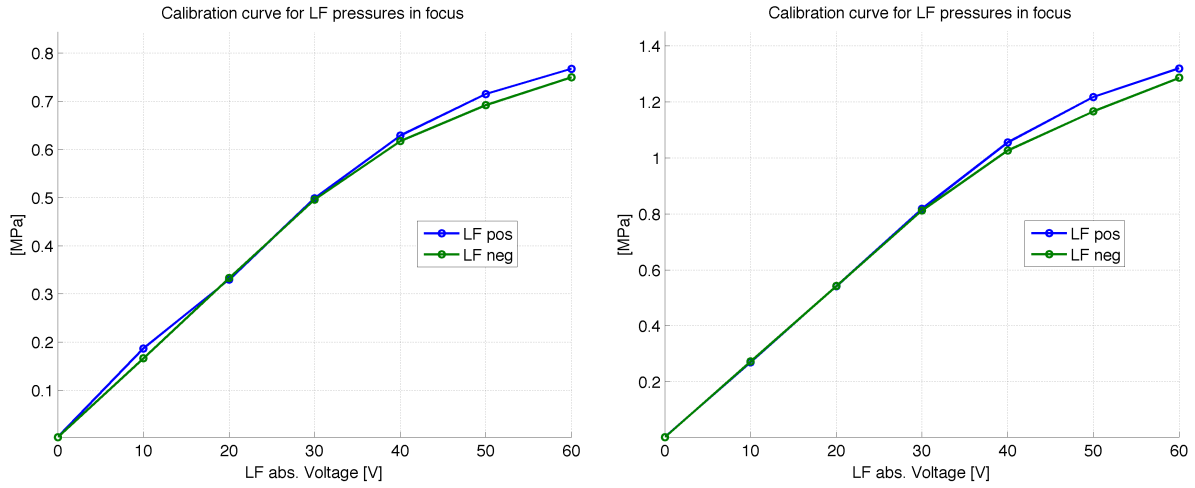

(a) (b)

Figure B.2: LF pressure calibration curves in water, at focal depth (20 mm), when the relative aperture is 110% in (a) and 200% in (b). The pressure is computed as the maximum of the LF-filtered pulse envelope.

The pressures values obtained for real tissues at focal depth in focus may be extracted from the presented results by computing the derated pressures for the desired medium (i.e. taking

Table B.3: HF pressure calibration in water at focal depth (20 mm). The pressure is computed as the maximum of the HF-filtered pulse envelope

Power [dB]	Pressure [MPa]	Derated pressure [MPa]
0	6.62	2.25
-16	1.05	0.36

frequency dependent attenuation into account). For muscle, this may be easily computed using the formula

$$p_{\text{derated}}\left(z_{\text{mm}}\right) = p\left(z_{\text{mm}}\right) \cdot 10^{-\frac{A}{20} \cdot f_{\text{LF,MHz}} \cdot z_{\text{mm}}} \tag{B.1}$$

where A is the attenuation constant (which has for value 0.52 $\text{dB} \cdot \text{MHz}^{-1} \cdot \text{mm}^{-1}$ for muscle at $37°C$ [42, tab. 4.16]), $f_{\text{LF,MHz}}$ is the center frequency of the LF pulse (expressed in MHz), and z_{mm} is the depth (expressed in millimeters).

One may notice that for the use of Okla for imaging of nonlinear scatterers, one must use LF voltages superior to 50V in order to obtain a sufficiently important manipulation pressure at depths such as 20 mm in tissue. Such an important LF voltage is known to create high important distortions of the HF pulse, as well as important heating of the probe surface.

B.4 Comparison of between measured and simulated axial profiles

Numerical simulations have been conducted in order to compare the results from Abersim with the results from the water tank. The simulated propagation was conducted with a strict respect of the scanner configuration (propagation in water at 21.7°C, same apertures, same pressure levels observed in focus...), and the parameters used in the XdSim software are presented in Table B.4.

Table B.4: Parameters used to configure a simulation equivalent to the water tank measurements

	LF	HF
Center frequency f_c [MHz]	0.9	10
Bandwidth B_r [%]	60	80
Number of periods N_p	2.5	1.5
Az. Aperture [# elem.]	12	20
Az. Aperture [mm]	15.8	7.6
Focal length$F$ [mm]	20	20
F-number ($F_{\#} = \frac{F}{D}$)	1.3	2.6
Initial position [ns]	0	-49
Amplitude [kPa]	0.38	0.15

Some profiles along the transducer central axis allow a comparison between the simulations and the water tank measurements. The range evolution of the phase relation between the HF and LF pulses is presented in Figure B.3, the LF manipulation pressure p_m as well as the pressure p_e experienced by the HF pulse are presented in Figure B.4, and the positively manipulated HF pulse profiles are presented in Figure B.5. The pressure profiles were computed in a similar way for the water tank measurements and the simulations, by taking the maximum of the pulse envelope.

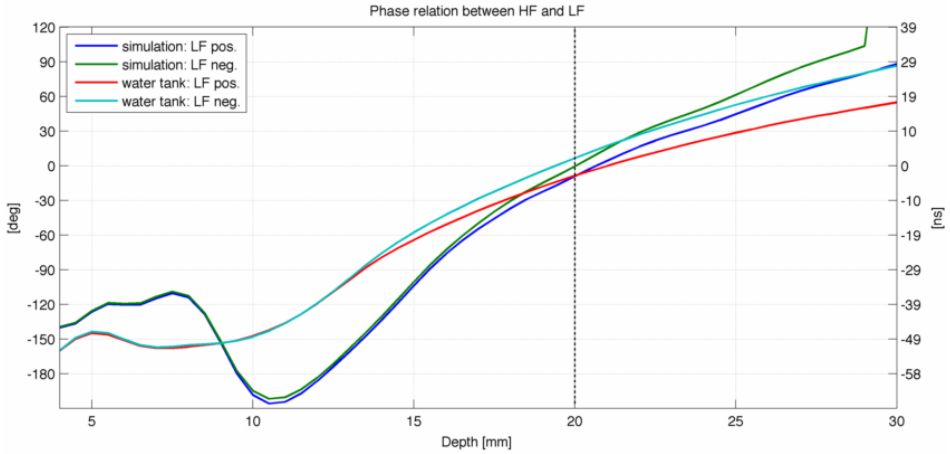

Figure B.3: Comparison between the phase relation between the LF and HF pulses obtained with numerical simulations and water tank measurements.

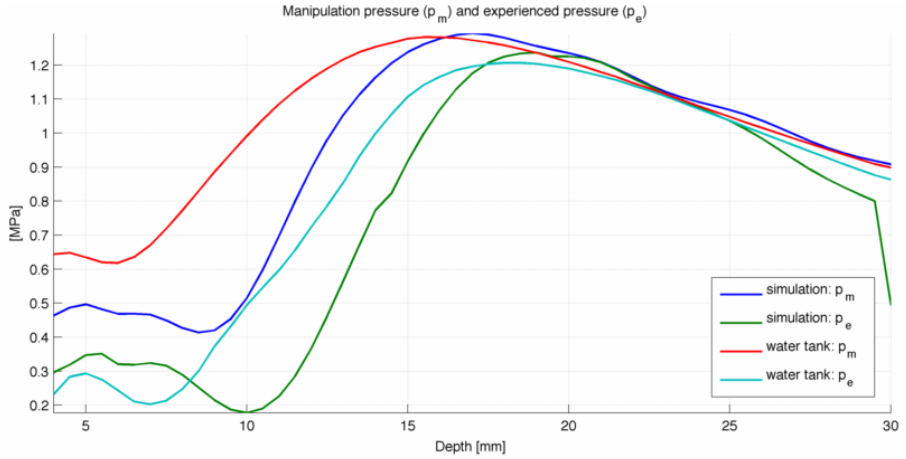

Figure B.4: Comparison between the LF manipulation pressure profiles and the experienced pressure profiles obtained with numerical simulations and water tank measurements.

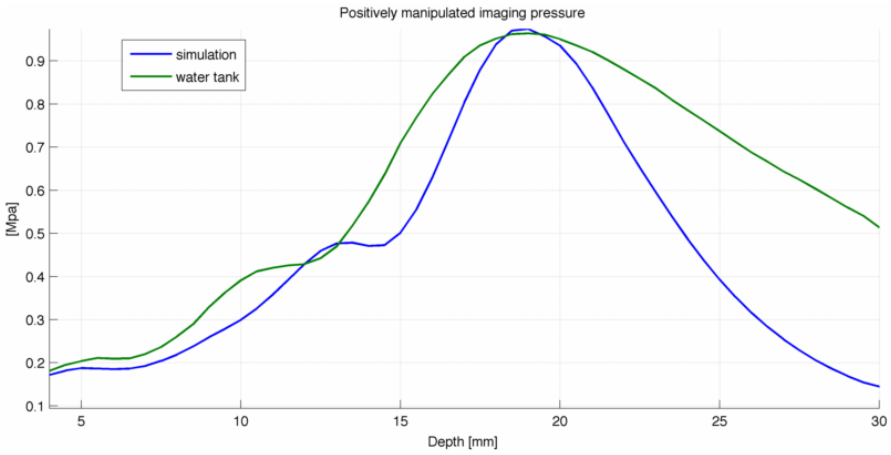

Figure B.5: Comparison between the positively manipulated HF pressure profiles obtained with numerical simulations and water tank measurements.

On the presented profiles, we clearly observe that the difference between the water tank experiments and the simulations reside in the quality of the focusing of the beams. The simulated curves present a better focusing both for the HF and LF beams. This difference can be observed more easily for the LF manipulation pressure profiles.
Such differences between water tank experiments and simulations had not been observed for the previously investigated probes. The difference with Okla reside in its curved shape, and the trick used in Chapter 4.1.3 present clearly some limits: the method using an effective aperture to replace a curved transducer by an equivalent plane transducer do not take into account the *directivity* of the elements on the curved array. The directivity of each individual elements in a curved array is not the same that the other elements on the probe surface (as it is the case for linear probes such as Viglen), and the resulting beam in the direction of the transducer central axis will be reduced in intensity and in focusing quality for a curved probe compared to a linear probe.

Therefore, the results obtained in Chapter 4 for the Okla probe have to be nuanced, since the quality of the beam focusing is poorer in reality, increasing the nonlinear propagations effects by increasing the compression/expansions as well as the level of SURF aberrations. Two main conclusions can be drawn from this discussion:

- The setup (C-O) in Chapter 4 is not as efficient as presented when it comes to limiting the . Therefore, a linear probe specially designed for focal depths around 15 - 20 mm (already being designed at ISB with the name of Vora) could provide even better limitations of the pulse-form distortions for applications in the detection of breast micro-calcifications. Before getting this probe in the laboratory, I have chosen to use the Viglen probe in Chapter 5 because it generated less noise due to a better shielding than the Okla probe.
- One may generate better simulations of the Okla probe by taking the directivity of the elements into account. This may be done by generating the initial pressure field with the framework Field II, and then simulating the pulse propagation with Abersim. A coupling of Field II with Abersim via the XdSim software is a good project for the future.

Appendix C

Matlab code of the pulse-form correction filter

This appendix includes the listing of the Matlab function for the pulse-form correction filter presented and used in Chapter 5. The source file is also available for further work in the continuation of this thesis in the *Arkiv* directory of the *BMT* common server at the ISB department.

Listing C.1: SURF pulse-form correction filter - surf_pulseform_correction.m

```
function [y_c,G] = surf_pulseform_correction(y, conf)
    % [y_c,G] = surf_pulseform_correction(y, conf)
    %
    % Performs pulseform correction using wiener filtering. Uses a moving
    % window at a certain step between two depth limits.
    %
    % Input:
    % y          - Signal to be filtered: y(range, beam, lf_polarity, frame)
    % conf       - configuration parameters
    %
    % Configuration structure 'conf' contains the fields:
    % dim        - dimension for average filter estimation (on beam / frame)
    % Niter      - number of iterations
    % iter_w     - Iteration weighting function handle
    % win_c      - Correction window length for fft
    % win_e      - Estimation window length for fft
    % step       - Step size ≤ win_e
    % overlap    - Percentage of step correction overlap (0 < overlap < 1)
    % fs         - Sampling frequency
    % depth_axis - depth axis where to search for the depth limits
    % depth_lim  - depth limits inside which the filter will be applied
    % Ns         - Noise parameter for the Wiener filter
    % alpha      - Ratios parameter used for tukey windows shapping
    % h          - Filter to be applied at each iteration
    %
    % Output:
    % y_c        - Corrected signal
    % G          - Filters

    [N B P F] = size(y);

    y_c = y;

```

```
34      if ¬isfield(conf, 'dim')
35          conf.dim = 4; % default filter averaging on frames
36      end
37      if ¬isfield(conf, 'Niter')
38          conf.Niter = 1; % one iteration by default
39      end
40      if ¬isfield(conf, 'iter_w')
41          conf.iter_w = @(it) 0.5^it; % iteration basic weighting function
42      end
43      if ¬isfield(conf, 'win_c')
44          conf.win_c = N; % entire signal as correction window
45      end
46      if ¬isfield(conf, 'win_e')
47          conf.win_e = N; % entire signal as estimation window
48      end
49      if ¬isfield(conf, 'step')
50          conf.step = N; % entire signal default step (gives the worst results)
51      end
52      if ¬isfield(conf, 'overlap')
53          conf.overlap = 0.5; % default overlap ratio of half a step
54      end
55      if ¬isfield(conf, 'fs')
56          conf.fs = 40e6; % 40 MHz default sampling frequency
57      end
58      if ¬isfield(conf, 'conf.depth_axis')
59          c0 = 1540;
60          conf.depth_axis = 1e3*c0/conf.fs*(0:(N-1))/2; % depth axis in [mm]
61      end
62      if ¬isfield(conf, 'depth_lim')
63          conf.depth_lim = conf.depth_axis([1 end]); % entire depth axis covered
64      end
65      if ¬isfield(conf, 'Ns')
66          conf.Ns = 0; % no noise power (unit Wiener gain)
67      end
68      if ¬isfield(conf, 'alpha')
69          conf.alpha = [0.5 0.5]; % default ratios for tukey windows
70      end
71      if length(conf.alpha) == 1
72          conf.alpha = conf.alpha([1 1]);
73      end
74
75      [win_c win_c_ix win_c_h] = prepare_window(conf.win_c);
76      [win_e win_e_ix]         = prepare_window(conf.win_e);
77      [step step_ix]           = prepare_window(conf.step);
78
79      fftwin_c  = tukeywin(win_c, conf.alpha(1));
80      fftwin_c  = fftwin_c(:, ones(1,B), [1 1], ones(1,F));
81
82      fftwin_e = tukeywin(win_e, conf.alpha(2));
83      fftwin_e = fftwin_e(:, ones(1,B), [1 1], ones(1,F));
84
85      fe = 1e-6 * linspace(-conf.fs/2, conf.fs/2, win_e);
86      fc = 1e-6 * linspace(-conf.fs/2, conf.fs/2, win_c);
87
88      dlim_ix = find_indx(conf.depth_axis, conf.depth_lim);
89
90      ov_step = ceil(step * (1 - conf.overlap));
91
92      Ndepth  = dlim_ix(end) - dlim_ix(1) + 1;
93      Nstep   = ceil( (Ndepth - win_c + 1) / ov_step );
```

```
94
95      switch conf.dim
96          case 2
97              G = ones(win_c, F, Nstep);
98          case 4
99              G = ones(win_c, B, Nstep);
100     end
101
102     if ¬isfield(conf, 'h')
103         H   = ones(win_c,1); % no extra filtering
104     else
105         if size(conf.h,1) == 1
106             conf.h = conf.h';
107         end
108         H   = abs(fft(conf.h, win_c));
109     end
110
111     if isreal(y)
112         hfunc = @hilbert;
113         rfunc = @real;
114     else
115         hfunc = @noop;
116         rfunc = @noop;
117     end
118
119     the_y = zeros(Nstep,N,B,F);
120     the_w = zeros(Nstep,N,B,F);
121
122     % Estimate the correction filter step by step:
123
124     for k = 1:Nstep
125
126         n = dlim_ix(1) + win_c_h + (k-1)*ov_step;
127
128         y_s = y; % signal copy for this step
129
130         % Extract the windowed data at the current step
131         y_wc = fftwin_c .* y_s(n + win_c_ix,:,:,:);
132
133         for it = 0:(conf.Niter-1) % iterative correction
134
135             % Extract the windowed data at the current step
136             y_we = fftwin_e .* y_s(n + win_e_ix,:,:,:);
137
138             % Estimate the filter
139             lambda = conf.iter_w(it);
140
141             G_old = squeeze(G(:,:,k));
142             [G_new Kc] = estimate_pulseform_correction_filter(y_we, ...
143                                                 conf.dim, conf.Ns, fe, fc);
144             G(:,:,k) = G_old * (1-lambda) + G_old .* G_new * lambda;
145
146             % Apply the filter to the step (no overlap)
147             y_s(n + win_c_ix,:,:,:) = apply_pulseform_correction_filter( ...
148                                       G(:,:,k), y_wc, conf.dim, rfunc, Kc, H);
149
150         end
151
152         y_c(n + step_ix,:,1,:) = y_s(n + step_ix,:,1,:);
153
```

```
154         the_y(k,n + step_ix,:,:) = squeeze(the_y(k,n + step_ix,:,:)) ...
155                                             + squeeze(y_s(n + step_ix,:,2,:));
156         the_w(k,n + step_ix,:,:) = the_w(k,n + step_ix,:,:) + 1;
157 
158         clear y_s;
159     end
160 
161     y_ct = squeeze(wavg(the_y, the_w, 1));
162     c_ix = (dlim_ix(1) + win_c_h+step_ix(1)) : n+step_ix(end);
163     y_c(c_ix,:,2,:) = y_ct(c_ix,:,:);
164 
165 end
166 
167 function [Gc Kc] = estimate_pulseform_correction_filter(y_we, dim, Ns, fe, fc)
168     Y_we = fft(y_we,[],1);
169 
170     % Wiener filter:
171     XY = Y_we(:,:,1,:) .* conj(Y_we(:,:,2,:));
172     YY = Y_we(:,:,2,:) .* conj(Y_we(:,:,2,:));
173     w = real(XY) ./ abs(XY);
174 
175     Ke = squeeze(1 ./ (1 + Ns./YY));
176     Kc = interp1(fe, Ke, fc', 'linear', 0);
177 
178     Ge = squeeze( wavg(XY,w,dim) ./ wavg(YY,w,dim) );
179     Gc = interp1(fe, Ge, fc', 'linear', 0);
180 end
181 
182 function y_c = apply_pulseform_correction_filter(Gc, y_wc, dim, rfunc, Kc, H)
183     B = size(y_wc, 2);
184     F = size(y_wc, 4);
185 
186     Y_wc = fft(y_wc,[],1);
187     switch dim
188         case 2
189             G = permute(Gc(:,:,ones(1,B)), [1 3 2]);
190         case 4
191             G = Gc(:,:,ones(1,F));
192     end
193 
194     Y_wc(:,:,2,:) = Kc .* H(:,ones(1,B),ones(1,F)) .* G(:,:,ones(1,F)) ...
195                                                     .* squeeze(Y_wc(:,:,2,:));
196     Y_wc(:,:,1,:) = Kc .* H(:,ones(1,B),ones(1,F)) .* squeeze(Y_wc(:,:,1,:));
197 
198     % Reintroduce the filtered data into the corrected output
199     y_c = rfunc(ifft(Y_wc,[],1));
200 end
201 
202 function [win win_ix win_h] = prepare_window(win)
203     win     = win + (1-mod(win,2));
204     win_h   = (win - 1) / 2;
205     win_ix  = -win_h : win_h;
206 end
207 
208 function x = noop(x)
209 %     x = x;
210 end
```

Appendix D

Matlab code used for SURF post-processing of data from the scanner

This appendix main purpose is to help the future student starting at ISB. It presents two examples of listings used for:

- Acquisition of data with the scanner coupled to a displacement robot.
- Post-processing of the data collected in Chapter 5 through the usual SURF treatment: reception of the RF-data, RF filtering, IQ demodulation, delay estimation and correction, pulse-form correction.

The Matlab scripts use a framework developed at ISB for importing and handling RF-data from the Ultrasonix scanner, and controlling the Physik instrument robot present in the laboratory. The source files are also available for further work in the continuation of this thesis in the *Arkiv* directory of the *BMT* common server at the ISB department.

Listing D.1: Example acquisition of data with the Ultrasonix scanner and the robot control

```
clear all; close all; clc;

ulterius_params;

general.param_ids = [...
    FOCUS_DEPTH_ID,...
    LF_FREQ_ID,...
    LF_FOCUS_ID,...
    LF_REL_APT_SZ_ID,...
    DEPTH_ID...
    SKINLINE_ZERO_RF_ID...
    ];
general.param_values = [20e3,0.9e6,0,200,40,160];

% B-mode 0V
setup{1}.param_ids = [...
    LF_CENTER_ACTIVE_ID,...
    LF_OUTER_ACTIVE_ID,...
    HF_POSITION_ID
```

```
    ];
setup{1}.param_values = [0,0,0];

% Confocal 50V
setup{2}.param_ids = [...
    LF_INDEP_FOCUS_ID,...
    LF_CENTER_ACTIVE_ID,...
    LF_VOLTAGE_ID
    ];
setup{2}.param_values = [0,1,50];


ult = multerius;

if ¬ult.connect('localhost')
    disp('Could not connect'); return;
end

% Connect to robot
rob = physik('COM1');
connect(rob);
% Set up general parameters
for kk=1:length(general.param_ids)
    if ¬ult.set_int_param(general.param_ids(kk),general.param_values(kk))
        fprintf('Could not set parameter with ID : %d and value : %d \n', ...
            general.param_ids(kk),general.param_values(kk));
    end
end

rob = move(rob,[0 0 0]);
while get(rob,'moving')
    'Moving';
end
pos0 = get(rob,'position');
dr = [1e-3 0 0]';
Nimages = 100;

rob = set(rob,'maxpos',pos0 + (Nimages+1)*dr);

wh = waitbar(0,'Scanning');

tot_imgs = length(setup)*Nimages;
for kk=1:length(setup)

    % Set the parameters
    setup_kk = setup{kk};
    for nn=1:length(setup_kk.param_ids)
        if ¬ult.set_int_param(setup_kk.param_ids(nn),setup_kk.param_values(nn))
            fprintf('Could not set parameter with ID %d and value %d \n', ...
                            setup_kk.param_ids(nn),setup_kk.param_values(nn));
        end
    end

    ult.set_freeze_state(1);
    cmd_str = sprintf('!GetParams.exe -f %s\\setup=%d.xml',pwd,kk);
    eval(cmd_str);
    disp('Parameters are set.')

    ult.set_freeze_state(0);
    pause;
```

```
80      ult.set_freeze_state(1);
81
82      for img_num=1:Nimages
83          this_img = (kk-1)*Nimages + img_num;
84          waitbar(this_img/tot_imgs, wh, ...
85                      sprintf('Recording img #%d of setup #%d',img_num,kk));
86
87          % Wait for images to be recorded
88          ult.set_freeze_state(0);
89          pause(4);
90          ult.set_freeze_state(1);
91
92          %[success data] = ult.get_cine_data(multerius.RF,50);
93          % Retrieve data
94          fname = sprintf('data\\rf_setup=%d_pos=%d.rf',kk,img_num);
95          cmd_str = ['!console.exe 51 ' fname];
96          eval(cmd_str);
97
98          % Move robot
99          rob = relmove(rob,dr);
100         while get(rob,'moving')
101             'Moving';
102         end
103         pause(0.5);
104     end
105
106     [success data_desc] = ult.get_data_desc(multerius.RF);
107     rf = zeros(data_desc.h,data_desc.w/2,2,Nimages);
108
109     disp('Averaging data');
110     for img_num=1:Nimages
111         fname = sprintf('data\\rf_setup=%d_pos=%d.rf',kk,img_num);
112         [tmp hdr] = load_ux_signal(fname);
113         rf(:,:,:,img_num) = mean(tmp,4);
114         clear tmp
115         delete(fname);
116     end
117     fname = sprintf('data\\data_setup=%d.mat',kk);
118     save(fname,'rf','hdr');
119     clear rf;
120
121     rob = move(rob,pos0);
122     while get(rob,'moving')
123         'Moving';
124     end
125     disp('Done with setup');
126 end
127 close(wh);
128 disconnect(rob);
129 ult.disconnect();
```

Listing D.2: Example of the post-processing applied on a SURF signal

```
clear all; close all; clc;

setups = 1:2;
c0 = 1540;

%% ———————— Loading data ———————— %%

data = cell(1,length(setups));
beams = 70 + (-20:20); % [];

for kk=1:length(setups)
    fname = fullfile('data',sprintf('data_setup=%d.mat',kk));
    hh = load(fname);
    data{kk}.fs_rf = hh.hdr.sf;
    data{kk}.Ts_rf = 1/data{kk}.fs_rf;

    if isempty(beams)
        data{kk}.rf = hh.rf;
    else
        data{kk}.rf = hh.rf(:,beams,:,:);
    end
    disp(['RF data extracted for setup ' num2str(kk)]);
end

%% ———————— Filtering of data ———————— %%

Ntaps = 60;
fco = [4.5 9]*1e6;

for kk=1:length(data)
    [data{kk}.rf data{kk}.h_rf] = rf_filtering(data{kk}.rf, Ntaps, fco, ...
                                                data{kk}.Ts_rf);
    data{kk}.z_rf = 1e3*c0*data{kk}.Ts_rf*(0:(size(data{kk}.rf,1)-1))/2;

    disp(['RF data filtered for setup ' num2str(kk)]);
end

%% ———————— IQ demodulation ———————— %%
fdemod = 0;
cutoff = 3; % [MHz]
decimation = 1;

for kk=1:length(data)
    iq_temp = zeros(size(data{kk}.rf));

    for nn=1:size(data{kk}.rf,4)
        for ii=1:size(data{kk}.rf,3)
            iq_temp(:,:,ii,nn) = hilbert(data{kk}.rf(:,:,ii,nn));
        end
    end
    data{kk}.iq = iq_temp(1:decimation:end,:,:,:);
    clear iq_temp;

%     % Alternative:
%     [iq_temp, a, b] = demod_ustb(data{kk}.rf, data{kk}.fs_rf, fdemod, ...
%                                                 'narrowband', Ntaps, cutoff);
%     data{kk}.iq = iq_temp(1:decimation:end,:,:,:);

    data{kk}.fs_iq = data{kk}.fs_rf/decimation;
```

```
60      data{kk}.Ts_iq = 1/data{kk}.fs_iq;
61      data{kk}.z_iq = 1e3*c0*data{kk}.Ts_iq*(0:(size(data{kk}.iq,1)-1))/2;
62
63      disp(['IQ data extracted for setup ' num2str(kk)]);
64  end
65
66  %% ------------ Delay and center frequency estimation ------------ %%
67
68  dz_mm = 1e3 * c0 * data{1}.Ts_iq / 2;
69
70  % Delay estimation parameters
71  delay_win_mm = 3;
72  delay_win = ceil(delay_win_mm/dz_mm/2);
73  reg_meth = 'lin_conv';
74
75  % Frequency estimation parameters
76  fc = 6e6;
77  Tp = 1/fc;
78  freq_win_per = 22.5;
79  freq_win = floor(freq_win_per*Tp/data{1}.Ts_iq);
80  freq_step_per = 2.5;
81  freq_step = floor(freq_step_per*Tp/data{1}.Ts_iq);
82
83  for kk=1:length(data)
84      data{kk}.tau    = zeros(size(data{kk}.iq,1), size(data{kk}.iq,2), ...
85                                                   size(data{kk}.iq,4));
86      data{kk}.fc_est = zeros(size(data{kk}.iq,1), size(data{kk}.iq,3), ...
87                                                   size(data{kk}.iq,4));
88
89      for nn=1:size(data{kk}.iq,4)
90          data{kk}.tau(:,:,nn) = delay_wls(data{kk}.iq(:,:,:,nn), ...
91                      delay_win, data{kk}.fs_iq, fdemod, fdemod, reg_meth);
92
93          data{kk}.fc_est(:,1,nn) = freq_estimation(data{kk}.iq(:,:,1,nn), ...
94                      data{kk}.fs_iq, freq_win, freq_step, 'fft');
95          data{kk}.fc_est(:,2,nn) = freq_estimation(data{kk}.iq(:,:,2,nn), ...
96                      data{kk}.fs_iq, freq_win, freq_step, 'fft');
97      end
98
99      % Average tau over all frames and convert to seconds
100     data{kk}.tau = mean(data{kk}.tau,3) / data{kk}.fs_iq;
101
102     % Subtract signals to make simple suppression signal
103     data{kk}.iq_sup = squeeze(data{kk}.iq(:,:,1,:) - data{kk}.iq(:,:,2,:));
104
105     % Compute Relative Amplitude Difference and Relative Tisse
106     % Suppression (no correction)
107     data{kk}.RAD = squeeze(mean(mean(abs(data{kk}.iq(:,:,1,:)),4),2) ...
108                             ./ mean(mean(abs(data{kk}.iq(:,:,2,:)),4),2));
109     data{kk}.RTS = squeeze(mean(mean(abs(data{kk}.iq_sup),3),2) ...
110                             ./ mean(mean(abs(data{kk}.iq(:,:,1,:)),4),2));
111
112     disp(['Delays and center frequencies estimated for setup ' num2str(kk)]);
113 end
114
115 %% ------------ Delay correction ------------ %%
116
117 for kk=1:length(data)
118     if kk > 1
119         data{kk}.iq_dc = zeros(size(data{kk}.iq));
```

```
120
121         % Correct delay
122         for nn=1:size(data{kk}.iq,4)
123             data{kk}.iq_dc(:,:,:,nn) = correct_delay(data{kk}.iq(:,:,:,nn), ...
124                             data{kk}.tau, data{kk}.fs_iq, fdemod, 'linear');
125         end
126
127     else
128         data{kk}.iq_dc = data{kk}.iq;
129     end
130
131     % Subtract signals to make simple suppression signal
132     data{kk}.iq_sup_dc = squeeze(data{kk}.iq_dc(:,:,1,:) ...
133                                                 - data{kk}.iq_dc(:,:,2,:));
134
135     % Compute Relative Amplitude Difference and Relative Tisse
136     % Suppression (delay correction only)
137     data{kk}.RAD_dc = squeeze(mean(mean(abs(data{kk}.iq_dc(:,:,1,:)),4),2) ...
138                                 ./ mean(mean(abs(data{kk}.iq_dc(:,:,2,:)),4),2));
139     data{kk}.RTS_dc = squeeze(mean(mean(abs(data{kk}.iq_sup_dc),3),2) ...
140                                 ./ mean(mean(abs(data{kk}.iq_dc(:,:,1,:)),4),2));
141
142     disp(['Delays corrected for setup ' num2str(kk)]);
143 end
144
145 %% ---------- Pulse form correction ---------- %%
146
147 depth_lim   = [18 23.5]; %[5 30];   % correction depth interval
148 Ns          = 1e4;                   % influence of the noise
149
150 Nc    = 5;                           % number of cycles of the HF pulse
151 Tp_mm = 1e3 * c0 * (Nc/fc) / 2;     % pulse length [mm]
152
153 for kk=1:length(data)
154
155     if kk > 1
156         clear conf;
157         data{kk}.iq_c = zeros(size(data{kk}.iq));
158
159         depth_axis  = data{kk}.z_iq;
160         dz_mm       = data{kk}.z_iq(2)-data{kk}.z_iq(1);
161         step        = round(2 * Tp_mm / dz_mm);
162
163         conf.dim        = 4; % filter averaging on frames
164         conf.Niter      = 10;
165         conf.iter_w     = @(it) max(0.9^it, 0.05);
166         conf.win_c      = round(12 * Tp_mm / dz_mm);
167         conf.win_e      = round(8 * Tp_mm / dz_mm);
168         conf.step       = round(2 * Tp_mm / dz_mm);
169         conf.overlap    = 0.45;
170         conf.fs         = data{kk}.fs_iq; % 40 MHz default sampling frequency
171         conf.depth_axis = data{kk}.z_iq;
172         conf.depth_lim  = [5 35];
173         conf.Ns         = 1e5;
174         conf.alpha      = [0.5 0.5];
175         conf.h          = data{kk}.h_rf;
176         conf.do_plot    = 1;
177
178         % Pulse-form correction
179         data{kk}.iq_c = surf_pulseform_correction(data{kk}.iq_dc, conf);
```

```
180
181     else
182         data{kk}.iq_c = data{kk}.iq_dc;
183     end
184
185     % Subtract signals to make simple suppression signal
186     data{kk}.iq_sup_c = squeeze(data{kk}.iq_c(:,:,1,:) - data{kk}.iq_c(:,:,2,:));
187
188     % Compute Relative Amplitude Difference and Relative Tisse
189     % Suppression (pulse-form correction)
190     data{kk}.RAD_c = squeeze(mean(mean(abs(data{kk}.iq_c(:,:,1,:)),4),2) ...
191                                 ./ mean(mean(abs(data{kk}.iq_c(:,:,2,:)),4),2));
192     data{kk}.RTS_c = squeeze(mean(mean(abs(data{kk}.iq_sup_c),3),2) ...
193                                 ./ mean(mean(abs(data{kk}.iq_c(:,:,1,:)),4),2));
194
195     for nn=1:size(data{kk}.iq, 4)
196         data{kk}.fc_corr(:,nn) = freq_estimation(data{kk}.iq_c(:,:,2,nn), ...
197                                 data{kk}.fs_iq, freq_win, freq_step, 'fft');
198     end
199
200     disp(['Pulse-form corrected for setup ' num2str(kk)]);
201 end
202
203 %% ---------- Save processed data ---------- %%
204
205 save(fullfile(pwd,'processed_data.mat'), '-v7.3', 'data');
206 disp(['Processed data saved in ' fullfile(pwd,'processed_data.mat')]);
```

Bibliography

[1] K. Armstrong, E. Moye, S. Williams, J. A. Berlin, and E. E. Reynolds. Screening mammography in women 40 to 49 years of age: a systematic review for the american college of physicians. *Annals of Internal Medicine*, 146:516–526, 2007.

[2] G. M. Tse, P. H. Tan, A. L. Pang, A. P. Tang, and H. S. Cheung. Calcifications in breast lesions - pathologists perspective. *Journal of Clinical Pathology*, 60:1–26, 2007.

[3] B.A.J. Angelsen. *Ultrasound Imaging - Waves, Signals, and Signal Processing*, volume I. Emantec, Norway, 2000.

[4] B.A.J. Angelsen. *Ultrasound Imaging - Waves, Signals, and Signal Processing*, volume II. Emantec, Norway, 2000.

[5] Francis A Duck. Nonlinear acoustics in diagnostic ultrasound. *Ultrasound in medicine & biology*, 28(1):1–18, 01 2002/01/01.

[6] P. J. A. Frinking, A Bouakaz, J Kirkhorn, F. J. Ten Cate, and N De Jong. Ultrasound contrast imaging: Current and new potential methods. *Ultrasound in medicine & biology*, 26(6), 2000.

[7] R. Hansen, S.E. Måsøy, T. F. Johansen, and B. A. J. Angelsen. Utilizing dual frequency band transmit pulse complexes in medical ultrasound imaging. *The Journal of the Acoustical Society of America*, 127(1):579–587, 2010.

[8] H. Fukukita, S. Ueano, and T. Yano. Ultrasound pulse reflection mode measurement of nonlinearity parameter b/a and attenuation coefficient. *Journal of the Acoustical Society of America*, 1996.

[9] B.A.J. Angelsen and R. Hansen. Surf imaging - a new method for ultrasound contrast agent imaging. In *Ultrasonics Symposium, 2007. IEEE*, pages 531–541, Oct. 2007.

[10] R Hansen and B J Angelsen. SURF imaging for contrast agent detection. *IEEE Transactions on Ultrasonics, Ferroelectrics, and Frequency Control*, 56(2):280–90, February 2009. PMID: 19251515.

[11] T. Johansen, J. Deibele, S.-E. Måsøy, R. Hansen, and B. A. J. Angelsen. Design and test of a dual-layer, dual frequency surf array. In *Proceedings of the 31st Scandinavian Symposium on Physical Acoustics*, 2008.

[12] D.H. Simpson and P.N. Burns. Pulse inversion doppler: a new method for detecting nonlinear echoes from microbubble contrast agents. *IEEE Ultrasonics Symposium*, 2:1597–1600 vol.2, Oct 1997.

[13] S. E. Måsøy. *Estimation and correction of aberration in medical ultrasound imaging.* PhD thesis, NTNU, 2004.

[14] J. Grythe. Improving elastography using surf imaging for suppression of reverberations. Master's thesis, NTNU, 2009.

[15] M. Afadzi. Detection of microcalcifications for breast cancer diagnosis using surf imaging. Master's thesis, NTNU, dec 2007.

[16] J. P. Svanem. Vevskarakterisering ved surf imaging: Diagnose av prostatakreft. Master's thesis, NTNU, jun 2008.

[17] Thor Andreas Tangen. Real time delay estimation and correction for a new dual frequency method in ultrasound imaging. Master's thesis, NTNU, 2006.

[18] B. Dénarié. Characterization of SURF pulse propagation. Master's project, NTNU, dec 2009.

[19] Fact sheet no. 297 World Health Organization. http://www.who.int/mediacentre/factsheets/fs297 /en/index.html.

[20] MedicineNet. http://www.medicinenet.com/breast cancer/.

[21] O. Peart. *Mammography and Breast Imaging:Just the Facts.* McGraw-Hill Medical Publishing Division, New York, 2005.

[22] S. F. McGee, F. Lanigan, E. Gilligan, and B. Groner. *Mammary Gland Biology and Breast Cancer*, volume 7. European Molecular Biology Organization (EMBO) Molecular Medicine, jun 2006.

[23] D. Kopans. *Breast Imaging.* Lippincott, Williams & Wilkins, 2006.

[24] R. S. C. Cobbold. *Foundations of biomedical ultrasound.* Oxford University Press, 2007.

[25] O. Standal, T.A. Tangen, and B.A.J. Angelsen. A phase based approach for estimation and tracking of locally variable delays. In *Ultrasonics Symposium, 2007. IEEE*, pages 1583–1585, 2007.

[26] Ultrasonix Medical Corp. http://ultrasonix.com/updates/sonixrp/.

[27] S.-E. Masoy, O. Standal, P. Nasholm, T.F. Johansen, B. Angelsen, and R. Hansen. SURF imaging: In vivo demonstration of an ultrasound contrast agent detection technique. *Ultrasonics, Ferroelectrics and Frequency Control, IEEE Transactions on*, 55(5):1112–1121, 2008.

[28] ABERSIM. http://www.ntnu.no/abersim.

[29] Mathworks. http://www.mathworks.com/.

[30] T. Varslot and S. E. Måsøy. Forward propagation of acoustic pressure pulses in 3d soft biological tissue. *Modeling, Identification and Control*, 27:181–200(20), July 2006.

[31] Vermon. http://www.vermon.com/.

[32] S. E. Måsøy, T. F. Johansen, and J. Deibele. Design of VORA, linear SURF array. Design report, SURF Technology AS, Richard Birkelands vei 2B, 7491 Trondheim, Norway, May 2010.

[33] Mechanical Index. http://www.us-tip.com/serv1.php?type=db1&dbs=mechanical%20index.

[34] S. E. Måsøy, T.A. Tangen, O. Standal, J. Deibele, S. P. Näsholm, R. Hansen, B. A. J. Angelsen, and T. F. Johansen. SURF imaging: Acoustics from a dual-frequency band annular array. Transmitted for publication in JASA, mar 2009.

[35] S. E. Måsøy and T.A. Tangen. Water tank measurements: Timing between hf and lf pulse in viglen. Technical report, NTNU, oct 2009.

[36] T.A. Tangen, A. Skavhaug, R. Hansen, S. E. Måsøy, and B. A. J. Angelsen. Suppression of linear scattering for a dual-frequency band imaging technique. NTNU, 2009.

[37] CIRS Model 049 elasticity phantom. http://www.cirsinc.com/049_ultra.html.

[38] http://en.wikipedia.org/wiki/sephadex.

[39] B. A. J. Angelsen. Simulation of the nonlinear wave equationn in gpu. Technical report, NTNU, apr 2010.

[40] S. E. Måsøy and T.A. Tangen. Water tank measurements: Timing between hf and lf pulse in okla. Technical report, NTNU, oct 2009.

[41] S. E. Måsøy. Timing of the lf and hf pulse in the ultrasonix scanner. Technical report, NTNU, feb 2009.

[42] F. A. Duck, A. C. Baker, and H.C. Starrit. *Ultrasound in Medicine*. Institute of Physics Publishing, 1998.